Department of Applied Physics

Properties of the Human Tear Film Lipid Layer

Insight Through Molecular Simulations

Jelena Telenius

Aalto University

DOCTORAL DISSERTATIONS

Aalto University publication series
DOCTORAL DISSERTATIONS 210/2013

Properties of the Human Tear Film Lipid Layer

Insight Through Molecular Simulations

Jelena Telenius

A doctoral dissertation completed for the degree of Doctor of Science (Technology) (Doctor of Philosophy) to be defended, with the permission of the Aalto University School of Science, at a public examination held at the lecture hall E of the school on 17 January 2014 at 12.

Aalto University
School of Science
Department of Applied Physics
Biological Physics Group

Supervising professors
Risto Nieminen
Computational Nanoscience
Department of Applied Physics
Aalto University School of Science

Thesis advisors
Ilpo Vattulainen, Prof.
Biological Physics Group
Department of Physics
Tampere University of Technology

Preliminary examiners
Matthias Weiss, Prof.
Lehrstuhl Experimentalphysik I
Universität Bayreuth, Germany

Arto Urtti, Prof.
Centre for Drug Research, Faculty of Pharmacy
University of Helsinki

Opponents
Jesus Perez Gil, Prof.
Dept. Bioquimica y Biologia Molecular I,
Universidad Complutense, Madrid, Spain

Aalto University publication series
DOCTORAL DISSERTATIONS 210/2013

ISBN 978-952-60-5489-6
ISBN 978-952-60-5490-2 (pdf)
ISSN-L 1799-4934
ISSN 1799-4934 (printed)
ISSN 1799-4942 (pdf)
http://urn.fi/URN:ISBN:978-952-60-5490-2

Unigrafia Oy
Helsinki 2013

Finland

441 697
Printed matter

Aalto University

Abstract

Aalto University, P.O. Box 11000, FI-00076 Aalto www.aalto.fi

Author
Author

Name of the doctoral dissertation
Properties of the Human Tear Film Lipid Layer - Insight Through Molecular Simulations

Publisher School of Science

Unit Department of Applied Physics

Series Aalto University publication series DOCTORAL DISSERTATIONS 210/2013

Field of research Computational biophysics

Manuscript submitted 21 August 2013 **Date of the defence** 17 January 2014

Permission to publish granted (date) 10 October 2013 **Language** English

☒ **Monograph** ☐ **Article dissertation (summary + original articles)**

Abstract

The outer layer of human tear film – the tear film lipid layer – covers the surface of the eye. This layer is the interface between the tear film and the air surrounding the eye. Abnormal composition of the tear film and its lipid layer may have quite severe consequences for health in terms of the so-called "dry eyes syndrome". People with dry eyes experience uncomfortable feelings, which bear a resemblance to having "sand in the eyes", and they have also excessive tear production and blurry vision. In addition to the abnormal lipid composition, also abnormal secretion of the tears themselves can lead to the development of dry eyes. Untreated dry eyes can lead to inflammation of the eye surface, and even scarring of the eye surface tissue. Dry eyes are treated with eye drops, which are selected to match the symptoms of the patient – some people need more lipids to the layer, while some others lack the aqueous tears.

In this thesis, the tear film lipid layer was investigated by the means of molecular dynamics simulations. First, it was investigated how lipids in a native composition organize themselves to the interface between air and water. The systems considered were exposed to varying interfacial areas to see what happens to the interfacial region during the early phases of closing and opening the eyes. Second, consequences of abnormal lipid compositions typical to blepharitis patients were explored. Further, these considerations were complemented with simulations of lipid layers with quite diverse compositions to elucidate the roles of certain specific lipids in the function of tear film lipid layers.

It was found that the lipids form a layer to the very interface of air and water. In the normal tear film composition, phospholipids formed the main body of the interfacial layer, while cholesteryl esters were observed to penetrate into it, promoting tighter packing of the interfacial layer. When the system was exposed to decreasing interfacial area to investigate what happens when eyes are being blinked, triglycerides helped the layer to stay intact even at very small interfacial areas. Meanwhile, with lipid layers characteristic to blepharitis patients, the ability to form a continuous lipid layer to the surface was impaired.

Should the tear film lipid layer really be a monolayer-like also in reality, the results suggest that each lipid type in the layer has a specific role to maintain the function of the layer: phospholipids form the interface, cholesteryl esters make it stiffer, and triglycerides enable easier adjustment to changes in interfacial area.

The results presented in the thesis pave the way for new avenues in clinical research of dry eyes, and aid the developing of more suitable eye drops for the treatment of dry eye patients.

Keywords monolayer, coarse grained, MARTINI, molecular dynamics simulation, MD, tear film lipid layer, TFLL, dry eye syndrome

ISBN (printed) 978-952-60-5489-6 **ISBN (pdf)** 978-952-60-5490-2

ISSN-L 1799-4934 **ISSN (printed)** 1799-4934 **ISSN (pdf)** 1799-4942

Location of publisher Helsinki **Location of printing** Helsinki **Year** 2013

Pages 177 **urn** http://urn.fi/URN:ISBN:978-952-60-5490-2

Tekijä
Author

Väitöskirjan nimi
Ihmisen kyynelnesteen rasvakalvon ominaisuuksista - Näkökulmia molekyylidynamiikka-simulaatioista

Julkaisija Teknillinen korkeakoulu

Yksikkö Teknillisen fysiikan laitos

Sarja Aalto University publication series DOCTORAL DISSERTATIONS 210/2013

Tutkimusala Laskennallinen biofysiikka

Käsikirjoituksen pvm 21.08.2013 **Väitöspäivä** 17.01.2014

Julkaisuluvan myöntämispäivä 10.10.2013 **Kieli** Englanti

☒ **Monografia** ☐ **Yhdistelmäväitöskirja (yhteenveto-osa + erillisartikkelit)**

Tiivistelmä

Ihmisen silmän pinnalla on ohut kerros kyynelnestettä, kosteuttamassa ja suojaamassa silmän pintaa. Kyynelnestekalvon uloin kerros koostuu rasvamolekyyleistä. Tämä pintakerros on ns. kyynelnesteen rasvakalvo. Häiriöt kyynelnesteen ja sen rasvakalvon koostumuksessa voivat johtaa ns. "kuivasilmäisyyteen". Kuivasilmäisyyden oireita voivat olla tunne, että on "hiekkaa silmissä", sumentunut näkö, tai vuotavat silmät. Hoitamattomana kuivasilmäisyys johtaa silmän pinnan tulehdukseen ja pahimmillaan edelleen silmän pinnan arpeutumiseen. Kuivasilmäisyyttä hoidetaan silmätipoilla, joiden koostumus valitaan potilaan oireiden mukaan – joidenkin ihmisten kyynelnesteestä puuttuu vettä, toiset tarvitsevat lisää rasvamolekyylejä.

Tässä väitöstutkimuksessa silmän pinnan rasvakalvoa tutkittiin molekyylidynamiikka-simulaatioilla. Ensin tutkittiin rasvakalvoja, jotka vastasivat koostumukseltaan silmän pinnan rasvakalvon normaalia tai lähes normaalia koostumusta. Sitten simulaatioilla tutkittiin silmäluomen tulehduksesta (blepariitti) kärsivien potilaiden rasvakalvon rakennetta.

Simulaatiotuloksia tarkasteltaessa nähtiin rasvojen asettuvan ilman ja veden rajapinnalle monokerrokseksi (yhden rasvamolekyylikerroksen paksuiseksi kerrokseksi). Fosfolipidit muodostivat kalvon perusrakenteen, ja kolesteroliesterit asettuivat niiden väliin, järjestäen rasvamolekyylit tiukemmin pakatuksi kalvorakenteeksi. Kun systeemiä simuloitiin eri rajapinnan pinta-aloilla, huomattiin, että triglyseridit auttoivat kalvoa säilyttämään muotonsa silloinkin, kun ilman ja veden välisen rajapinnan pinta-ala oli hyvin pieni. Tämä saattaa olla triglyseridien rooli silmän pintakalvossa – auttaa kalvoa mukautumaan silmän räpäyttämisessä tapahtuviin pinta-alan muutoksiin. Blepariittipotilaiden rasvakalvo ei simulaatioissa muodostanut vastaavan kaltaista säännöllistä monokerrosrakennetta.

Jos silmän pinnan rasvakalvo todellisuudessakin on yhden lipidikerroksen vahvuinen, tuloksia voitaisiin suoraan soveltaa lääketieteellisessä tutkimuksessa. Toivonkin, että väitöskirjassa esitetyt tulokset voivat auttaa kuivasilmäisyyden tutkimuksessa, ja hoitomuotojen kuten silmätippojen ominaisuuksien kehittämisessä.

Avainsanat monokerros, karkeistaminen, MARTINI, molekyylidynamiikkasimulaatio, MD, kyynelnesteen rasvakalvo, TFLL, kuivasilmäisyys

ISBN (painettu) 978-952-60-5489-6 **ISBN (pdf)** 978-952-60-5490-2

ISSN-L 1799-4934 **ISSN (painettu)** 1799-4934 **ISSN (pdf)** 1799-4942

Julkaisupaikka Helsinki **Painopaikka** Helsinki **Vuosi** 2013

Sivumäärä 177 **urn** http://urn.fi/URN:ISBN:978-952-60-5490-2

Acknowledgements

I want to thank each and every one of you who came to my defense today. All of you have been important to me and my work !

I wish to thank all who contributed to my delightful project with the tear film lipid layers. I felt the subject deeply inspiring – and I enjoyed working with each and every one of you. Thanks to all in the experimental collaboration team (Dr. Juha Holopainen, M.Sc. Pipsa Kulovesi, and M.Sc. Antti Rantamaki). And special thanks to D.Tech. Artturi Koivuniemi, who was first offered the tear film project. However, as he had too many projects already, he generously provided me with this project, which then soon became the basis of my thesis work. I also wish to thank Artturi for all the support and advice in the simulations, and help with technical and scientific problems that I faced during my thesis work. I hardly would have defended without the ever-helpful and ever-willing attitude of his – no problem or question was too trivial for him to answer, and whatever I got stuck with, I got opportunity to discuss with him. And, if he did not have any answers, he always was willing to brainstorm things further, and provide names of more experienced fellow scientists, who I could consult further in my project. Thanks to M.Sc. Matti Javanainen, as well, who has now taken over the project, and will pursue further simulations in the subject with the same experimental team.

I want to thank all BIO group members, for without you I wouldn't have but scratched the surface of MD simulations. Especially I wish to thank everybody who participated in generating the atmosphere in the group meetings of the BIO group at the Aalto University. I have never before and never after experienced such a combination of harsh – but deserved – criticism and generous sharing of the experiences and knowledge, combined with free and open discussion and brainstorming of all scientific problems that anyone in the group was facing. Not only did I learn a lot about my own project, and got new viewpoints to apply to my own work, but I also learned a lot of how MD systems behaved in general, and how one can ensure one is proceeding in the right direction in the simulations.

Special thanks from that inspiring atmosphere go to Markus Miettinen, Emppu Salonen, Luca Monticelli, Teemu Murtola, Olli Punkkinen, Liam McWhirter, Sarah Overduin, Giulia Rossi, Tomasz Rog and Samuli Ollila.

I also wish to thank Hector Martinez Seara, Tomasz, Jukka Maatta, Jaakko Uusitalo, Jarkko Luoma, Emppu, Samuli, and Luca for discussions and practical help in my thesis project.

Special thanks of course goes to my supervisor Prof. Ilpo Vattulainen, for providing solid funding and freedom of research for the whole time of my thesis work, and also for very good comments and feedback during the proofreading of my thesis. It has been truly a journey of a lifetime – and well worth it, thanks for accepting me as part of your group, and thanks for leading me all the way to the defense !

I also wish to thank all other Aalto friends (you know who you are) who let me complain about the “impossible life” and “impossible thesis” of mine – you helped me to push through, and finally I stand here – I will defend, after all !

I owe a deep gratitude towards all my collaborators, and especially my supervisor Assoc. Prof. Himanshu Khandelia in Denmark, in MEMPHYS group of membrane biophysics. The work I conducted while in Denmark did not end up into the thesis – but the enthusiasm and self esteem you equipped me with during my stay in Odense is clearly visible in the written pages of my thesis. Special thanks to all Whiskey club members, for providing me academic discussions also outside the university itself!

Last I wish to thank my new team in Oxford, the Bioinformatics research group of PhD Jim Hughes, for tolerating my varying input in my new and always so intriguing project in mouse genomics, as my efficiency at work has strongly (inversely) correlated with the amount of thesis work I had to do during the nights and weekends.

Thanks to Chris, and mum and all friends – without you my journey through the thesis would have been absolutely unbearable ! Thanks for just being there !

In Oxford, 25 November 2013

Jelena Telenius

Contents

Preface

One of our most important and valuable senses is vision. There are a number of diseases that affect our eyes – including some that affect our vision. Yet, even if our ability to see is not compromised, there are disorders that may hinder our daily lives considerably due to pain involved with our eyes. One of the very common disorders in this context is the dry eyes syndrome. This syndrome has been investigated for decades and there are treatments for its symptoms, yet its cause of is not well understood.

Here we discuss how molecular simulations bridged to experiments in ophthalmology can possibly, and hopefully, shed light on related issues. We discuss what I have done during the recent years together with my supervisors and collaborators to better understand on a molecular level how the tear film lipid layers function on the surface of an eye. It is quite an intriguing idea that lipids, which are the molecular form of fat, may have a role to play in complex diseases such as the dry eye syndrome. A variety of experimental studies yet supports this view in general.

The work I discuss here mainly focuses on molecular simulations that I have carried out to elucidate the structural and also dynamical properties of tear film lipid layers. All simulations have been coupled to experiments, with an aim to gain added value by doing them in unison. However, as the core of my work is based on simulations, this thesis is also organized to highlight the background and practical aspects associated with molecular computer simulations, and then to discuss how they can be used to generate new knowledge about tear film lipid layers.

Some of you may find the presentation too easy, some of you may find it too challenging. It is always quite difficult to find a balance between these two since you may be an expert as well as a newcomer to the field. I have done my best to create a piece of science, which would help everybody, at least a bit. Nonetheless, since my own background is in experimental biochemistry, and this work deals with computational physics applied to a biophysical problem, I have chosen to focus quite a bit on topics which I have found to be both difficult and rewarding during my PhD training period. Many of them deal with the theoretical background of computer

simulations, and physics in general, so please keep this in mind when you read this work.

Chapter 1 deals with the eye and especially the dry eye syndrome. The background and many physics based concepts of molecular computer simulations are introduced and discussed in Chapter 2, after which in Chapter 3 we discuss how they can be used in practice. Chapter 4 summarizes the scientific achievements of this PhD thesis project, and also brings out my personal contribution to the work done. In Chapter 5 we consider the simulation models we have used in the projects, and Chapters 6 and 7 present the new results we have found. The whole work is briefly summarized in Chapter 8. Please enjoy the ride.

Abbreviations

AFM	atomic force microscopy
BAM	Brewster angle microscopy
CE	cholesteryl ester
cm	center of mass
CG	coarse-grained
CO	cholesteryl oleate
CPU	central processing unit
DPD	dissipative particle dynamics
DPPC	di-palmitoyl phosphatidyl choline
DPPE	di-palmitoyl ethanol amine
DNA	deoxyribonucleic acid
FFA	free fatty acid
GIXD	grace incident X-ray spectroscopy
GPU	graphical processing unit
IL	interleukine
LJ	Lennard-Jones potential
MD	molecular dynamics
MSD	mean squared displacement
NMR	nuclear magnetic resonance
NVE	microcanonical ensemble (constant particle number N, vessel volume V, total energy E)
NpT	isothermic-isobaric ensemble (constant particle number N, pressure p, temperature T)
NVT	canonical ensemble (constant particle number N, vessel volume V, temperature T)
OCA	oleyl carboxylic acid
PC	phosphatidyl choline
PCA	palmitoyl carboxylic acid
PL	phospholipid
PME	particle mesh Ewald
POPC	palmitoyl-oleyl phosphatidyl choline
QM	quantum mechanics
RDF	radial distribution function

TFLL	tear film lipid layer
TG	triglyceride
TGFβ1	transforming growth factor β1
TNFα	tumor necrosis factor α
TO	trioleate

MATHEMATICAL SYMBOLS

About the syntax in general

Italics = scalar variables, constants, mathematical symbols

Bold = vectors (variables with both quantity and direction)

d*t* infitesimal change in time (other infitesimal changes similarly denoted by d)

Δt measurable change in time - "time step" (other bigger-than-infitesimal changes similarly)

U_o internal energy in starting state (other starting states similarly denoted by subscript o, and the end state with the bare symbol. ➔ $U - U_o$ denotes "internal energy in the end, minus internal energy in the beginning". However, in angles and torsion angles subscript 'o' means "equilibrium" (as stated in the symbol list below)

<> average over both ensemble (coordinate space) and time points, if not mentioned otherwise. If mentioned, may mean only an ensemble average (coordinate space)

$\overline{A(t)}$ time average of $A(t)$

i-j interaction between particles i and j

Special symbols

n	summing index, "total number of something".
i,j,k,l	indices (of atoms, energy states etc)
α,β	parameters (for scaling the interactions)
x,y,z	cartesian coordinate axes
θ,φ,r	spherical coordinate axes

Vectors

a	acceleration
A	area
B	magnetic field
E	electric field
F	force
p	momentum
r	spatial coordinate
v	velocity

Scalars and functions

a	angle, in angle vibration
b	bond length
d	dihedral angle, rotation angle (d being time dependent, d_o in equlibrium)
D	diffusion coefficient
e	Euler's number
E	energy, electric field (Appendix A)
E_i	energy of certain energy state
g	degeneracy of a state
$g(r)$	radial distribution function (RDF)
h	position of particle (h current, h_o in equilibrium)
$h(x,y)$	height-height correlation function
k	spring constant
k_B	Boltzmann's constant
K	kinetic energy
m	mass
N	number of molecules
q	(partial) charge, wavenumber (elasticity), heat (Appendix C)
Q	electric charge (Appendix A), partition function (Appendix B)
r	bond vibration, radial distance, radius from particle center (in RDF)
S	order parameter, entropy (Appendix C)
t	time
T	absolute temperature (in Kelvins)
U	potential energy, thermodynamic internal energy (Appendixes B-D)
v	velocity
w_i	weight of a molecular state
W	work, weight of configuration (Appendix B)
x	displacement (1-dimensional)
x,y	plane of (planar) lipid layer
z	direction of (planar) lipid layer normal

ε	electric permittivity
ε_0	permittivity of vacuum
ρ	density
π	surface pressure (in pressure-area isotherms)
θ_z	angle between lipid layer normal and lipid hydrocarbon tail
Ω	number of different microstates

1. Eyes, Tear Film, and the Clinical Relevance of the Study

In the first Chapter of this Thesis, we discuss the clinical relevance and the motivation of the present study. The system we focus on is a model of a human tear film lipid layer, which resides at the surface of an eye. The eye in turn is a light-sensing organ, so it has to be situated at the very surface of the human body. This, however, poses significant challenges to the protection and nutrition of this sensory organ. Thereby, we first review the anatomy and function of the eye. We further discuss how the aqueous tear film at the eye surface protects and nurtures the eye, and what role the lipid layer of the tear film may play in this. Also the common failures of this protecting system due to environmental, hormonal, and physiological reasons are reviewed to provide the reader with an overview of the prevalence, etiology, and treatment of the common medical condition known as the "dry eyes syndrome" (*keratoconjunctivis sicca*).

1.1 Structure of the Eye

The human eye is an elastic ball, residing in a bony orbital cavity formed by seven skull bones surrounding the eye (Figure 1) [1-3]. As the eyeball should be able to move rather freely, it does not touch the walls of the cavity, but the space between the eyeball and the bones is lined with foamy fat tissue. Human eye contains six orbital muscles that enable its free movements.

1.1.1 Structure of the Eyeball

The eyeball has a strong and elastic collagenous shield, the sclera, to keep it in shape (Figure 2). The intraocular lens divides the eye to the anterior and posterior segments. The anterior segment is filled with a transparent, non-

viscous anterior chamber fluid, and the posterior pole of the eyeball is filled with a gel-like, viscous transparent fluid, the vitreous [1-3].

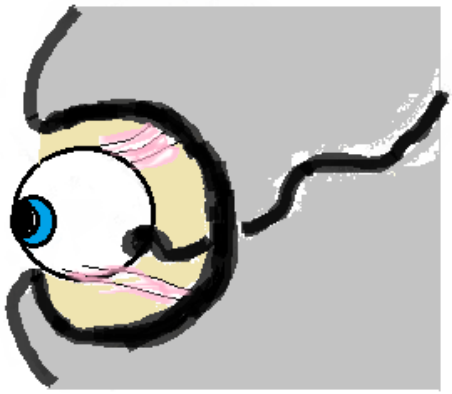

Figure 1. The eyeball resides in a bony orbital cavity (black) surrounded by ocular fat tissue (yellow) protecting the eye. Eye movements are enabled by the action of six orbital muscles (pink), to allow the free movement of the eyeball in the cavity. The visual nerve (black) transfers the visual signal perceived by the eye to the brain [1-3].

The eyeball is surrounded by stiff but thin, form-giving tissue film, the sclera. Immediately under the sclera, there is another thin layer: the choroid, which is the layer of blood vessels providing nutrients to the retina, lying underneath the choroid. The retina is a light sensitive layered structure, which transforms light into chemical energy. This is then transferred via the optic nerve into the visual cortex of the brain [1-3].

The outer layer of the eye (the sclera, which is non-transparent) is in the anterior part of the eye replaced by a transparent layer, the cornea (Figure 2). After passing through the first layer of the eye (the cornea), the light travels through the anterior chamber, which is filled with aqueous liquid resembling the serum of blood [1-3]. The purpose of the transparent liquid is not to enhance the image quality as a part of the refracting system, but instead it transports nutrients to these parts of the eye, as blood cannot enter this perimeter due to its obvious non-transparent nature. After passing through the anterior chamber, the light will enter the lens of the eye via the pupil (which we see as the ”black dot of the eye” as no light comes back from the pupil), and finally travels through the vitreous to reach the retina. If there is too much or too little light entering the retina, the iris muscles contract correspondingly and adjust the pupil size. In the dark the pupil is much larger than in bright light. This enables an optimal amount of light to enter the retina at all times, and diminishes the magnitude of the higher order optical aberrations that may decrease the quality of vision in luminous conditions.

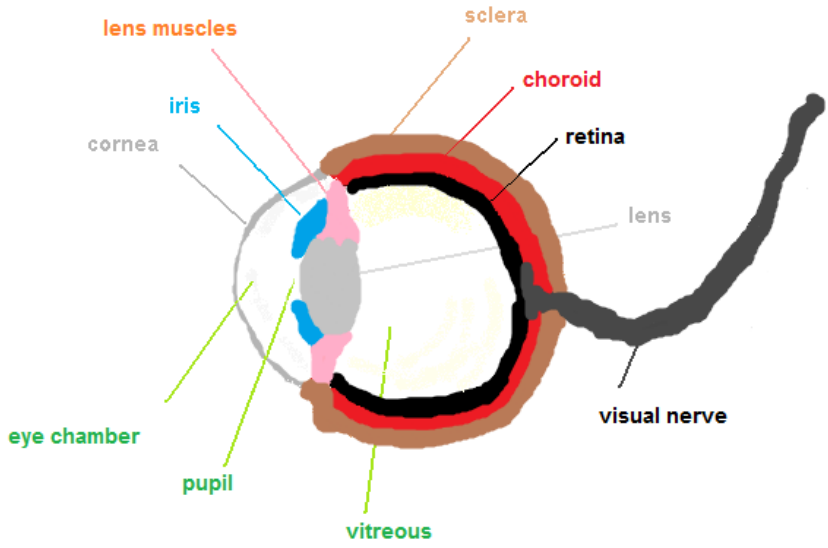

Figure 2. Anatomical parts of the eyeball.

1.1.2 Role of Eye Components in Sensing Light

Targeting the light to the retina is taken care of by both all the transparent eye components, as well as by the air-surface interface of the eye. The first lens of the eye is the pre-ocular tear film, which is mandatory in order to have a smooth optical surface. The air - tear film - cornea interface bends the light the most (approximately two thirds of the optical power of the eye), and the rest of the optical power is due to the intraocular lens (approximately one third, or 20 D) [1-3]. The lens power can be changed by the intraocular muscles, which also enable the focusing on different distances. The closer we look, the more detailed picture our eyes can form, as each nerve cell is like one pixel of our own biological “digital camera”. The picture will be formed upside down to the retina, and only in the brain is the image turned 180 degrees to form the picture we actually “see” and interpret. The brain also makes image manipulation, like shape recognition, and thereby adds extra contrast to the boundaries of objects to make it easier for us to understand what we actually see [4-5].

1.2 Surface Layer of the Eye

The very anterior surface of the eye consists of the cornea, and a wetting layer on top of that, the so-called tear film. The cornea and tear film serve an important role in the function of the eye. Not only is the very air-cornea interface the most refracting surface of the eye [3,6], but also the surface layer needs to be able to effectively protect the eye from pathogens and foreign objects such as dirt [7-9].

One could ask why such a delicate instrument like the eye is actually located on the very surface of the body – the sensory parts of the ear are for example hidden deep within the scull structure. The reason is obvious – there is way more light on the very surface of the body, and as eyes are for sensing the light, one has to have this sensory organ very close to the hazardous pathogens and dirt of the outside world.

Nonetheless, the eye is equipped with a variety of protecting measures [10]. The inner membrane of the eyelids forms a solid tissue to contact the junction of the sclera and cornea, and in this manner provides a mechanical boundary for external objects not to be transferred inside the eye itself [3]. The tear film also provides an effective protective mechanism – the aqueous fluid of the lacrimal glands. The aqueous fluid – or the "tears" as we usually call them – form a watery layer on the surface of an eye. The tears are rich in antibacterial substances (like lysozyme) and immunoprotective agents such as immunoglobulins [11]. Tears are secreted in the upper, outer corner of the eye (Figure 3), and they flow across the eye surface, rinsing it clean

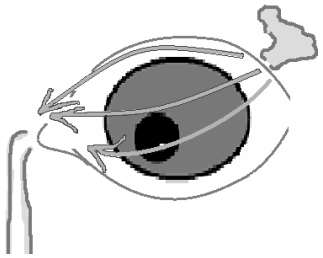

Figure 3. The flow of aqueous tears across the eye surface. The aqueous tears are secreted from the lacrimal gland (up right), and they flow towards the nasolacrimal duct (down left).

from pathogens and dirt [1-3]. The drain for the tears is on the other side of the eye, on the very inner corner, where the nasolacrimal duct will transfer the tears to the nasal cavity. The emotional tears, which we cry when feeling sad, are so plenty that the nasolacrimal duct cannot remove all of them but they run to our cheeks instead. These tears are a much more dilute solution than the normal tears – a lot of water is added to the solution when we cry,

so we will not waste all that precious disinfecting solution when feeling desperate.

1.2.1 Maintaining the Balance of the Tear Film

We have now seen how important the aqueous layer on the surface of the eye really is. It protects the cornea from drying, and from pathogens and dirt [7-11]. The aqeous layer also provides a smooth refractive surface for the light and enables formation of a high quality picture to the retina [6].

There are several mechanisms, which maintain the constant wetting and protection of the cornea. The most important of these is the blinking reflex [12]. Blinking clears the eye surface from dirt and pathogens, and redistributes the moist tear film onto the corneal epithelium every five seconds. It takes half a second for the tear film to spread over the whole surface after the blink [13]. The spread aqueous film will break up abruptly after 7-10 seconds, so a constant series of blinks is needed to maintain moisture at the eye surface [14].

The tear film is thus spread to the eye surface and re-compressed close to eyelid margins every 5 seconds via blinking. The corneal epithelium and the tear film itself are highly specialized to enhance this cyclical moisture generation process at the eye surface.

The very surface of the cornea is coated with sugar-rich molecules, the mucins, which very efficiently bind to water molecules, thus spreading the water layer onto the whole eye surface (Figure 4). These mucins provide a wettable surface along which the tear film can spread onto the eye surface after the blink. Also the aqueous tear layer to be spread onto the eye contains a lot of soluble mucins. These along with the membrane bound mucins form a meshwork-like system aiding wetting and protecting the cornea and conjunctiva [9, 15]. The aqueous phase of the tear film contains also a lot of amphiphilic proteins (for example lipocalins), which enhance the spreading of the lipid layer onto the eye surface after a blink [11,16]. They act as surfactants, lowering the surface tension of the spreading layer [17]. This basically means that these proteins make it more favorable for the water molecules in the aqueous layer to be spread to the interfacial layer, instead of staying close to other water molecules at the lid margins. This lowering in the surface tension enables the layer to be spread fast enough even though a large area of the water-air interface is formed while the layer is spreading.

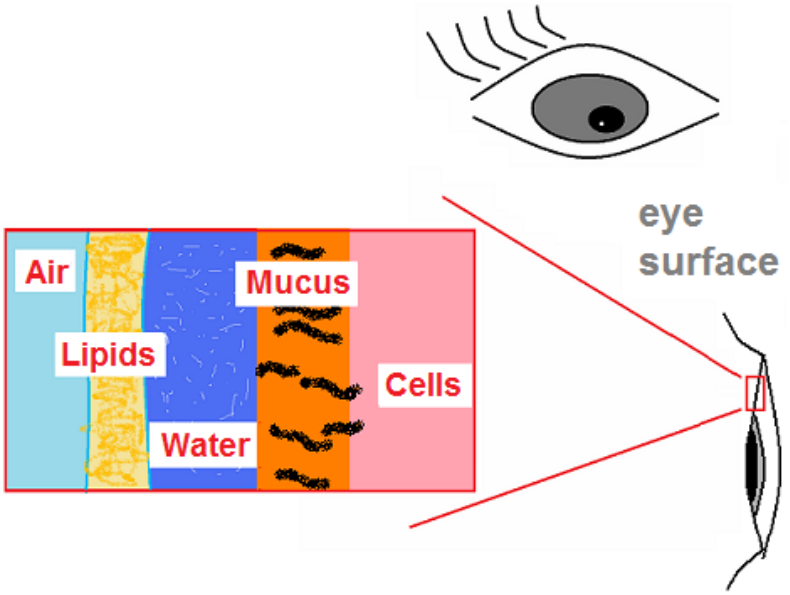

Figure 4. The three layers of the tear film – the mucus layer, the water layer, and the lipid layer (not in scale). The lipid layer is very thin (tens of nanometres) compared to the thickness of the aqueous layer (a couple of micrometres).

The blinking cycle does not affect only the aqueous layer of the tears. Namely, on top of the aqueous layer there is the last protective barrier of the eye surface – the lipid layer of the tear film [18-19]. The lipid layer further decreases the surface tension of the tear film, enhancing even more the potent spreading of the tear film after a blink (Figure 4) [20]. The lipids are believed to act together with lipocalin proteins when forming the surface layer of the tear film after the blink.

The lipid layer experiences very different dynamics than the aqueous layer of the tear film. The aqueous layer is replaced by a new solution almost every blink of the eye, while it is transferred to the lacrimal ducts [21]. The lipid layer instead stays the same a long time, and is replenished with fresh meibomian secretion only when needed, during the blink.

1.2.2 Composition and Structure of the Tear Film Lipid Layer

There are only a few studies about the structure, composition, dynamics, and function of the tear film lipid layer (TFLL). What is known, though, is that the TFLL indeed exists, meaning that the lipids of the tear film really do separate to a lipid layer at the air-water interface of the surface of the eye and do not form an emulsion with the aqueous layer of the tear film [21]. The thickness of the lipid layer is unknown, although there are some guidelines suggesting the normal thickness of TFLL to be around 10-100

nm [18, 22]. However, some studies have shown that already a thickness of ~50 nm could cause the dry eyes symptoms [23].

The TFLL consists of a variety of different kinds of lipids, most of which are secreted by the meibomian glands inside the upper and lower eyelid [23-26]. Both eyelids contain dozens of meibomian glands, and the glands empty their fatty secretion right next to the eyelashes [2-3]. It has been debated if the lipid layer serves to further decrease the evaporation of the aqueous tears, as it spreads on top of the aqueous layer, but no conclusion in that matter has been reached [18-19,30-34]. It is also not known whether the lipid secretion has an impact to the refraction of the surface of the eye [6]. What the lipid layer does in any case, however, is that it prevents the aqueous tears from escaping the very eye surface to the eyelids and cheeks, and it also prevents water evaporation between closed eyelids when we sleep [19,23,24, 28-34]. It furthermore lowers the surface tension of the tear film, allowing the moist aqueous layer to be spread onto the whole eye surface [20, 36-37]. Yet, the role of the TFLL remains elusive as very recent evidence has shown that the TFLL might not retard the evaporation of the tear fluid [31].

1.2.3 Detailed Lipid Composition of the Tear Film Lipid Layer

Recent data suggests that the TFLL contains some wax esters, triglycerides, possibly some cholesteryl esters, and some free fatty acids and lysolipids, but nonetheless most of the lipids are common phospholipids [25-26] (Figure 5). The main difference in the composition of the meibomian gland secretion and TFLL lipids is that the TFLL contains a lot more phospholipids.

Meibomian gland dysfunction increases evaporation of water from tear film [40] by impairing the functionality of TFLL, so the neutral lipids produced by meibomian glands (triglycerides and cholesteryl esters, among others) have to be crucial for maintaining the balance of the tear film.

However, the amount and importance of phospholipids in the lipid layer has been widely discussed recently. It has been proposed that lack of phospholipids could drastically make the aqueous layer of the tear film thinner, and could thus be associated with a higher water evaporation rate in the eye surface [41-42]. This is a quite new hypothesis, as the traditional view has been that mainly the thickness, not the composition of TFLL, is crucial for maintaining the balance of the tear film [23].

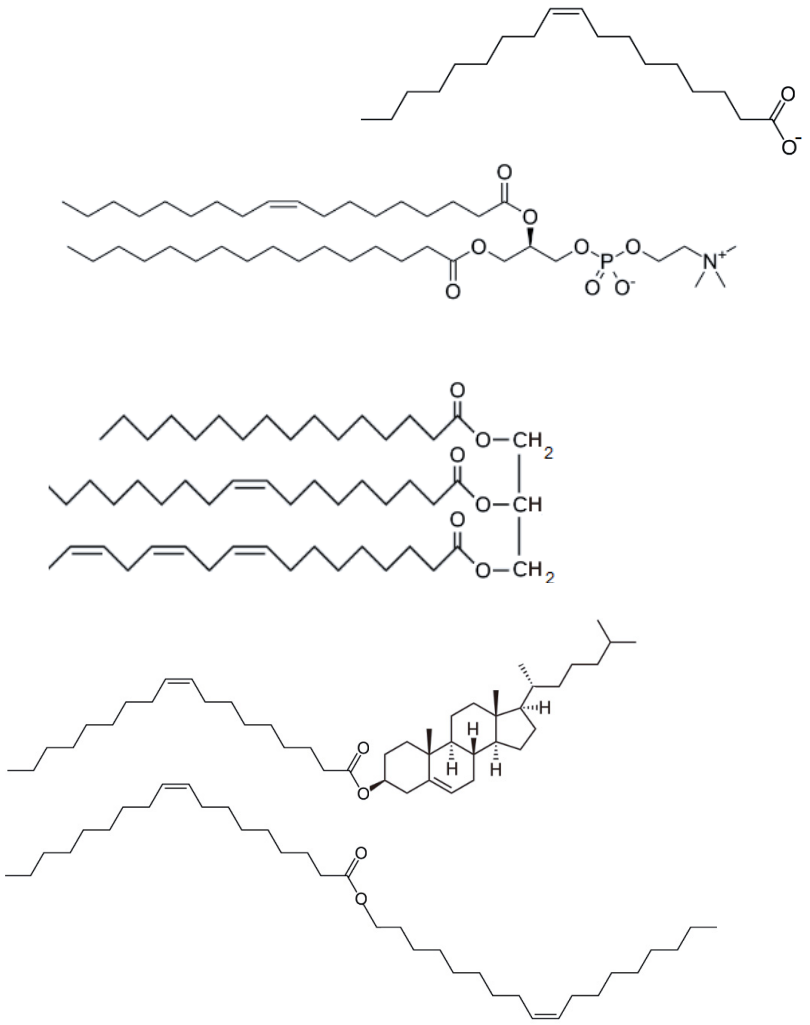

Figure 5. Structures of TFLL lipids. From top down: free fatty acid (FFA, here oleate in deprotonated form); phospholipid (phosphatidylcholine (PC)); triglyceride (TG), cholesteryl ester (CE, here cholesteryl oleate (CO)); wax ester (oleyl oleate). Figure modified from Wikipedia commons.

1.2.4 Models for the Structure of the Tear Film Lipid Layer

The organization of the lipids in the TFLL is not random, but the layer is known to be organized into a layer-like structure [43]. The most common model for the structure is a multilayer, where phospholipids lie at the very interface of lipid and aqueous phases and more hydrophobic lipids reside closer to the air interface, and the tails of lipids in these layers overlap partially (Figure 6) [28,44-46]. Recent mass spectroscopy data of the

composition of tear film [26] suggests, however, that there are much more phospholipids in the mixture than there could be in this kind of layer. Namely, combining the multilayer model to the approximated thickness of more than 50 nm of normal tear film layer leads to a lipid composition where most of the lipids would be non-PL lipids (non-phospholipids). These kinds of lipid compositions are seen only in patients, not in healthy individuals [41,47]. So, the layer could instead of a single multilayer consist of one or several bilayers (or bilayer-like structures) of phospholipids and non-polar lipids with possibly some bulk non-polar lipids between bilayer leaflets and at the very air interface. Or, the layer could be a simple monolayer-like structure with some more hydrophobic lipids in the layer and some bulk non-polar lipids at the air interface.

Tear film also contains a lot of lipid binding proteins, among them tear fluid lipocalins [48]. The role of these proteins as co-surfactants in the TFLL is unknown, but it may be that lipocalins indeed function as an integral part of the lipid layer of tear film. The other option would be that the lipocalins are mainly part of the aqueous phase of the tear film. Further investigation is needed to clarify the role of lipocalins in the tear film.

In the present study, I have investigated the properties of lipid monolayers or monolayer-like structures having the composition of TFLL. These studies have been carried out by molecular dynamics simulations using coarse-grained molecular models to elucidate the behavior of these lipid mixtures in the air-water interface. The simulation systems included only the lipid components, and no proteins.

1.2.5 Dynamics of the Lipid Layer

One important feature of a tear film lipid layer is its very dynamic character – it is squeezed to the very edges of eyelids during blinking of the eye, and as the eye is opened after a blink, it slowly, within one second, returns spontaneously to cover the whole eye surface once again [13-14].

It seems that during this process all the lipids need to stay in the lipid layer and avoid being pushed into the aqueous phase, since when lipid vesicles are seen in the aqueous phase, they are in seconds recycled from the eye surface via lacrimal ducts [21]. So, losing lipids to the aqueous phase essentially causes a loss of lipid in the tear film. Accordingly, the dynamics of the tear film, and its lipid layer, plays a crucial role in maintaining the functional state of tear fluid. The tear film should be very elastic and able to compress massively during blinking while still maintaining its structural

integrity and ability to regenerate the continuous lipid layer to the eye surface quickly after opening the eyes.

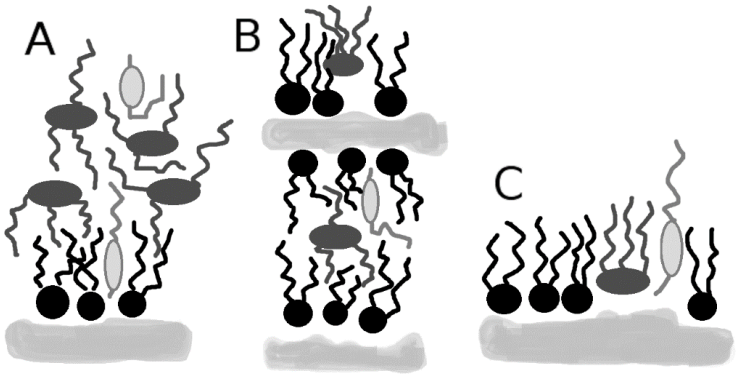

Figure 6. Proposed models for TFLL at an air-water interface. A) Classical multilayer model. B) Multilayer model describing a more phospholipid-abundant lipid composition. C) Monolayer model. Colour code is as follows: Cholesteryl esters (light grey), triglycerides (dark grey), phospholipids (black), and water (grey). Air is on top, while water resides at the bottom.

During the down blink, up to certain lateral pressure, the TFLL is assumed to be in liquid state, and to form folds or multilayer structures to handle the decrease of the interfacial area (Figure 7). After reaching a limiting pressure, TFLL is then believed to turn into a super-compressed state, where it can maintain the disorder of liquid state, but resist further conformational changes due the solid-like compressibility of the system [28]. If the folding of the system is not proceeding efficiently enough, or the super-compressed state is not reached during the compression, disintegration of the lipid layer can take place.

The folding, i.e. the collapse, of the lipid layer is commonly believed to begin with layer weakening, when little kinks, or ripples form to the layer as the layer is compressed [49]. The ripples then mature to produce lipid layer folding [50] – for example PC (phosphatidyl choline) monolayers fold on the hydrocarbon side of the lipid to form “bilayer-like” protrusions to the water side of the membrane (Figure 7) [51]. Upon further compression, the layer becomes very unstable, and the bilayer-like parts elongate and can eventually bend back to face the monolayer they grow away from [52]. At that point they could possibly detach from the membrane via a vesicle formation process. If the bilayer part formed in this manner does not bend, it could detach during increased compression in the non-bent form too – in that case the resulting lipid assembly would be a micelle. A third possibility could be, if the monolayer included non-polar lipids like triglycerides, that the membrane-detaching particle could resemble lipoprotein particles,

having the non-polar lipids in the “core” of the particle, while the phospholipids would reside on the surface.

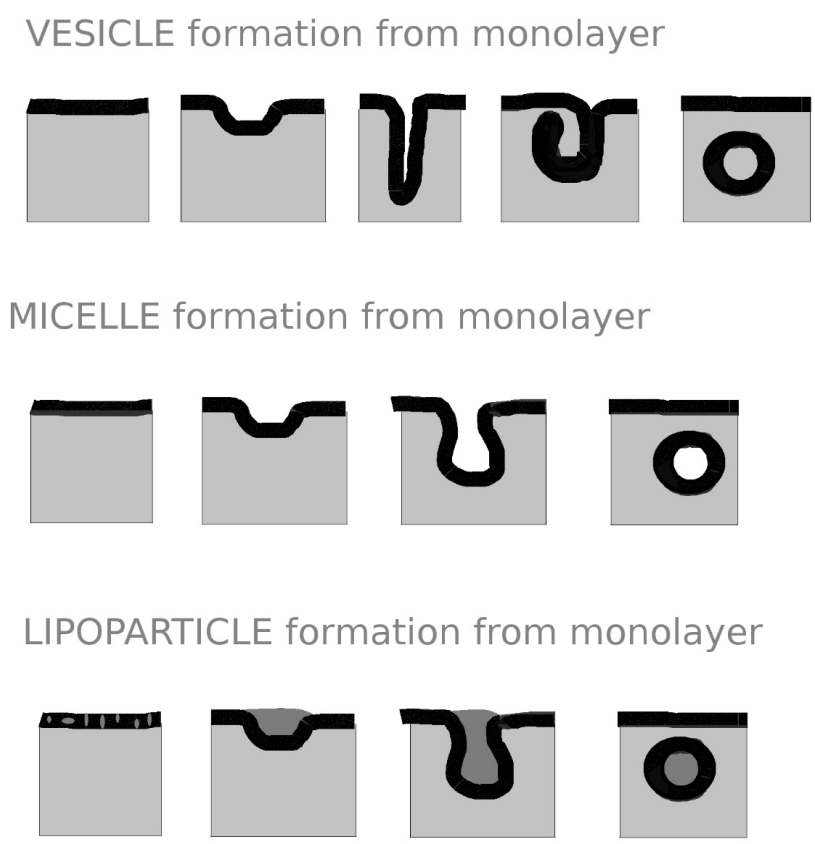

Figure 7. Schematic models for monolayer collapse. Vesicle formation craves folded structures’ bending, and subsequent stalk formation or related phenomena. Micelle formation craves stalk formation or related phenomena. Lipoparticle formation via this mechanism is rather improbable, as the sides of the bent PC lipid layer are not in close contact with each other, but instead are separated by a thick layer of neutral lipids.

1.3 Dry Eye Syndrome

As the moist tear film protects the cornea, and especially the corneal epithelium at the very air-cornea interface against inflammation, debris, and drainage. And indeed: the malfunction and abnormalities in the systems maintaining the balance of tear film can cause clinical symptoms.

The common name for the failure of the tear film to cover the whole surface of the eye is called “the dry eyes syndrome” (*keratoconjunctivis sicca*) [53-56]. Normally the air-cornea contact in the corneal epithelium

happens ~7 seconds after blinking as the moist tear film abruptly breaks up and suspects the corneal epithelium tissue to air contact, but in the dry eye syndrome this time is diminished to ~2 seconds [14]. Normally we just simply blink again, already before the tear film break-up happens, but in the dry eyes syndrome that is not the case as the tear film breaks up before the next blink.

1.3.1 Symptoms

The first step of dry eyes is tear film thinning, or even the breakup of tear film [10,34,57]. The dry eye patients feel this as a painful sensation – they describe "burning" of eyes, and a feeling of "having sand in the eyes". Not all patients feel any pain, however [60].

This primary tear film break-up of dry eyes causes vision blurring due to aberrations in the tear film surface bending the light to the retina [61]. Also, as the corneal epithelium is exposed to air contact, it causes irritation and inflammation of the eye [62, 53-56]. This is probably caused by exposure of the epithelial cells to a situation where there are high amounts of aqueous tear-soluble molecules on eye surface, with only a small amount of water to host them. This situation is called hyperosmolar stress. The chronic exposure to hyperosmolar stress results in inflammatory response at the eye surface, leading to secretion of various pro-inflammatory cytokines such as the IL-1 (interleukine 1), -6, and -8 as well as TGF-β1 (transforming growth factor β1) and TNF-α (tumor necrosis factor α).

The inflammation is the crucial driving force for the development of the clinical dry eye syndrome. The inflammation namely damages the tear film maintenance system at the eye surface (e.g. lacrimal and meibomian glands), and this further increases the magnitude of the dry eye symptoms [53-56]. In severe dry eye cases this gradually impairs even the production of reflex tears in conditions of ocular stress (like low humidity, difficult visual task, or smoke in the air), and exposes the eye surface to environmental hazards [63]. The dry eyes syndrome is thus primarily an inflammatory disorder, and often several anti-inflammatory treatments (using e.g. corticosteroids or cyclosporine A) are needed to interrupt the notorious cycle of the dry eye disease related inflammations [64-66].

The syndrome is a chronic disorder, so once the dry eyes have developed, it will follow the patient for the rest of his life. An untreated dry eyes syndrome can lead to scarring and damage of cornea, permanently affecting the vision [53-56]. However, even the dry eye patients receiving treatment

for the syndrome experience lower life quality due the blurred vision, corneal pain, and eye inflammation [67].

1.3.2 Etiology and Treatment of Dry Eyes

There is no single cause of the dry eyes syndrome. The complex system of tear film production and balance can break up at any part of the system. This can be caused by various secondary reasons, like autoimmune diseases such as Sjögren's syndrome [68-71], inflammation of the eye due to viral, bacterial, or fungal infection, or physical trauma [53-56, 64-66]. Also hormonal balance [72-74], nutrition [75-79], and daily habits (like use of computers) [80-90] affect the balance of tear film.

In some cases the primary cause of the tear film imbalance is lack of mucus to bind the water to the eye surface. This is the case for example in the autoimmune disease known as Sjögren's syndrome, where many of the goblet cells producing the mucus for the tear film die [68-71]. This causes inadequate lubrication of the eye surface due to high evaporation of the aqueous tears. In other types of dry eyes there is instead too much mucus in the tear film, generating too viscous tear films, which impairs the efficient spreading of the layer to cover the whole eye surface after the blink [53-56]. Also the lacrimal gland can be dysfunctional, or its hormonal control can be altered, leading to a too small amount of aqueous tears to provide a thick enough water-rich layer to cover and protect the eye [91-92]. This happens often to women after the menopause. Also the meibomian glands within the eyelids might be affected – for example in eyelid margin inflammation (blepharitis) the inflammation swells the eyelid margin, and the meibomian gland orifices begin to touch the tear film surface continuously, causing too much lipid secretion to the tear film. This alters the lipid composition and functionality of the tear film. In other types of dry eyes there can be impaired lipid secretion instead [23,25,40,47,93].

The cause of the dry eyes syndrome needs thus to be investigated carefully before assigning the treatment, to ensure that the right kind of eye drops, which are the primary treatment for the syndrome, are assigned to the patient [94-95]. Some drops contain a lot of mucus-mimicking molecules, others are lipid-rich, and many only compensate for the loss of aqueous tears [96-97]. Lack of aqueous tears can also be treated surgically by inserting a silicone plug to the corner of the eye, to prevent the aqueous tear clearage via the nasolacrimal duct. Other non-medicinal treatments include wearing swimming goggles on a daily basis, to prevent the evaporation of the tear film, manual removal of extra lipids from the layer when needed,

and vitamin A and omega-3 fatty acid intake in the diet, which might decrease the severity of the symptoms [94-95].

In any case, it is improbable that the symptoms fully vanish, as the dry eyes syndrome is a chronic disorder.

1.3.3 Risk Factors for Dry Eye Syndrome

The main risk factors for the dry eye syndrome are older age [98], female sex, connective tissue disease, use of medications such as beta-blockers, diuretics, and tricyclic anti-depressants, computer use [82-83], and use of contact lenses [84-90].

From these the old age is the most natural, as when we age, our body can simply fail us and cause us many peculiar conditions. Also, as mentioned, after menopause the altered hormonal secretion can cause inadequate secretion of aqueous tears in women [74, 91-92, 98].

The office workers – the users of computers – are at risk as well, as when we stare at the computer screen, our reflex blinking frequency diminishes [82-83]. This happens as our visual system detects a difficult visual task, and prioritizes high quality visual data production instead of maintaining prime quality tear film via blinking. We blink even four times more seldom than normally when we work with computers. The blinking rate restores itself as soon as we stop looking at the computer or TV screen. The more rare blinking when using computers suspects us to the tear film break-up between the blinks. If the low blinking frequency continues more than 3 minutes, it further affects the tear film composition, and diminishes the tear film break-up time [99]. So – in the end we do not only blink more rarely, but the tear film breaks up faster between the blinks. This causes eye irritation among the office workers, and many of them develop the dry eye syndrome [82-83, 99].

The third risk factor of the dry eye syndrome, the wear of contact lenses, is a more straightforward cause [84, 89]. As the contact lens is a foreign body, it can cause irritation of the eye surface, or even mechanical damage to the eye structures [85-86]. The lens can also adsorb tear film proteins, lipids, and mucins onto its surface, causing aggregation of the tear film components [87-88, 100]. These effects can then cause inflammation in the eye surface, which easily leads to dry eye symptoms. Also the impaired flow of oxygen to the eye surface tissues causes stress to the cornea, as the lens prevents the free flow of oxygen from air to the tissue [86-89]. The tear film secretion system is under higher stress when wearing contact lenses as well – the tear film needs to be produced both under and above the contact lens,

and the lacrimal gland needs to provide more tears than normally. Wearing contact lenses is thus prone to cause eye inflammation, and it also pushes the tear film maintenance system to its limits, as a larger surface needs to be lubricated with a smaller supply of oxygen [86-89, 100]. These factors contribute to the high prevalence of dry eyes amongst contact lens wearers.

2. Relevance and Basis of Molecular Simulations in Physics

In the previous Chapter, we discussed the clinical and biological motivation of this work. Here the focus will be shifted to the physics of the system of interest. We introduce the concept of "molecular dynamics" as a molecular simulation method based on physics that is useful to model molecular scale systems and their evolution in time. We will see how molecules and their movement can be described by the means of mechanics, electrostatics, thermodynamics, and statistical physics. We also consider comparisons between experimental and simulation approaches in investigating molecular systems. Moving on, we also introduce some fundamental concepts of physics that underlie the molecular dynamics simulation approach.

2.1 Simulations as a Tool to Validate Laws of Nature

Experimental science is the corner stone of natural sciences. For any given system or process studied, experiments result in a variety of different kinds of data sets. The interpretation of these requires the data to be analyzed with mathematical tools, and to be interpreted with physical models. Understanding the physical basis of experimental data is based on models, each based on a set of assumptions, and the one providing the best fit to experiments is then possibly the model able to describe the process in question. The aim of the chapter is to illustrate how to find and use the laws of nature that describe complex processes in strongly interacting many-particle systems, and how to combine these to create a basis for a simulation model.

Simulations are based on scientific knowledge of how nature works through the interactions between the components comprising the systems

in question. Simulations allow one to ask the intriguing question: What is the simplest possible model able to describe the experimental findings?

2.1.1 Pros and Cons of Simulations in Biomolecular Research

Simulations have several strengths. One of them lies in their ability to render "virtual experiments" possible, meaning that one can do simulations of phenomena that would not be appropriate as experiments in real life, such as how toxins would affect the function of receptors in cells of human beings, or what happens on molecular scales in a processes where the resolution of even the best possible experimental techniques is too limited. On the other hand, by simulating and analyzing various kinds of simplified models, one can reach valuable information of the function and properties of real world systems [101-102]. With the simplified models one can easily create "ideal conditions" that experimental researchers just try to reach. In simulations "ideal conditions" are always a true possibility, opening new vistas in the field of basic research.

The "computer experiments" done through simulations can also play a major role in overcoming the limitations of experimental methods – for example in the case of very small or very big systems (nanometers, kilometers), or when extremely rapid or slow phenomena (nanoseconds, thousands of years) take place [102-105].

In molecular biology there are several reasons to conduct simulations, thereby complementing experimental research. One significant asset for simulations is the relatively low cost. In a cell biology laboratory the cost of samples can be of the order of 100-1000 euros per day, per researcher (this holds especially if costly reagents like modified ATP-nucleotides, molecule-specific antibodies, or expensive biological material such as dissected mouse tissue is used on a daily basis), with additional costs of the needed analysis methods (purification kits, sequencing services, etc.). Many of the analysis stages of biological samples are also very labor-intensive, and thus also the salary expenses are significant. Meanwhile, in simulations the cost of these "samples" is more reasonable since the main expense is the computational time – simulation studies are not very labor-intensive since most of the work is done by computers. In Finland, and in many other countries, the supercomputing centers are supported by public funds (as they provide resources not only for research, but also for example for calculating the mathematically complex and computationally costly meteorological data for daily forecasts), and the use of those services is free of charge, or has a very low cost for academic users. To conclude – if

infrastructure is assumed to exist, computational research is cost-effective, as labor costs are low, and no new reagents need to be bought – the main pre-requisite for "computational experiments" being the computing environment itself.

If we further consider sample preparation, purification, and analysis in a typical experimental laboratory, it is usually time consuming and resource demanding. The investigated molecules also usually have a rather limited lifespan in experimental setups – some marker molecules can last intact in fluorescence measurements only for a couple of seconds, and most purified protein samples are usually stored in -70 degrees Celsius, when not needed, as they slowly change conformation and denature in room temperature. So, to conduct experiments for one hour, one sometimes needs to purify and extract the system of interest for weeks. While the purified material can often be stored in a freezer and used bit by bit, the amount of preliminary work is yet quite substantial. In simulations, the molecules, once created for the first time, remain "functional" forever, and can be used in any setting over and over again, easily, and with no additional cost.

Another major advantage of biomolecular simulations is the absence of "marker molecules". In experimental setups one often uses non-biological molecules, for example fluorescence probes, to probe the measured systems (see below). Possible alternatives to replace marker molecules are often even more problematic, such as the use of solid support or consideration of biomolecular systems in their crystalline phase, which usually alter the structure of the system significantly.

The probe molecules can cause artifacts in the system, and the measured properties can be biased by the addition of this non-natural substance to the sample. In simulations one needs no such molecules, as the structure and dynamics of all molecules and their surroundings can be traced and elucidated in detail, without adding any markers. In fact, simulations have been widely used to quantify and test how big perturbations one induces to the molecular systems when investigating them with probe molecules, by comparing the behavior of the simulation systems with and without the marker molecule in question [106-110]. Also the effects of experimental conditions to the sample can be simulated. Many setups release free radicals, for example, which can oxidize the lipid molecules present in the sample. Simulations of bilayers containing oxidized lipids have revealed how dramatically this kind of experimental setup can alter the properties of the lipid layer investigated during the experiment itself [111-113].

Simulations are also practical in investigating the effect of modifications to small biomolecules – they can be used to probe the molecular systems, without the need of right away using expensive experimental setups.

Mutations to peptides, and in enzyme active sites, and efficiency of drug binding to cell membranes can be investigated first in simulations, to guide experiments [114-116]. However, these predictions are often times far from exact. They can be used as guidelines, but not all predicted properties can be seen in experiments, and not all experimentally predicted properties can be observed in simulations. Also, some important phenomena, for example large protein conformational changes due to point mutations are still out of reach for simulations [117].

While the role of simulations in making predictions is increasing, a great fraction of simulation work is yet based on explaining what really happens and why, thereby providing insight into the processes earlier studied in experiments. That is, one major objective of simulations is to shed light on phenomena previously observed in experiments, by simulating the very system used in experiments, or a simplified one if the native one is too complex for simulations. This is true in all simulation fields, from semiconductor research to clinically relevant biological processes.

However, this does not completely rule out the power of simulations in finding new phenomena or molecular properties – especially many subtle changes in the properties of the system (like imperfections in solid state crystal structures, or subtle changes in the binding pocket of an enzyme) can be first found in simulations, and only later verified in experiments. The simulations then follow the idea that "if the world looked like this, then what would happen" – if there were such an imperfection in the crystal structure, then what would its effect be on material properties, and if there were such a change in the binding pocket, then how would the drug binding change.

As for further limitations of computer simulation models, there is reason to keep in mind that the interpretation of simulation results requires care: one needs to keep in mind the peculiar nature of all simulation models as incomplete but ideal descriptions of the system. So, the researcher needs all the time to keep in mind which properties are described in the system and which are not, and on which accuracy one can model the system. One can draw conclusions only about properties included to the model, and nothing else, and only in the accuracy inbred in the model. This is possibly the biggest drawback of simulations – quite often the simulation world is not able to reproduce the world as we experience it – it is always a model, and we cannot be sure how accurate the model is. The description of the molecules of the system is idealized, and thus does not necessarily reproduce (all) the properties of the true system with meticulous detail. In addition to this, the simulation timescales for molecules are usually in a range of nanoseconds to microseconds, when experiments for the same

systems can last from seconds to hours. Also the length scales differ – in molecular simulations it is not possible to reach dimensions larger than dozens of nanometers, while there are no such limitations in experimental setups. These limitations of simulation studies are discussed in detail in Chapters 2.1.2 and 3.3–3.9, where the molecular dynamics simulation practices are reviewed. Related questions are also discussed in Chapters 5–8, when we discuss the simulation methods, results, and analysis of the work conducted for this Thesis.

2.1.2 Analyzing Simulation Results, and Comparing Results to Experimental Data

The analysis of the results of simulation data is not completely similar to the analysis of experimental data. The errors of experimental results are usually due to imperfect sample preparation, side effects caused by some interfering phenomena, too small data sets, or selection of wrong kind of analysis tools for the data. Meanwhile, in simulations the errors quite often rise mainly from imperfect descriptions of the simulation system itself, and approximations and errors made in the data production phase (simulation).

When comparing simulation results to experimental data, one also often faces scale differences. Simulation systems are usually several orders of magnitude smaller than experimental systems (micrometers vs. centimeters), and simulation time is much shorter than in an experimental setup (microseconds vs. milliseconds, or even hours). This is good to keep in mind, as the same physical phenomena can look very different when monitored in different time and length scales. For example in very small lipid layer systems (in simulations) one cannot see undulations of the membrane at all, as the membrane patch is so small [118]. For very big membrane systems (considered in some experiments) the undulation is not clearly visible, either, as one cannot monitor properties such as the thickness of the membrane, but one can measure only more crude properties [118-120].

Another intriguing topic where simulations and experiments contribute in different ways to unlock related questions deals with so called “lipid rafts”. They are currently considered as self-organized functional nanoscale membrane domains rich in cholesterol and sphingolipids. These domains are seen to spontaneously form in planar lipid membranes in molecular dynamics simulations [121-125]. The idea that these rafts really exist in planar membranes can be debated, as some experimental results nowadays point to the direction that these assemblies form as a response of

differences in the curvature of the lipid membrane [124]. However, in experiments it is difficult to measure lipids in nanoscale, and in short timescales, which are the time and length scales the simulations operate at – the lipid raft domains in planar lipid membranes, if they exist, seem to be too transient and too small to be detected by the current experimental methods. In simulations, on the other hand, the experimental result showing the formation of lipid rafts in curved - instead of planar - membranes is hard to reproduce, since the sizes of even small liposomes or other curvature-containing lipid systems are quite big given the computing resources that are usually available [125].

2.2 Molecular Dynamics – How to Describe the Movement of Particles

2.2.1 Essence of Molecular Dynamics

In describing the movement of molecules, one commonly used way of carrying out the task is called “molecular dynamics” (MD) simulations [102, 126-129]. The particles of classical MD simulation are atoms, or groups of atoms, having simple properties like a size, charge, and bonds to other atoms.

In MD ones needs mathematical formulae from statistical and classical mechanics, electrostatics, and thermodynamics. Classical mechanics is needed to describe the behavior of atoms and molecules, creating for example bonds between atoms, and particle sizes and the ability of particles to move and experience forces. Electrostatics is needed to add the property called “a charge” to the model, to enable modeling of non-uniform electron distributions inside molecules, to account for the net charges of molecules, and consequently to computer interactions between charged and/or polar molecular groups. Statistical mechanics is needed to define quantities like “pressure” or “temperature” on molecular scale where those properties cannot be measured as such, but a statistical model is needed to evaluate them.

To implement the above descriptions, one further needs other techniques, some that one cannot solve exactly, but the solutions may be approximate and based on computer algorithms [130]. The most evident of the approximate quantities is “time”. As simulation describes a model that is a

simplification of real life, so also it is not obvious that the time in a simulation model is fully consistent with real time as we experience it. In more practical terms, first of all, in MD simulations time is not continuous but discrete, given as a number of time steps, each of which is typically a few femtoseconds. Second, even if the discrete nature of time were not a problem, then one has to worry about the accuracy of describing interactions between the many atoms/particles (so called force field), since the accuracy of the force field largely determines how closely the dynamics of the simulated model matches the dynamics of a real system, which the model aims to mimic.

There are multiple different MD software packages developed to run the time development of these kinds of simple systems [131-135]. Each of these programs is based on a similar way of interpreting "time", but the details in time evolution may differ depending on how the system is described. Each program can have one or multiple ways of controlling the evolution of system volume and pressure (via so called thermostats and barostats) and other properties such as surface tension. The most important and also the most variable part of the model simulated by software packages is the description of atoms and molecules and their interactions (the above mentioned force field) – we discuss these topics one by one below.

2.2.2 Newtonian Mechanics

Mechanics is the branch of science concerning the behavior of physical bodies that are subjected to forces. If we are also interested in the movement of particles in time, we are talking about "dynamics". When we deal with the dynamics of molecules, we talk about "molecular dynamics". In molecular dynamics our aim is to elucidate how individual molecules and their positions evolve in time. For a more thorough presentation of related topics overall, an interested reader is advised to have a look at appropriate literature [136-137].

When particles are in motion, every one of them has a mass (m) and a velocity ($\mathbf{v}$). Velocity is given by the speed of the particle together with its direction of movement. Together these two quantities give rise to a quantity known as momentum ($\mathbf{p}$) :

$$\mathbf{p} = m\mathbf{v} \qquad \textbf{(1)}$$

The speed of a particle and its direction remain the same, if the particle does not experience any external force. This is the so-called Newton's 1st law. If there is an external force **F** acting on the particle, the force causes a change in the momentum (d**p**), which is linear in time (d**p**/dt). If the mass of the particle does not change, the change of velocity due to the force is linear in time (d**v**/dt). This is called the Newton's 2nd law :

$$\mathbf{F} = \mathrm{d}\mathbf{p} / \mathrm{d}t \;=\; \mathrm{d}(m\mathbf{v} / \mathrm{d}t) \;= m(\mathrm{d}\mathbf{r}^2 / \mathrm{d}t^2) = m\mathbf{a} \qquad \textbf{(2)}$$

where **r** is the spatial coordinate of the particle and **a** is the acceleration of the particle. Here we are interested only in systems where the masses of the particles do not change – so instead of monitoring momentum changes, we can monitor changes in velocities.

The laws of Newton are very simple. They seem to be a property of our world the way we perceive it, as long as the speed of particles is sufficiently small compared to the speed of light, to avoid any need of taking relativity effects into account. All everyday phenomena follow Newton's mechanics – only on very small length scales (inside atoms) and very long length scales (in space) we need to lean on more advanced descriptions of the movement of particles.

2.2.3 Energy

Now let the force move the particle a certain distance (**r** - $\mathbf{r}_0$) from point $\mathbf{r}_0$ to **r**, and integrate that path to get the total "effect" that the force exposes to the particle. We will now define this effect as the work (W) :

$$\begin{aligned} W \;&=\; \int_{r(t_0)}^{r(t)} \mathbf{F}\mathrm{d}\mathbf{r} \;=\int_{t_0}^{t} \mathbf{F}(\frac{\mathrm{d}\mathbf{r}}{\mathrm{d}t})\mathrm{d}t \;=\int_{t_0}^{t} \mathbf{F}\mathbf{v}\mathrm{d}t \;=\int_{t_0}^{t} m\frac{\mathrm{d}\mathbf{v}}{\mathrm{d}t}\mathbf{v}\mathrm{d}t \\ &= m\int_{t_0}^{t}\left(\frac{\mathrm{d}\mathbf{v}}{\mathrm{d}t}\mathbf{v}\right)\mathrm{d}t \;=\; \frac{1}{2}m\left(v_t^{\,2} - v_{t_0}^{\,2}\right) = \frac{1}{2}m\Delta v^2 \end{aligned} \qquad \textbf{(3)}$$

The force thus produces a change having a form of $(1/2)mv^2$. This is the definition of the kinetic energy K. Like this, the change due to the force is the difference in kinetic energies between the beginning (t_0) and the end (t) of the action of the force:

$$W = K\text{-}K_0 \qquad \textbf{(4)}$$

If the work done during the path ($\mathbf{r} - \mathbf{r}_0$) does not depend on the path along which the particle moves, it is said that the force causing the movement is conservative. This kind of force is independent of time. The resulting potential (U) has a certain strength in each point of space $\mathbf{r}$.

The change of the potential gives the force acting in that particular point:

$$\mathbf{F} = -\nabla U \tag{5}$$

Now, from the integral of work, only the initial and final points of the path remain:

$$W = \int_{\mathbf{r}_0}^{\mathbf{r}} \mathbf{F} d\mathbf{r} = -U_{\mathbf{r}} + U_{\mathbf{r}_0} = -U + U_0 \tag{6}$$

So, now we have two definitions for the work W, and we can combine them as follows:

$$W = K - K_0 = -U + U_0 \Leftrightarrow K + U = K_0 + U_0 = E \tag{7}$$

We have accomplished to define the energy E. The total energy of the system is thus a property, which does not change when forces are applied to particles. When forces act on particles, the system changes, but the total energy, and also the total momentum stay constant. This applies to systems, which do not interact with their surroundings, and are not under the influence of a field (like electric or gravitational field). The shape of the particles is also assumed to stay constant at all times.

In molecular dynamics we simulate systems with no surroundings. Thus if no further modifications are made, one simulates a system with constant energy E. However, we can modify the simulation conditions to generate other kinds of environments to replace the case of constant energy with conditions for constant temperature or constant pressure. These modifications are reasonable and also justified if they allow one to better model the conditions in experiments. Actually, they also do so, as systems experiencing constant pressure, and constant volume are prevalent in nature. In experimental setup, the constant pressure case is basically an experiment conducted in an open container, and the constant volume case is conducted in a closed container. It is also very tedious to try to insulate the experimental system so well, that constant energy conditions (which are the easiest to reach in simulations) could be reproduced reliably.

2.2.4 Interactions in Molecular Systems – Bonds, Angles, Dihedrals

To simulate molecules, one needs a way to describe the conformational degrees of freedom for a given molecule. In practice this implies that one should have means to describe the bonds and angles between atoms in molecules, and also the bond rotation barriers [102, 126-129].

The bonds and bond angles can be approximated as springs, having a certain spring constant. A simple harmonic oscillator is well suited to describe the minor changes in bond lengths and angles, as long as those reach values rather close to their equilibrium length. Harmonic oscillators cannot thus be used when chemical reactions are considered, but they are quite suitable to investigate the physical properties of the system when chemical reactions are not involved.

A harmonic oscillator describes, simply, oscillatory movement around an equilibrium position, i.e. around the minimum of a potential energy function. The system is assumed to show similar oscillatory behavior at all times.

If one monitors the one-dimensional displacement of the position of a particle under consideration, compared to its equilibrium position, and denotes its equilibrium position by h_o and its current position as h, then one gets for the displacement x:

$$x = h - h_0 \tag{8}$$

and can write the potential U to a Taylor series around equilibrium position h_o as :

$$U(h) = U(h_o) + \frac{1}{1!}\frac{\mathrm{d}U(h)}{\mathrm{d}h}|_{h=h_0}\left(h-h_0\right) + \frac{1}{2!}\frac{\mathrm{d}^2U(h)}{\mathrm{d}h^2}|_{h=h_0}\left(h-h_0\right)^2 + \ldots \tag{9}$$

Here we choose the potential energy and the spatial coordinate to be zero at h_o , and as we also assume the first derivative of U with respect to position to be zero (potential minimum at h_0), we get an approximation

$$U(h) = \frac{1}{2!}\frac{\mathrm{d}^2U(h)}{\mathrm{d}h^2}|_{h=h_0}\left(h-h_0\right)^2 \tag{10}$$

This implies that we can employ the harmonic approximation providing us with a description

$$U(x) = \frac{1}{2}kx^2 \tag{11}$$

where the so-called spring constant k is

$$k = \frac{\mathrm{d}^2 U(h)}{\mathrm{d}h^2}\Big|_{h=h_0} \tag{12}$$

The spring constant k represents the stiffness of the spring described by the potential.

The formula above can easily be modified to provide a more generic description of the bonding potential between two atoms/particles to oscillate around their equilibrium length:

$$U(r) = \frac{1}{2} k_{bond\,i,j} (r - r_0)^2 \tag{13}$$

where i and j are the atoms/particles connected via the bond, r is the distance between the two atoms/particles i and j, and r_o is the corresponding equilibrium bond length (Figure 8).

As the force in equation (11) is a function of the position only (conservative force), the strength of the force arising from this potential can be calculated by a simple derivation

$$F = -\frac{\mathrm{d}}{\mathrm{d}x}\left(\frac{1}{2} k x^2\right) = -kx \tag{14}$$

where x is now the displacement from the equilibrium position. Equation (14) now shows that the force follows Hooke's law, the force being linearly proportional to the displacement.

The corresponding force acting on the atom/particle i is now thus

$$\mathbf{F}(\mathbf{r}) = -k_{bond\,i,j}(\,|\mathbf{r}| - r_0)\,\frac{\mathbf{r}}{|\mathbf{r}|} \tag{15}$$

Angle potentials can be formed similarly, by modeling the angle bending as a harmonic potential around the equilibrium bond angle (Figure 8).

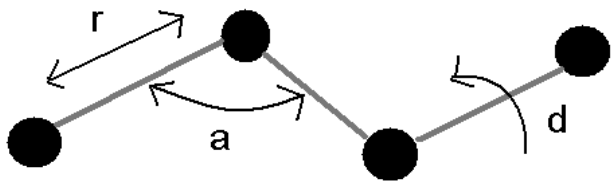

Figure 8. Molecule with bond vibration (r), angle bending (a), and dihedral rotation (d).

The potential function for the angle *a*, formed by atoms *i-j-k* is :

$$U(a_{i,j,k}) = \frac{1}{2} k_{angle\ i,j,k} (a - a_0)^2 \quad \textbf{(16)}$$

Rotation around bonds can be similarly represented by a dihedral potential with an angle *d*, which describes the angle between two planes: the plane 1 formed by the atoms *i-j-k*, and the plane 2 formed by the atoms *j-k-l*:

$$U(d_{i,j,k,l}) = \frac{1}{2} k_{dihedral\ i,j,k,l} (d - d_0)^2 \quad \textbf{(17)}$$

To avoid confusion, here d and d_o describe the time dependent and equilibrium angles in a generic manner, respectively. The harmonic dihedral potential can represent only one minimum energy conformation for a rotation around a bond, however in many cases one would need several minima. Often a cosine potential is used instead of a harmonic potential to create multiple minima in the dihedral potential:

$$U(d_{i,j,k,l}) = k_{dihedral} \left(1 + \cos(nd\text{-}d_0)\right) \quad \textbf{(18)}$$

where the parameter n gives rise to multiple equilibrium configurations for the rotation.

The above equations constitute the core of molecular simulations to describe so-called bonded (intra-molecular) interactions.

2.3 Electrostatics

To describe molecules on atomic level, we need to describe the effect of atomic and molecular charges to the system's behavior [102, 126-129]. In molecular dynamics we usually take into account only the repulsion and attraction by electric charges (i.e., Coulombic interaction), and ignore polarization effects that charges may induce in the molecules and atoms around them [102, 126-129]. So, we assign charges to particles only once, and assume that the charges are not strong enough to modify the polarization and partial charges of their surrounding atoms and molecules.

To be able to represent the interaction between charged particles, one needs to derive the law of Coulomb from the Maxwell's equations and force

of Lorenz, which are the basic fundamental principles of electrostatics – they are like the "Newtonian equations of electrostatics". This is done in Appendix A.

We reach the well known relation

$$\mathbf{F} = \frac{q_1 q_2}{\varepsilon_0 4\pi r^2} \frac{\mathbf{r}}{|\mathbf{r}|} \qquad \textbf{(19)}$$

which tells us the magnitude of a force between charged particles, having charges q_1 and q_2, when separated by distance $r = |\mathbf{r}|$. Here we assumed low charge density (permittivity close to permittivity of vacuum ε_0), no fast movement of charged particles, and also that all charges are constant.

This law can be straightforwardly used in MD simulations to describe the charged interactions between the particles [138]. These Coulombic interactions are one of the cases where one deals with so-called non-bonded interactions in molecular simulations.

2.4 Lennard-Jones Interactions

In addition to forces between charges, there are more subtle interactions between atoms and molecules [102, 116, 126-129]. These include i) attraction between polar molecular groups, ii) polarization effects, where one molecule can influence the charge distribution of another, resulting in weak attraction between these polarized regions, and, very close to the atom itself iii) a strong repulsion caused by overlapping electron orbitals of atoms, determining the *size* of an atom. These attractive forces, acting on a range of a few nanometers from the atom are called van der Waals interactions, and the short-range repulsive force is called the Pauli repulsion.

In molecular dynamics one does not usually describe explicitly either of these forces. Instead, one uses the so-called Lennard-Jones potential, which combines these two, having Pauli repulsion at short distances, and van der Waals interaction at longer distances from the atom center (Figure 9) [102, 126-129].

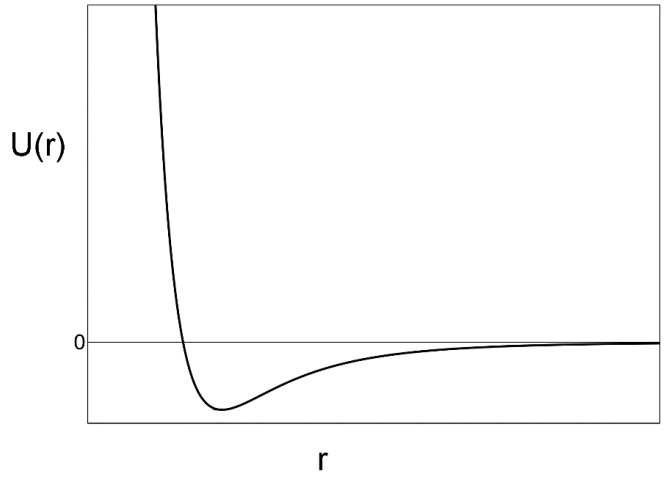

Figure 9: The Lennard-Jones (LJ) potential. r is the distance from the center of the atom, along radial coordinate. Figure modified from Wikipedia commons.

In MD simulations the Lennard-Jones potential is most commonly applied as a pairwise potential, where the shape and the strength depend on the interactions between atoms *i* and *j*:

$$U_{ij}(r) = r^{-12}C_{12,ij} - r^{-6}C_{6,ij} \quad \textbf{(20)}$$

where $C_{12,ij}$ and $C_{6,ij}$ are material-specific parameters to scale the repulsion and attraction for an atom pair *i-j*, respectively. The exponents of the potential (12 for repulsion and 6 for attraction) have been selected for convenience, to allow numerical calculations in simulations to be as quick as possible.

The potential then imposes a force between the particles *i* and *j*. The force is of course dependent on the distance between the atoms:

$$\mathbf{F}(\mathbf{r}_{ij}) = -\nabla U_{i,j} \quad \textbf{(21)}$$

If we define the direction of the force to co-incide our "**r**" axis of our coordinate system, it would look like this:

$$\mathbf{F}(\mathbf{r}_{ij}) = \left[\frac{\mathrm{d}}{\mathrm{d}r}\left(r^{-12}C_{12,ij} - r^{-6}C_{6,ij}\right)\right]\frac{\mathbf{r}}{|\mathbf{r}|} \quad \textbf{(22)}$$

Of course, in practise we operate in Cartesian coordinates, and thus have one term for each axis (*x*, *y*, *z*) in the equation.

Together with Coulombic interactions (which were described in Chapter 2.3), the Lennard-Jones potential completes the picture of the non-bonded

interactions that are highly important in molecular simulations, reproducing, e.g., thermodynamic solvation and partitioning behavior.

2.5 Statistical Mechanics

In the chapters above we glimpsed through the mechanics and electrostatics needed in MD simulation. To be able to simulate molecular scale systems, we need also methods from statistical physics – especially some statistical thermodynamics, to apply state variables like "temperature" to the molecular description. For a more thorough introduction to statistical physics descriptions of mechanics and thermodynamics, the reader is advised to take a look at the following references [139-142].

Thermodynamics describes the physics of the phenomena having to do with heat (temperature), and especially the responses of particles when they are exposed to temperature changes, i.e. cooling or heating. In a thermodynamic description the system has a "state" which has properties like "volume", "temperature" and "pressure". Forces and heating and cooling can change the energy of the system and lead to, for example, changes in the state of the matter.

Meanwhile, statistical physics leans on statistical mathematical formulae when describing phenomena, i.e. the systems investigated show some kind of probability-based behavior, which can be modeled with the tools of statistical physics. Statistical physics provides tools to quantify the stochastic nature of mechanical many-body systems (statistical mechanics). On the molecular level, statistical mechanics can be used to derive the laws of macroscopic scale thermodynamics by the means of statistical thermodynamics, which links the statistical behavior of molecular particles to the global thermodynamic variables like temperature or pressure.

In macroscopic systems one can just measure the pressure or temperature of the system, but on molecular scale those quantities cannot be measured as such. On molecular scale for example "temperature" is a statistical quantity, describing the average kinetic energy of the particles. To maintain constant temperature in simulations, one needs to have a way to calculate the temperature of the system based only on the masses and velocities of the particles. Statistical mechanics gives us tools to do just that.

In addition to temperature, also pressure is a statistical variable in molecular systems. In a closed container having liquid inside, the pressure against the walls of the container is actually caused by particles hitting the

container walls at random intervals. The distribution of the frequency particles hitting the walls is statistically distributed. The more frequently the particles hit the walls, the heavier they are, and the higher velocity they have, the higher the pressure against the container wall. Thus, the pressure in molecular simulation can be calculated by monitoring the collisions of the particles of the system, with the help of statistical methods.

Also energy itself becomes a statistical variable on molecular scale. Each molecule has its own kinetic and potential energy. The sum of all these little energies is constant, if the system is isolated from its surroundings. But each molecule can change its energy state for example by hitting other particles and like that gaining or losing some kinetic energy. The energies are thus statistically distributed in the system.

2.5.1 Setting the Kinetic Energy for the Particles in order to Start Simulations

We have now seen that system properties (temperature, energy, pressure etc.) can be calculated exactly from molecular data. On the other hand there is a vast number of ways of building a molecular system to fulfill certain macroscopic properties (like “temperature 37 degrees Celsius”). We thus need some mathematical formalism to assist us in determining which states of the system are more probable, and would thus represent the system the best. We need, for example, a way to set the molecules to their representative kinetic energy values in a way that it represents a *probable* state that the system would take in real world, too. It is namely crucial that we start our simulations from a state which the system takes very often, rather than accidentally starting it with a configuration the system visits only very rarely. We wish our results to represent the system behavior “in general”, and not its behavior in a rare event, which may happen very seldom.

2.5.2 Microstates, Phase Space, and Ensemble

Each state the system can take, when still fulfilling the conditions of, for example “constant temperature” is called a microstate. The conditions set to the system (for example “constant temperature”) is called an “ensemble”, and a single representation of this ensemble (like “temperature 37 degrees Celsius”) is called a macrostate representing that ensemble. The group of all possible states the system can take when still residing in this same macrostate is called a “phase space”.

The ensemble thus determines which quantity/quantities are held constant (energy, temperature, pressure, etc.). The macrostate determines, at which *value* the system will be kept (for example 37 degrees Celsius). The phase space tells the range of configurations the system can take within these restrictions, and the microstate is the state the system has at *one specific instant*.

In reality, as MD systems are described via classical mechanics, we of course have not discrete, but continuous distributions for particle energies and momenta, which form the degrees of freedom of the system. Each set of these, which reproduce the macrostate, is called a microstate for that ensemble. In classical systems there can thus be an infinite number of microstates. This is not a problem, however, as for surveying a molecular dynamic system, we need only two things: we need to know which kind of microstates are most probable, to set the system's starting structure to correspond to a commonly observed microstate. When running a simulation, we also need to know whether we can survey all the available states for the system freely, to not be stuck in some parts of the phase space (as not all microstates can change to some other microstates) – or if there are restrictions, we need to be aware of them.

2.5.3 Configuration

Now we will focus on the theoretical principles behind the formulae of the most probable microstate, i.e. in constructing a solution to the starting structure of the MD system.

In MD the most crucial degrees of freedom are those of kinetic energy. In many cases also the spatial configurations of molecules, and their distribution in the system are made as random as possible before starting the simulation, and special care needs to be taken that no "pre-ordered" structures are simulated un-intentionally, but the most crucial step is still to assign an appropriate distribution of velocities for the particles – to assign particles with suitable kinetic energy values. These velocities then serve as a crucial pre-requisite to reproduce the time evolution of the macrostate investigated.

There is reason to stress that finding an appropriate distribution of velocities is indeed of crucial importance. This task can be accomplished by examining the properties of the most probable state of the system (the most probable energy distribution), and linking this state to the appropriate values of temperature to find an algorithm capable of assigning a suitable velocity distribution.

In Appendixes B, C, and D, we discuss how the most probable distribution for energy levels can be derived, how entropy is defined as the thermodynamic quantity linking the temperature of the system to the energy levels of molecular states, and how – by combining these two – the Boltzmann's distribution emerges from the underlying principles of physics. These aspects are often discussed in literature, therefore we present and discuss them in the appendices only.

By setting the velocities of the molecules of the system so that the kinetic energy distribution follows the Bolzmann's distribution, one can reach a reasonably good approximation for the starting configuration of the MD system. In practice one just starts the *NVT* simulation with this setup, monitors the kinetic energy values, and if needed, corrects or scales the velocities of the molecules to reach a constant temperature and an equilibrated system during the simulation run. After equilibration the system can then be ran longer, and the gathered data can be used to investigate the biological properties of the system.

3. Implementing Mechanics and Statistical Physics into Molecular Dynamics

In the previous chapter it was described which kinds of mathematical formulations can be used in constructing a molecular system in physics description. In this chapter it is illustrated how these formulations can be transformed to computer simulation of the evolution of a molecular system in time, a molecular dynamics (MD) simulation, and how these simulations are to be ran. It is shown how time, molecules and atoms, forces between them and thermodynamical ensembles are implemented to the simulation protocols in practice. Some of the most common analysis protocols of simulation results are also presented.

3.1 Software to Implement the Ensemble

The aim of MD is to simulate molecular systems and their time evolution in a way that it describes sufficiently well the behavior of the same systems in the real world. In Chapter 2 we discussed the mathematical formalism of several of the essential features that underlie molecular dynamics simulations. Next we discuss the machinery needed to apply these ideas to practice, thereby allowing us to carry out simulations and monitor the time development of a system of interest.

While the description of interactions is the core of any simulation model, here we prefer to first discuss some practical aspects and come back to the description of interactions in Section 3.5, where we discuss related themes in greater length.

3.1.1 Describing Time in Molecular Dynamics – the Integrator

The heart of MD is the integrator. The integrator creates the time evolution to the system in the form of small and discrete time increments, Δt. The integrator takes the mathematical formulas of the mechanical forces, and applies them to the simulation system, and based on those re-calculates and re-distributes the velocities to the molecules.

The integrator's action is quite simple. First the algorithm checks the positions and velocities of the atoms and molecules. Then it calculates the forces acting on each particle at a given moment. Then the algorithm moves time by one time step Δt, and calculates a new set of coordinates and velocities based on the forces acting on the particles in the system.

There are several common integrators, which differ from each other by their complexity [102, 128-129]. The most common integrators are the Leap Frog and the velocity-Verlet algorithms [143-144].

Here, as an example of an integrator, is given the pseudocode of the Leap Frog algorithm:

$$\begin{aligned} \mathbf{r}_{n+1} &= \mathbf{r}_n + \mathbf{v}_{n+1/2}\Delta t \\ \mathbf{v}_{n+1/2} &= \mathbf{v}_{n-1/2} + \frac{\mathbf{F}_n}{m}\Delta t \end{aligned} \qquad \textbf{(23)}$$

The algorithm describes the evolution of the system from the time step n to the time step n+1, i.e., it advances the simulation by one time step Δt. In this algorithm the velocities are calculated in the middle of the time steps – half way between time steps n-1 and n, and time steps n and n+1, respectively. This is one of the examples of how the different integrators differ from one another – at which point each of the components, the velocities, the positions, and the forces acting on the particles, are calculated. Other differences include e.g. the number of terms used in the integrator to predict the next positions and velocities. The more terms are used, the more accurate is the integrator, but increasing the number of terms also decreases the integrator's computational performance.

Each integrator algorithm has its own pitfalls – some are more prone to propagate rounding errors in the calculated values, some do not produce accurate values of the velocities, and others are computationally expensive [128]. One of the requirements that is considered to be crucial in MD simulations is the integrator's ability to generate time reversible trajectories. Time reversibility (more generally symplecticity) is an

important property since it implies, e.g., conservation of energy during the time integration process.

The leap frog integrator is probably the most commonly used one, as even though it is computationally a little more expensive than some of the others, it can reproduce the velocities correctly, and is not prone to propagate rounding errors in the numerical computations [128].

3.1.2 Simulating with the Integrator

Each MD software package has the integrator as their hard coded "core" of the whole program [131-135]. It is usually just the integrator together with computations of forces, which use the most of the computational resources of the simulation. The simulation programs have highly optimized performance of their integrators, and that is the reason why each program usually provides only one, or perhaps two, different integrators to choose from. When one has selected the software one will be using, the integrator is thus already pre-determined for the user.

The only thing one needs to keep track on when running the simulations with the integrator, is the nature of one's own simulation system – as the properties of the atoms and molecules in the system should be taken into account when the time step Δt is selected in the beginning of the simulation run. The rule of thumb is to use a time step of the size of approximately 1/20 of the fastest oscillatory motion (for example bond vibration) of the system [128]. Usually the by far fastest motion is the hydrogen vibration. If hydrogen bonding is not essential for the system described, it is thus highly recommended to freeze the bond length of hydrogen atoms, or not describe them as separate atoms at all but instead describe for example the methyl group -CH3 as a single entity instead of one carbon and three hydrogens. This speeds up the simulation significantly, as the time step can be set much higher when the hydrogen vibrations need not to be taken into account [128, 138].

3.2 Thermostats and Barostats

When the integrator is solving the time evolution of the system, it produces the *NVE* ensemble, as the particle number *N* stays constant, the integrator does not modify the volume *V* of the system, and the Newton's laws maintain constant total energy *E* for the system.

However, often one wants to simulate systems in constant pressure instead of constant volume, and in constant temperature instead of constant total energy. To do that, one needs to add additional parts to the iteration protocol of the integrator. These kinds of pressure controlling algorithms are called barostats, and temperature controlling algorithms known as thermostats, respectively.

3.2.1 Thermostats

In the beginning of the simulation, the velocities of the particles are assigned with the help of the Boltzmann distribution or some other reasonably random distribution, to correspond to the temperature in which one wishes to simulate the system [102, 138]. However, maintaining this temperature during the simulation needs to be taken care of separately.

The integrator of a MD system does maintain constant total energy of the system, but not constant temperature. It re-distributes the energies straightforwardly, and does not take into account how much of the energy goes to potential energy – for example to stretching a bond far from its equilibrium position, or changing the conformation of a molecule to a higher energy conformation – and how much is distributed to the kinetic energy, for example in the form of translational motion of molecules. This leads to stochastic heating and cooling of the system.

To keep the system at constant kinetic energy, one needs to add a thermostat to the integrator, to avoid the system cooling down when some of the kinetic energy is transferred to potential energy, or to heat up when the potential energy is released again to kinetic energy.

One way to do this is to scale all velocities every now and then, to reproduce the target temperature. The so-called Berendsen thermostat is using this kind of approach [145]. The total kinetic energy of the system is calculated at frequent intervals, and the value is compared to the target temperature, the velocities of all atoms of the system are then scaled with the same scaling factor to reach the target temperature. Now the temperature converges with ease close to the target temperature, but might never reach it precisely. The other side effect of this thermostat is that it does not reproduce the canonical *NVT* ensemble, but only mimics it.

Another way of implementing a thermostat is the so-called Nosé-Hoover thermostat [146-148]. This thermostat is more complex, and is based on the so called “heat bath”. In the heat bath approach the system is linked to an additional degree of freedom, which can donate or receive heat, but does

not interact with the system otherwise. Usually this thermostat first proposed by Nosé is in practice implemented with the Hoover method, where the heat bath also has a coordinate and a momentum. These are abstract, however, so the heat bath does not really move away from the system it is thermostating.

This formulation can reproduce the canonical ensemble, but is at its best when the temperature of the system is already rather close to the target temperature. If that is not the case, the Nosé-Hoover thermostat tends to undulate wildly around the target temperature [138]. This can cause the simulation to crash due to unstable conditions, or to just lead to production of large amounts of useless data, because a simulation with fluctuating temperature cannot be used quite so well in the analysis of the system properties.

Due to this, the standard protocol to simulate systems in constant temperature has for a long time been to start the simulation with the Berendsen thermostat, which quickly sets the temperature of the system close to the target temperature, and then to continue the simulation with the Nosé-Hoover thermostat, which produces the canonical ensemble and also converges fast to the exact target temperature [138].

However, now as the developers of the GROMACS software package have implemented a newly published, potent, thermostat called V-rescale, that is about to change [149]. The V-rescale thermostat is basically a Berendsen thermostat with an additional stochastic term. Thus, not all velocities are scaled with the same scaling factor, but a stochastic term is added, which gives rise to statistically distributed values for the velocity changes. This modification enables the system to reach the true *NVT* ensemble, and also converges fast to the target temperature. In addition to that, running the temperature scaling in GROMACS with V-rescale, instead of Nosé-Hoover, is actually even slightly faster in terms of processor time.

3.2.2 Barostats

With the integrator and the thermostat one can simulate the canonical ensemble, which corresponds to a closed container, at a constant temperature. To simulate an open container instead – for example at room temperature, and normal 1 atm pressure – we need to add a barostat, a pressure controlling algorithm, to the simulation protocol.

The function of barostats is based on scaling the size of the simulation system, the distances between single molecules, and the equations of motion of the molecules in the simulation system.

The most common barostats used in MD simulations are the Berendsen and Parrinello-Rahman barostats [145, 150-151].

In the Berendsen barostat all the molecular coordinates are scaled such that the system stays in the desired pressure [145]. This is done by changing the simulation system size by a scaling factor and adding a corresponding change to the velocities of each molecule. If the box is made bigger, the molecules are allowed higher velocity, and vice versa. The scaling of the system size is done slowly, in the course of very many time steps, and the compression happens inside the limits of the isothermal compressibility of the molecules in question, which is given as a parameter to the simulation program, to not break down the simulation system. However, usually setting the time interval (the time step) for the barostat action wisely, already eliminates the possibility of compressing or expanding the system too vigorously.

The Parrinello-Rahman barostat does not just scale the system properties, but adds a "piston-like" element to the system description [150-151]. The "piston" has a mass, an equation of motion, and it acts on the system volume. The piston will push/expand the system with some velocity depending on the system properties, i.e. based on the kinetic and potential energy the molecules of the system have. If the system is "hard to push" the piston proceeds more slowly, mimicking a real situation when compressing or expanding a substance. Further, the Parrinello-Rahman method also takes into account the isothermal compressibility of the molecules, and the "piston" never moves faster than the molecules can bear.

Both Berendsen and Parrinello-Rahman barostats can be used as both isotropic and an-isotropic barostats. An isotropic barostat scales the system size the same amount on each side of the rectangular simulation box, but an anisotropic barostat can change the system shape, and even keep one or two of the three dimensions unchanged during compression. This is very practical when simulating systems consisting of many different phases – for example when simulating a lipid layer between air and water. If one would need to scale all dimensions with the same pressure, the air phase would vanish from the system, but with semi-isotropic pressure coupling, where one compresses one of the three dimensions differently than the other two, one can generate rather hard pressures into the water and lipid phases and yet preserve the air phase of the system intact.

Also some conformational changes, for example crystallization or melting of large molecules, need so much space to happen that it is convenient to have "flexible walls" of the simulation system, each of which are able to give space to the big molecules rumbling around in the system. Now the system

could be simulated with a totally anisotropic barostat, where each of the three dimensions can change its pressure unrelated to the other two. Each of these three flexible walls can adapt to the movements of the molecules on its own speed, without all walls needing to move with the same pace.

However, getting back to the barostat implementation, and comparing the Berendsen and Parrinello-Rahman barostats: the Berendsen barostat can reach constant pressure for the system very quickly, but Parrinello-Rahman is considered better for long simulation runs. The reason for that is that it is not a trivial task to combine an integrator with both thermostat and barostat, and one should combine them in a way, which interferes the time evolution of the system as little as possible. As the Berendsen barostat and the Berendsen thermostat fit well together, but cannot quite reproduce the isobaric-isothermic *NpT* ensemble, this combination is suitable for only approximate runs, or in situations where only the average properties, and not the fluctuation properties of the system are of interest.

Simulations are usually started with the Berendsen barostat, and after the pressure has stabilized close to the reference pressure, the simulation is continued with combining the Nosé-Hoover thermostat with the Parrinello-Rahman barostat. This combination provides a more realistic representation of the system, but can cause large oscillations in both temperature and pressure, if used when system properties are not yet close to their reference values [138].

In any case, adding both a thermostat and a barostat to the integrator makes the integrator code sometimes very complicated, and it is tricky to ensure that the right ensemble is produced and that the simulation stays stable at the same time. To generate smooth constant pressure simulations, the standard protocol is to simulate the system first with only temperature coupling, with the Berendsen thermostat, and then add the Berendsen barostat on the side, and finally for the production run change both barostat and thermostat for the Nosé-Hoover – Parrinello-Rahman combination.

3.3 Simulating Molecules

We have now seen how the thermodynamic ensembles can be reproduced in simulations as additions to the integrator. However, even assigning the new velocities to the atoms in the integrator is not a straightforward process. Often a completed integrator step leads to violations of bond lengths or angle bending, or brings molecules too close to each other. All this imposes large forces to the atoms and molecules of the system, but the MD algorithm is usually capable of dealing with these forces. And if not – the system crashes, and the simulation needs to be restarted.

All simulations can crash due to excessive forces, but the probability of such an event can be lowered by a pre-minimized starting configuration, to get reasonably close to energy minimum configurations for all molecules of the system, before starting the simulation run. Sometimes that is not enough, however. It is sometimes a good idea to use bond and angle constraints to calm the system down before releasing all restraints and starting an unconstrained simulation run [138]. Constraints can be needed in the beginning of the simulation also for simply speeding up the system – for example constraining all bonds of hydrogen atoms speeds up simulations significantly, as mentioned already in the previous Section [128, 138].

Thus, to keep the simulations stable and fast, we need two new algorithms. One to energy minimize the starting structure to be able to start the simulation from as stable conformation as possible, and another to implement the constraints to the system during the integrator protocol, to speed up the simulations and prevent systems from crashing.

3.3.1 Steepest Descent Algorithm for Setting up the Starting Configuration

For minimizing the system configuration and molecular configurations before the simulation run, one can use specific algorithms, which simply calculate all the forces that the bonds, angles, rotation barriers and molecule-molecule contacts cause to the system. The algorithm relaxes the system by moving the atoms step by step towards the steepest crescent of their potential energy, hopefully finally reaching a configuration near the global configuration minimum for the whole system. This is for example how the STEEP algorithm implemented in GROMACS works [138].

As a result of the energy minimization process, the molecules can of course get stuck in a local minimum. If that happens, one can reconstruct the structure to be minimized to avoid that, and run the algorithm again and hope for better outcome. Another option is to use some more elaborate configuration minimization protocols, such as simulated annealing [127-128]. In simulated annealing the system is heated to a high temperature to allow considerable conformational freedom, and then slowly cooled down afterwards. Doing this provides a better chance that no molecules get stuck to the local minima in the conformational space. When using this kind of approach one needs to be careful, though, as some molecular isomerizations not possible in room temperature can take place in the high temperature phase of the simulated annealing protocol. One thus needs to protect the stereochemistry of the molecules by for example adding angle constraints to the system when running the annealing.

3.3.2 Implementing Holonomic Constraints for Molecules

In cases where there are bond or angle constraints in the MD system, one needs a way to set the constrained bonds and angles back to their equilibrium values, after the MD integrator has updated the positions of the atoms in the simulation system, possibly violating these constraints. Specific algorithms have been developed for this.

In GROMACS there are three different algorithms – the SHAKE, SETTLE and LINCS algorithms [152-155].

SHAKE is an iterative protocol, which solves equations of motion in the Lagrangian formalism, taking into account the holonomic constraints in the molecules (the constrained bonds and angles). The protocol is iterative, and stops only when a satisfactory solution for all atoms has been found, or a pre-set maximum number of iterations is reached [152].

Another possibility to set the constrained bonds and angles back to their right values is an algorithm called LINCS (LINear Constraint Solver) [154-155]. LINCS does not use iterations, but rather stores all the force gradients the constraints impose to the system in a single matrix, and moves all the atoms towards the gradient of the matrix in one step. In most cases the procedure leads to satisfactory results such that no iterations are needed. But if one wishes, one can also do up to four iterations of LINCS, to make it absolutely sure that the constraints are well taken care of. To speed up simulations even more, many software packages also provide a fast constraint solver for water molecules only. Very often most of the simulation box is full of water, and most of the simulation resources are

used to simulate water molecules. To accelerate the simulation up, one often imposes bond and angle constraints for the water molecules to reduce the time one spends simulating ”only water”. To get full advantage of this, for example the GROMACS software provides a fast and efficient version of SHAKE to take care of the iterative solving of constraints of water molecules. That program is called SETTLE, and it indeed speeds up the simulation significantly [153].

3.4 Tricks for Faster and More Accurate Simulations

3.4.1 Simulation Box and Boundary Conditions

In MD simulations one uses a lot of processor power to calculate properties of single atoms and molecules. Increasing the number of molecules in the system increases also the computational cost of the simulation. In principle, one is restricted to simulate very small systems – only a couple of dozen nanometers a side. However, there is one clever way of setting the size of the simulation system to “infinity”. The solution is to use “periodic boundary conditions” [102,128], and it takes advantage of the fact that in simulations, the system does not need to follow the same rules as everyday life does.

If we are simulating a box of molecules, the periodic boundary means that the edge of the boundary is not a wall, but a penetrable boundary. By crossing the box boundary, and exiting the box, the molecule simultaneously enters the box from the opposite side (Figure 10). If the molecule exits the box from the right hand side, it at the same time enters the same box from the left hand side. We simply just set the “neighboring spot” of the right boundary to be the left hand boundary. Now the molecules can move freely in a virtually infinite box.

We can also plot this as an infinite number of similar boxes (Figure 10). We simulate only one of them, but actually describe in the simulation an endless number of exactly similar simulation boxes. This periodicity causes of course various kinds of artifacts to the system. For example membrane undulation modes, which may happen to have as their periodicity a fraction multiplier of the simulation box length, may be pronounced in the results,

and undulation modes having a wavelength longer than the box size will not be seen in the results at all [49, 118]. Also, very big molecules can see themselves through the box boundary, and even small molecules can "sense" the periodicity. This can be problematic, as the molecules might organize themselves to abnormal conformations, or too ordered structures due to periodicity effects [158-159].

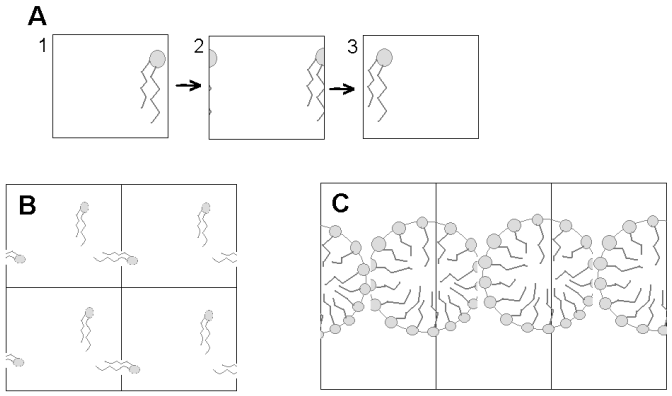

Figure 10. The periodic boundary conditions. A) If a molecule crosses the box's periodic boundary on the right, it re-enters the box on the left. B) The periodic boundary conditions can be described as an infinite number of similar boxes. C) Micelle fusing to itself across the periodic boundary.

However, the periodic image can be used as an advantage, too. For example, investigating vesicle fusion across the periodic boundary is a clever idea – one can simulate only one vesicle, and save a lot of computational power by doing that, but still see two different vesicles fusing, as the vesicle is fusing with itself over the periodic boundary (Figure 10) [160]. This trick may of course change the qualitative nature of the fusion process, and before applying such tricks, one should carefully test how much the protocol will tweak the behavior of the system in question.

Other types of boundary conditions include various types of solid walls, and external potentials mimicking free solvent properties (for example immersion to water) [102]. The periodic boundary conditions are however by far the most common choice, and usually the only boundary provided by biomolecular simulation packages, thanks to its ability to create infinite systems with only minute computational cost.

3.4.2 Treating Long-range Interactions

In a MD system each particle has two long-range, centrosymmetric potential functions – the electrostatic, and the Lennard-Jones potential. Each of these is applied as pairwise interaction functions in MD systems, as described above in Chapter 2.

Calculating pairwise forces for each atom pair in the whole simulation system is a tedious job, so several tricks have been developed to make this less resource consuming.

Neighbor lists

The most important of the ways to cut the cost of computing long-range interactions is probably the so-called “neighbor lists” [138]. For each particle in the simulation box, the software keeps track of its closest neighboring particles. The neighboring particles are collected to a so-called neighbor list, which is updated every now and then, usually every tenth time step, or so. The pairwise potentials are then calculated only between the neighboring particles, and most of the potential interaction pairs are just neglected. Here we see that it is of crucial importance to update the neighbor lists often enough to prevent molecules to diffuse close to new neighbors undetected. Also one needs to take care that the radius inside which the atoms are counted as ”neighbors” of another atom is large enough, to not leave a significant portion of the interaction range out of the description.

Restricting the potentials to a limited area of simulation space

Another way to cut down the costs of the centrosymmetric potential functions is to shift the tail of the potential slowly to zero at some radius from the potential center, or just truncate the potential at that point [138]. The Lennard-Jones potential fades away rather quickly, and there is usually no major harm done by just cutting the tail of the potential to zero at certain radius from the center of the atom. But for the charges it is a quite different story.

The Coulombic interaction has in principle an infinite range, and this can lead to significant problems in a system with periodic boundary conditions. As the molecules can see the other molecules “all the way to infinity” – there would be an infinite number of Coulombic interactions to compute, and the system would be simply impossible to simulate. Usually, to avoid this, the charges are slowly scaled to zero around a distance, which is

considered their “average range of visibility” in the biological media [138]. Charges can be efficiently shielded by other charged or electron-dense particles, so their range of effect is not after all infinite.

Cutting the tail of the charged interaction can lead to significant artifacts, however. As the charges of the same sign repel each other, the particles having a charge of the same sign tend to place themselves at equal distances from each other in the simulation systems [161-164]. This distance is just slightly larger than the cut-off length of the charged interaction. In that kind of situations one can clearly see that the cut-off clearly causes a serious artifact to the system behavior. This is especially true for systems containing a lot of ions, or strongly charged small molecules. For big molecules, and for only slightly charged, or only polar molecules the effect is much smaller, and cut-offs can be usually used without major artifacts.

When the charged interaction needs to be calculated more exactly, for example when there indeed will be a lot of ionic small molecules in the simulation system, one can use the so-called particle mesh Ewald (PME) method [165-166], which can calculate efficiently the tedious long-range Coulombic interactions by using a method based on Fourier transforms.

In any case one should always ensure that the simulation system is electrically neutral when starting the simulation. If there are negatively charged molecules, like DNA strands, one needs to add the corresponding amount of positive ions to the simulation, too, as otherwise the net charge will multiply to an “infinite negative/positive charge” in the system due the periodic boundary effect.

3.4.3 Parallelization

When running MD simulations, one is usually in a need of a lot of computing power. Usually the simulations are parallelized to 8-128 CPUs, but when using graphical CPUs (GPUs), one can survive with a smaller number of processors [167-168].

The development of computers, processors, MD software, and parameterization has worked hand in hand so that today it is possible to routinely simulate atomistic systems comprised of about 100,000 – 500,000 atoms for several microseconds, and coarse-grained systems (where multiple atoms are described with one particle) of around 100,000 – 500,000 particles for tens of microseconds to several milliseconds [169-170]. The limits of coarse-grained models largely depend on the level of coarse-graining done, and those cases will be discussed below a bit more (see Chapter 3.6). The progress has been rapid, since still seven years ago

all-atom systems could be simulated only for a couple of dozen nanoseconds, and the maturity of the molecular coarse-grained models was not yet significant [171].

Currently a typical MD simulation takes a couple of weeks, instead of a couple of months or half a year that the standard was still some five years ago. The reason for this is not only the development of faster processors, but also the better implementation of parallelization schemes to MD software engines [172]. For example, GROMACS 3, which was used until the year 2008, parallelized well only up to 8 processors. Some used it with 16 processors already then, though. But, when GROMACS 4 was released, one could suddenly parallelize systems to over 200 processors [131-132, 173].

To be able to run systems in parallel, one needs to modify the program code to be able to cope with parallel execution. One needs to also ensure that all processors have an equal amount of work to do – usually the first approximation is to give each processor the same amount of atoms to take care of, but to adjust that during the execution of the program to fine tune the performance. As all atoms do not reside in one processor any more, one needs to communicate atom positions, velocities and forces from one processor to another, if needed. Also one needs to ensure that no processor needs to sit and wait for information from other processors too long. All processors should have full work load at all times, and still efficiently communicate and transfer data between processors.

A rule of thumb is to share the similar kind of work to a certain set of processors, and another kind of work to another set of processors, provided that these tasks need a lot of communication only inside one group of processors, and not between the groups. Now the “unison” of the processors is ensured in two steps – first all processors in one group are tuned to work at equal pace, and then the processor groups are also tuned to work at equal pace.

A good example of this is the way how the GROMACS program divides the computing of a MD simulation – the heavy computing of PME electrostatics is assigned to a different set of processors than the rest of the simulation [131-132, 138]. The rest of the simulation is then divided to other processors so that each processor receives approximately the same volume of the simulation box to take care of. One set of processors thus does the tedious Coulomb force calculations, and the rest of the processors take care of the other MD routines. The MD routine processors each have a destined volume of the simulation box to take care of, and they communicate mainly with each other by transferring interactions and neighboring atoms. These

MD nodes only ask for the Coulombic forces from the PME nodes once in a time step, and they do it in a well-organized concerted manner. Like this both sets of processors get the most done in the time they have. Of course one needs to optimize manually this kind of setup – so users are advised to run test simulations with several ratios of PME/MD processors, to optimize the protocol for their individual system.

Dynamic load balancing

Good parallelization leads to an equal load for each processor. A good example of such a parallelization scheme is the way how the GROMACS 4 software deals with "dynamic load balancing", i.e. how the program divides the atoms to the processors evenly even though the simulation run itself will cause fluctuations and changes in the density and distribution of the particles [131-132,138].

In the beginning of the simulation each MD processor receives a volume slice of the whole box to take care of. Then, during the simulation the dynamic load balancing algorithm keeps track of the work load of the processors, and every now and then adjusts the box sizes again to better take the simulation system into account dynamically as the simulation progresses. Within this scheme the molecules can be easily moved from one processor to another to equalize the load between the processors.

That is very handy for example in cases of phase separation or big structural changes in the system, which change the load balance a lot during the simulation. Also it is crucial for systems having very inhomogenous structures from the very beginning on. These kinds of systems have for example large molecules on one side, and water molecules, or even vacuum on the other side of the system. Most biological systems are like this – lipid bilayers in water, proteins in water, and lipids between air and water, are all very inhomogenous systems. It is hard to approximate the relative workload for each part of the system before starting the system, but the dynamic load balancing algorithm can adjust the performance to the system properties on the fly.

Rate limiting steps – processor efficiency, and memory usage

A typical simulation run is heavily parallelized. If PME is used for calculating the Coulomb inteactions, some 30% of the processors need to be allocated only for PME. The second heaviest computing task in MD simulation is calculating the rest of the forces in the system, which typically takes at least 20% of the remaining processor power [138].

However, at present processors are developing faster very quickly, but the internal memory of the processors, and the fast memory available by the processors is getting increasingly smaller. Thus the rate limiting step of the simulations is nowadays often (instead of the computing) the waiting time needed to load the information for the computations from the memory to the processors, and especially writing output files, like coordinates and velocities for the user – generating the data files necessary for the analysis of the simulation [138]. Also communicating the atoms between processors, when running heavily parallelized systems is rather slow, even though it helps a lot that most processors have multiple cores which can communicate information fast to each others [138].

3.5 Parameterization of Force Fields, Emphasis Being on Atomistic Descriptions

3.5.1 What is a Force Field?

Classical MD systems aim for a realistic description of the molecules under investigation, but are not *ab initio* systems, where every property of the system can be deducted from the underlying theory. Thus, one needs to carefully tune the interactions that are used to describe a given system.

First one needs to decide which kind of interactions should be included in a model to have a sufficiently realistic description, and then decide the exact mathematical formulations via which these interactions are represented in the simulation model. When all the pieces are combined together, the resulting description is called a “force field” [174-177]. In physics, one also often talks about the Hamiltonian.

The force field thus includes the information that is used to describe any of the interactions in a system.

We went through some of the related descriptions of these molecular forces and interactions in the earlier Sections, and ended up having a lot of formulas containing atom-specific interactions, and interaction-specific constraints, like the bond strength between atoms A and B. Let us here summarize the most relevant interactions (Figure 11).

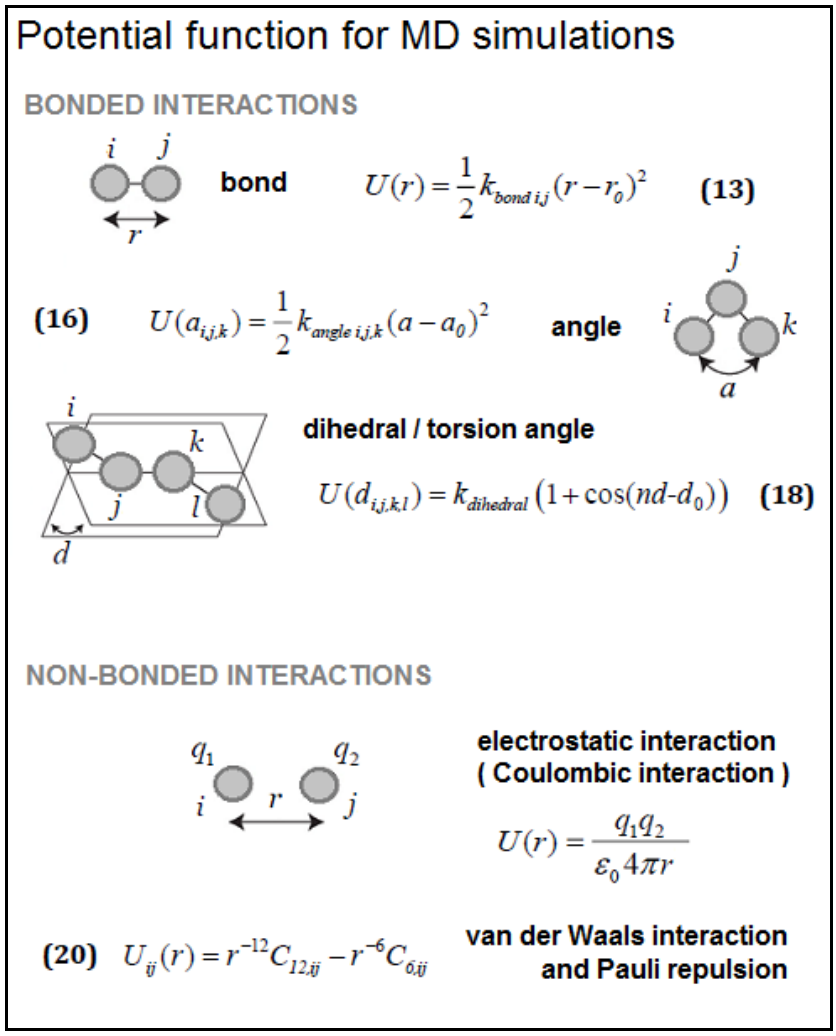

Figure 11. Example of how the potential function terms can be represented in a force field (bond, angle, torsion angle, Coulomb, van der Waals, and Pauli repulsion). Numbers in brackets refer to equation numbers in the Thesis. *i, j, k, l* are the interacting atoms. Bonded interactions: *r* is bond length, r_o its equilibrium value, *a* is angle with a_o representing its equilibrium value, *d* is torsion angle, d_o sets the first maximum of the rotation potential, n represents the number of minima in the potential. Symbols *k* are force constants. Non-bonded interactions: q_1 and q_2 denote charges of atoms, which are not covalently bonded, and ε_o is dielectric constant. *r* is distance between a pair of interacting atoms, and C_{12} and C_6 are constants which depend on the chemical nature of interacting atoms.

First, one talks about bonded interactions. These include interactions between particles that are covalently bonded to one another (bonding between two atoms, bending between three atoms, and dihedral interactions in a 4-body case being the most common ones). Second, there are non-bonded interactions, which typically are comprised of electrostatic interactions (between charges) and van der Waals (dispersion) interactions

(described in terms of the law of Coulomb, and the Lennard-Jones potential, respectively). Third, the constraints discussed earlier are also part of the force field, as are also possible truncation distances used in some interactions. It is also justified to think that any practical choice in simulating the system, such as how often neighbor lists are updated, or how the computations in the particle mesh Ewald algorithm are divided between the real space and the reciprocal space parts, are part of the force field since they affect the computations of forces in the system. For biomolecular systems, there are many commonly used force fields available (such as CHARMM, OPLS, Amber, Gromos, etc., see Table 1). It depends on the force field, and its original purpose, what kinds of atoms one can find readily parameterized [178-189]. Very often there are "standard" parameters available for all first and second row, and some third row elements of the periodic table. The most common bonding variations for each element are also present, as in many cases the bond order changes the

Table 1. Widely used force fields for biomolecules.

CHARMM [178-180] All atom / United atom	*Parameters available for :* Proteins, DNA, RNA, lipids, sugars, drug molecules *Typical simulation system :* Protein in water, study of ligand binding
AMBER [181-182] All atom / United atom	*Parameters available for :* Proteins, DNA, RNA, short hydrocarbons, drug molecules *Typical simulation system :* Protein in water, study of ligand binding
GROMOS [185-187] United atom	*Parameters available for :* Proteins, DNA, RNA, lipids, sugars *Typical simulation system :* Protein in water, study of ligand binding
OPLS [183-184] All atom / United atom	*Parameters available for :* Proteins, DNA, RNA, short hydrocarbons, drug molecules *Typical simulation system :* Drug solvation, drug conformation, ligand binding
MARTINI [188] Coarse grained	*Parameters available for :* Proteins, DNA, RNA, lipids, sugars, drug molecules *Typical simulation system :* Membrane penetration of drugs, lipid self-assembly
Berger [189] United atom	*Parameters available for :* Lipids *Typical simulation system :* Lipid bilayer in water (to assist force fields which have no lipids of their own)

properties of the atom significantly. For example, oxygen with coordination number 2 (having bonds with 2 other atoms) usually has some standard parameters, which differ from parameters of oxygen having coordination number 1 (binding to only one atom). The force field can also contain some special cases of these – for example the -OH bond in alcohols is usually defined separately, as it differs from most 1-coordinated oxygen bonds, and is also fairly common and very important biologically.

When parameterizing a certain atom, one also needs to take into account in which environment it will lie in the simulation model. There can be differences in for example rotation barriers depending on the surroundings of the atom in the molecule. One needs to keep in mind that all parameters are approximate, and very often one needs to re-parameterize atoms if one wishes to reproduce more exact behavior of the molecule of interest.

In practice, when force fields are used in simulations, the simulation code is presented with a force field parameter file listing the different atom types, and for each atom type their respective bond lengths with other atom types, and the corresponding bond angles and rotation barriers. Also the partial charge, and the Lennard-Jones potential are determined for each atom, and atom pair, respectively. Obviously, different force fields have different formulas for some of the interactions [174-177]. Especially wide variation is in the way of expressing bond rotation barriers.

3.5.2 Target Properties and Constructing a Force Field

If we are to build a general force field – a force field containing enough data to build many different systems, and into which it would be straightforward to add more atom descriptions – we need a systematic way of reaching the force field parameter values. An important part of this process is to determine, which are the “target properties” of the force field, i.e. the most important properties to be reproduced by the model.

Most biological force fields aim to reproduce system properties near room temperature, in 1 atm pressure [178-189]. For most biological molecules this means liquid state, and subsequently the target properties of choice are usually molecular density, heat of vaporization, and hydration energy (and other solvation (free) energies). These properties can be calculated from simulation results, and they offer a straightforward comparison to experimental results.

For all molecules the conformational energy is also an important property to optimize [178-189]. The configuration space is especially important for molecules such as drugs, for which usually solvated and not that much the

aggregated state in the system is of interest. The molecular configurations also naturally affect the binding of drugs to enzymes' active sites, for example. The conformations the molecules take in liquid state cannot be reached precisely via experiments, however. The optimization of the configuration space is thus done with the help of quantum-mechanical calculations for energies of different molecular configurations.

Selecting the target properties determines what kind of analysis results will be most exact when the simulation data based on using these parameters in MD simulations is being analyzed. If the target property is "solubility" instead of "molecular volume", one can investigate the phase separation processes more accurately than the density of the system.

3.5.3 Developing the Parameters

Finding the force field parameters that reproduce the target properties is a tedious and time-consuming iterative (systematic) process. One needs to set the parameters to be tested, simulate the system, calculate the target properties, re-adjust the parameters based on the results, and repeat this cycle until all target properties are sufficiently close to their experimental and quantum-mechanical simulation values. Finding a perfect match between simulations and experiments for a variety of system properties is hardly ever met, especially if the force field is to describe a wide variety of molecules with the same parameters. This leads to the obvious conclusion that no force field can model all system properties exactly, and one is to always remember this when interpreting the simulation results.

3.5.4 Constructing New Molecules for an Existing Force Field

There are many force fields one can use, already built and ready for action [178-189]. The development of a couple of them is even the basis for the Nobel prize in Chemistry 2013 [180].

However, often one faces a situation where one has a nice general-purpose force field one wishes to use. It has the right target properties, and it works well in the temperature and molecular phase range one wishes to reproduce, but no one has used it for the molecule one is interested in.

When constructing a new molecule for a certain force field, one needs to go through the existing parameters listed in the force field and try to find all interactions that are relevant in one's own molecule. If the parameters for all interactions are not there, one needs to consider if one can approximate

them with the existing parameters for closely related atoms, or is it essential to generate new parameters for the molecule one aims to explore. When adding new molecules to the force field, one has to always recalculate the partial charges for the atoms with QM (quantum mechanical) methods, but most other parameters can often be taken from an existing force field. After parameterization the properties of the molecule are tested, and for example the conformational space is monitored – and if the molecule is seen to lie in abnormal configurations, the rotation barriers of dihedral angles (and sometimes bond angles, too) are then modified to aim for a better model.

When more extensive parameterization of the new molecule is needed, one typically targets for the same properties as the people who originally developed the same force field also targeted when they constructed it in the first place. So, if the force field was constructed to reproduce the solubility properties, the new molecule is to be tested in simulations of different solvents. The simulation results need to reach reasonable agreement with the experimental data and QM results of the target properties, before the parameterization of the newly created molecule can be used in simulations.

Sometimes one needs to modify even the target properties to make the force field more suitable for different kinds of systems. For example, the OPLS force field is targeted for small molecules in liquid state, and that causes solidification of larger molecules already in room temperature [183-184]. However, as the force field contains an extensive number of parameters for many different functional groups – being thus very practical in building drug molecule structures – there would be an interest to use it in lipid bilayer simulations. To use OPLS to simulate lipid molecules, the Lennard-Jones parameters and rotation barriers of the carbohydrate tails of lipids need to be re-adjusted to reproduce the delicate liquid crystalline state of lipid molecules, and the various phase transitions the lipid tails show near room temperature. There have been various attempts to make this happen, and at this moment many laboratories use home-made modifications to describe the lipid tails in OPLS, to be able to enjoy the wide range of available molecular structures available in the OPLS force field, and still be able to reproduce the liquid state of the lipid systems [190-191].

3.6 Coarse Graining

In many force fields, for example in the OPLS-AA force field, each atom has its own particle [184]. These, so called ”all-atom” force fields are rather

precise and can, for example, show pretty exactly the hydrogen bonding patterns, and drug binding configurations for an enzyme.

However, if one is less interested in the details but aims for a more generic picture in a larger scale, thereby better understanding soft matter properties in general – for example self-assembly or diffusion of particles, or elastic properties like bending and other deformations of surfaces – it is not always necessary to describe every atom with a single particle. Many biomolecules can be rather straightforwardly described with a smaller number of particles, reaching a so-called coarse-grained model, where multiple atoms are represented with one particle only.

Coarse graining is a convenient way to gain access to phenomena on larger scales – one can run bigger systems showing phenomena like self-assembly of micelles and other lipid phases, drug penetration to membranes, and even peptide and protein folding [193-195].

There are many different levels of coarse graining. For instance, to speed up the computational performance of atomistic systems, one can describe the non-hydrogen bonding hydrogens (for example in hydrocarbon chains of lipid tails) as a united entity with the adjacent carbon atom. This kind of force field, where most hydrogen atoms are combined to their adjacent carbons to aim for -CH- , -CH2- and -CH3 entities, is called a united atom force field [183].

Moving on, one can take 3-4 atoms or atomistic groups to form a new unit, so called "bead", like in the MARTINI force field (Figure 12) [188], or one can take only 3 beads to describe the whole lipid molecule as in many parameterizations used in dissipative particle dynamics (DPD) simulations (see for example [192]). Here the same applies as for all atom force fields – first it takes a lot of time and effort to construct the parameters for the force field. After that using the existing general-purpose force field to describe new molecules is a simpler task, and needs only small modifications to the already existing parameters. The MARTINI force field is tuned for the most common biological molecules (lipids, carbohydrates, DNA, and proteins) [188], and all the target properties – in the case of MARTINI especially the phase behavior and solubility (partitioning) properties in room temperature – will be inherited to the new particles automatically. Phase behavior in MARTINI is mostly dominated by the LJ parameters and repulsion/attraction interactions (which are the way MARTINI implements the charged interactions instead of Coulomb potential). In very many cases one can construct the desired new molecule just by adding the existing building blocks together, and no new parameterization is needed. And even when new parameters are needed, one can mostly concentrate on the

reproduction of the configuration space (by complementing the MARTINI description with the needed amount of bonded interactions) [188]. One can thus rely on the force field in many issues, and needs to re-adjust the parameters only for the very details.

The speed up of coarse-grained models compared to atomistic simulations depends on the level of coarse graining. The united atom models are not significantly faster compared to all atom models. Meanwhile, the speed up of MARTINI models is usually about 1000x compared to corresponding atomistic descriptions. Finally, if one goes to very simplified models such as two-dimensional molecules (limiting the investigation to only, e.g. to the plane of a lipid membrane), describing each molecule with only one particle (simply using larger particles for larger molecules), and describing the solvent as a "potential field" instead of explicit particles, then the speed up could be very large indeed.

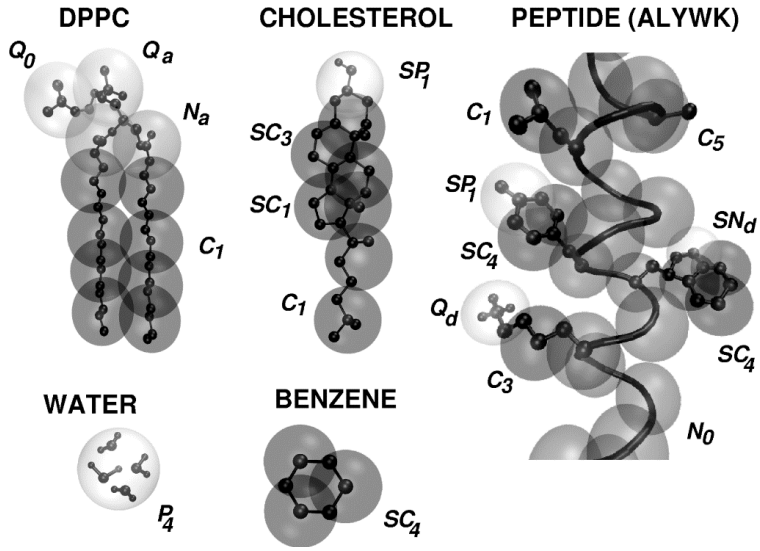

Figure 12. MARTINI-based mapping of particles. As the examples here highlight, in MARTINI one usually maps about 4 atoms or atom groups to a single coarse-grained bead. The symbols in the picture (P4 etc.) describe the bead types assigned to the corresponding parts of the molecule [188]. Figure adapted from the MARTINI website, with the permission of original authors.

There are several pitfalls in this approach, however. Describing multiple atoms with one particle sometimes changes the spatial relations of the molecules, modifying for example the diffusion properties and density of the system unexpectedly [188, 196]. Also some structures, such as the benzene ring are very difficult to coarse grain. In the case of benzene, and other planar structures, one usually needs to add extra constraints to the system to keep the desired ring planar during the simulation [138].

Another very difficult structure for coarse graining is the peptide backbone of proteins. Protein folding is primarily a hydrogen bonding process, and the energy differences between alpha helices and beta sheets are so small that even minute changes in the parameters bias the coarse-grained simulation results [197-198]. There has been at least one promising solution to this problem [199], but at least the MARTINI force field is so far able to simulate proteins only with fixed secondary structure [188].

3.7 Reaching Equilibrium Properties for the Simulated System in a Given Ensemble

3.7.1 Scanning the Phase Space

In MD simulation, one wishes to scan the phase space (the configuration space available for the system) as thoroughly as possible. One wants to visit every part of the phase space, and spend the most time in the most accessible areas of it. So, the aim is to have molecules near their energy minimum structures, and only rarely allow them to do things, which are energetically costly.

In Monte Carlo simulations this is done by setting a "penalty function" when one wishes to change molecule conformation from one conformation to another [129]. If the new conformation is energetically more favorable, it is chosen with a higher probability than when it is energetically costly.

In MD we do not need to worry about this that much. We of course wish to survey the phase space thoroughly both in energy space and in conformation space, but the mechanics and thermodynamics we include to the model keep the system and its parts automatically close to the energy minimum configurations. We thus will for sure scan mostly the rather favorable configurations and motion patterns of the molecules. And, as we have also included temperature into the description, the molecules will have enough energy to sometimes cross energetically unfavorable barriers, too. Depending on the barrier height, of course.

If we set the starting configuration to be as random as possible (random positions and orientations of molecules), we can be rather sure that the system will scan the phase space around the true minima of the system. However, it is very easy to accidentally construct somewhat ordered

starting configurations for the system, or get stuck to high energy conformations, or local minima, which do not represent the global, or the most common, minima of the system and the molecules. When this happens, the model cannot be equilibrated by just running it for elongated periods of time but the artifact needs to be fixed manually by altering the starting configuration to better resemble the configuration space one expects the molecules and the system to take.

However, in any case, to ensure that the simulation is indeed ran in an appropriate configuration space, one should carefully monitor the simulation results, especially if the molecules used in the simulation are not widely tested in simulations, or when testing a newly parameterized molecule. Careful observation of the phase space is also needed when the molecules of interest are used in a different context than the one for which they were parameterized.

For standard systems (such as lipid bilayers), and widely tested molecules (like most phospholipids), the standard simulation protocol is usually enough to prevent hard-to-spot configuration space anomalies from happening – it is enough to start the simulation with random configurations, run the steepest descent (or other energy mimimizing) algorithm for the system to get rid of configurations not normally present in the system of interest, and after that equilibrate the system in the preferred ensemble. A rule of thumb here is that "random configurations of molecules" should be interpreted to go only for the configurations accessible for the molecules of interest in the temperature of interest. If one wishes to simulate lipids in their (all) *trans*-configuration, and the simulation temperature does not allow transition between *cis* and *trans* states, one should not construct a starting population having both *cis* and *trans* states, but instead set all molecules to the *trans* configuration, and randomize only those configurations which are truly accessible for the molecules also in the simulation temperature. While equilibrating, one should monitor the energy terms of the system – the potential and kinetic energy levels and their fluctuation, along with visual inspection of the simulation trajectory. It is usually very easy to spot configuration space derived abnormalities in the system – part of the system may go to ordered phase unexpectedly, or demonstrate other concerted phenomena. If this happens, the simulation has to be started again – with a new and more appropriate set of molecular starting configurations.

More subtle artifacts generated as a result of a non-representative starting structure ensemble (which may not be fully resolved during the steepest descent step) need more detailed inspection to be spotted – for example a small fraction of the molecules of the system may be in a configuration

which is very rare – or even un-accessible – in that part of the configuration energy diagram which corresponds to the simulation temperature. This results from randomizing over angles and dihedrals that are not truly free variables in the simulation system – and if the molecule is not very well known (from experiments, quantum mechanical studies, or earlier molecular dynamics simulations), these kinds of events may very well take place. Thus, when parameterizing and testing new molecules, the simulation results should be analyzed for all key angles, dihedrals, and bond lengths, as well as the general configurations of the molecules monitored, to document this kind of behavior early on. If this kind of behavior is suspected when using readily parameterized molecules, calculating distributions of key angles, dihedrals, and visual inspection of the trajectory files, compared to the values presented by the parameterization of the molecule, and experimental and quantum mechanical reference values, can help in locating and solving the anomalies.

3.7.2 Ergodic Hypothesis

When monitoring the minor conformational changes, which do not involve the crossing of major energy barriers, like rotations around single bonds, we can lean on the so called “ergodic hypothesis”.

The ergodic hypothesis states that the phase space can also work, not only as a measure of “all different possible states of the system”, but also as a reasonable estimate of the paths that the system will take when evolving in time [126,129,140]. That is, if we know the whole phase space, and monitor the properties of the representations of the system in the phase space - that should be analogous to monitoring the time evolution of the same system: the same states should be as often represented in the phase space as in the time evolution trajectory. This assumption is a very powerful one. The ergodic hypothesis states that the frequency one detects one conformation in time, is essentially the same as the frequency one sees that conformation in one single time frame amongst all the conformations present in the system.

This can be formally written for any state variable one wishes to calculate from the time evolution trajectory. This property should, naturally, only depend on the coordinates of the molecules of the system, and have a single time average. So, we assume that our simulation trajectory is in equilibrium.

Here, to give an example, we give the ergodic hypothesis for density $\rho_i(r)$ at a distance r from a given atom i:

$$\overline{\rho_i(r)} = \langle \rho_i(r) \rangle_{NVE} \quad \textbf{(24)}$$

Here, $\overline{\rho_i(r)}$ describes the *time* average of the density over all times considered (averaged over time in a MD simulation), and $\langle \rho_i(r) \rangle_{\mathrm{NVE}}$ describes the *ensemble* average over a large number of initial coordinates in a system of N atoms, in a volume V, at a constant total energy E. Therefore, the ergodic hypothesis states that these two ways of calculating the density of the system give the same result; in rigorous terms the ergodic *hypothesis* states that this is *plausible*.

As the above is indeed a very powerful hypothesis, there are several restrictions for a system to be ergodic – it should not, for example, contain areas of phase space behind so high energy barriers that the time evolution of the system will never reach those parts. In addition, reproducing a large enough sampling requires either long time stretches, or very big system sizes, in order to reach all states of the phase space, or even reasonable estimates for the phase space. Most simulations are believed to be "sufficiently ergodic" to really give reasonable information for the system behavior [126,129,140].

Usually in MD one combines analysis in space and in time when analyzing the equilibrium properties, and in this manner takes full advantage of the ergodic hypothesis – like that one needs to analyze only rather short time ranges, as one can analyze all molecules from each time step. On the other hand, one can increase the accuracy of the estimate by analyzing as many time frames as possible. (Keeping that in mind, we will from now on use ensemble average brackets <> in the text to describe averaging over both the time points and coordinates, if not stated otherwise).

Error estimation for the properties are then made by taking advantage of the other statement of the ergodic hypothesis – that "long enough" equilibrium trajectories can be cut to several smaller ones, and these pieces can be treated as "independent simulation runs". Now one can analyze the properties of each of these, and in that manner get the error estimate for the analysis results from the variation between the trajectories.

The same procedure can be used for all equilibrium properties – for example monitoring the molecular conformation space, intermolecular interactions (for example hydrogen bonding or exposure to water), and the shape and thickness of molecular aggregates or layers.

3.7.3 Crossing High Energy Barriers

One of the most elaborate tests for the quality of the force field parameters is crossing high-energy barriers. For the common events, like rotations around single bonds resulting in conformational isomers of the molecules, it is not so difficult to sample a sufficient number of events to reach statistically significant data. However, one should detect even the most rare events at times – for example a single occurrence of a lipid flip-flop has been detected in simulation [200]. Crossing this kind of high energy barriers, which are rarely crossed and difficult to capture in simulation, can lead to global changes in system properties, like solidifying or melting of the simulated system. This can happen, if the molecule which crossed the energy barrier, is able to act as a nucleation site for a global transition event, which leads to the lowering of this high energy barrier for the surrounding molecules in the system. One such a nucleation event is used as an important test for lipid force fields – the melting of the lipid tails in response to high temperatures (see for example [201]). To investigate the phase transition in the system, the system is simulated with multiple temperatures, having the starting configuration either in liquid phase, or in gel phase, and monitoring the speed of the phase transition in the simulation. Like this one can determine the melting temperature of the lipid tails with an accuracy of a couple of degrees of Celsius, and use the data as a quality test for the force field.

3.8 Running the Simulations

To run a MD simulation, one needs to select a proper software (or code it oneself), set the system to run in the preferred ensemble, set all other parameters (like cut-off distances for interactions, neighbor list update frequency, length of time step, etc.), ensure that all molecules are well constructed, and that the system is energy minimized before starting the simulation run.

First the system is equilibrated in constant volume, and the temperature equilibration is monitored. When the energy of the system has stabilized and the temperature does not change any more, one can add constant pressure to the simulation. Once more the system properties – temperature, pressure and energy – are monitored, and allowed to equilibrate. Once the system is in equilibrium, one can start the production

run, where one gathers the data for the subsequent analysis phase. If the system has bond or angle constraints one desires to release before the production run, one can now release them, and equilibrate the system once more with an aim to reach an unconstrained equilibrium for the system.

When starting the production run one needs to carefully set the data gathering steps – one wishes to store more data from this equilibrium trajectory, as this will be the real simulation used for data analysis. The more the analysis will focus on the time evolution and not only averages of the different properties, the more carefully the data storing frequency needs to be selected. One never stores the coordinates, forces, and velocities of the particles every single time step, but instead something between every 100^{th} and every 10000^{th} step, as the trajectories can easily take tens or even hundreds of gigabytes of memory. A typical time step range is from femtoseconds to picoseconds, and one wishes to store data for a 10 ns -10 μs long simulation. How often one saves the data depends heavily on which quantities one wishes to analyze from it later – what is the time scale of those phenomena. For slow phenomena one saves data only every now and then, and for faster phenomena one needs to save more data more frequently.

A typical production run lasts from tens of nanoseconds to a couple of microseconds, depending on the amount of details in the model. If the model is heavily coarse grained, and contains rather simple molecules, and one wishes to monitor the self-assembly properties of the system, microseconds and even hundreds of microseconds are within reach, but if one has explicit hydrogen atoms, a big protein system, and one wishes to monitor very fast phenomena, like hydrogen bond formation, one probably runs out of storage space after ten nanoseconds already. So, already before collecting the simulation data, one needs to have a solid hypothesis which one wishes to test with the simulation. Not all properties can be analyzed from the same trajectory, and often one needs to run a simulation many times as one wishes to analyze also some properties which could not be seen from the data stored in the first run.

3.9 Analyzing the Results

The most common use of MD simulations is to analyze the trajectory for the equilibrium properties of the system. There are many analysis tools created for different properties, and it is rather straightforward to write new analysis codes which can straight away read the data from the original

simulation output files, and even use the code of the simulation software itself as a part of the analysis. What is required for re-using the MD code in the house-built analysis codes, is of course that the software is distributed under GNU public license, and thus provides the source code free of charge to the users [202]. Of the widely used MD simulation software, GROMACS is the most popular choice if one wishes to have a free source code [131-132, 173]. The users can send their analysis codes to the GROMACS community, and the house-built codes are step by step added to the new official versions of the GROMACS software. The program has benefited from this practice, and nowadays it contains a vast amount of analysis programs coded by external collaborators, and even some major additions to the simulation code itself. For example the possibility of being able to conduct simulations in constant surface tension has been coded outside the GROMACS developing group (in Prof. H. Grübmuller's group in the Max Planck institute, Göttingen).

In the following, as examples, I present five common analyses one often performs when analyzing simulation data of lipid systems: i) the transmembrane density profile, to get insight to the thickness and organization of a lipid layer; ii) the radial distribution function to survey the closest neighbors of the lipid molecules in the plane of the membrane, to see which lipid types closely interact with each other; iii) the diffusion coefficient, to see how fast and how the different molecules move within the plane of a membrane; iv) the order parameter, to tell how ordered the lipid tails are inside a membrane; and v) the undulation profile, to see how the membrane undulates and gives rise to lipids peeking from the lipid layer to the water phase during the simulation.

In GROMACS the density profile, radial distribution function, diffusion, and order parameter can be straightforwardly analyzed with the codes already distributed with the program itself [138]. The undulation analysis code I have used has been built in our laboratory [203], using the free source code of GROMACS, and probably our code is not the only one built for that purpose in the GROMACS implementation.

The basic idea of each of these programs is to take a part of the equilibrium trajectory, and calculate the same property for each of the frames in the trajectory. The quantity to be calculated is then averaged over time, i.e., averaged over the frames of the trajectory (static properties), or its time evolution is monitored (dynamic properties). Even though most of these properties can be roughly estimated by naked eye from some snapshots of the simulation, performing the analysis over long stretches of trajectory quantifies the results much more accurately, and by taking

averages of several similar analyses made for different parts of the trajectory gives valid error estimates for the results.

3.9.1 Density Profile

The density profile is the mass or number density of certain atoms/molecules along a specified axis. It can show, for example, where in the simulation box the different parts of the lipids reside (Figure 13). Averaging this property along all time frames gives a density profile, where one can see the structural orientation of molecules and for example also see how thick the lipid bilayer is on average. Basically, this plot gives the spatial organization of the system, describing how water is distributed with respect to other molecular components, how deep into the bilayer water molecules penetrate, where are the head groups and tails of lipids, etc. (an example of this is shown in Figure 23).

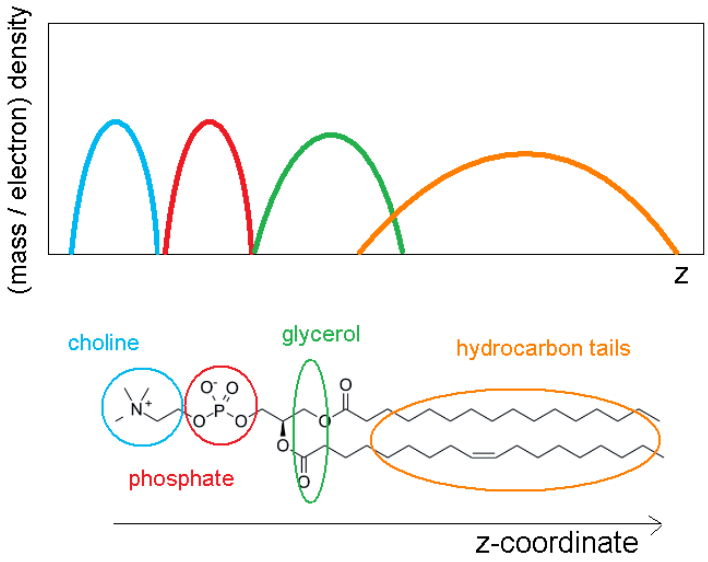

Figure 13. Schematic density profile of a phospholipid along the z-coordinate (the bilayer normal), the different colors denoting different molecular groups in a phospholipid.

If one takes a Fourier transform of the (electron) density profile, one gets the so-called structure factor, which is primary data comparable to results of scattering measurements. This enables comparison between, e.g., X-ray studies and simulations.

3.9.2 Radial Distribution Function

The radial distribution function (RDF) describes the distribution and organization of particles with respect to some particle located at the origin in a two- or three-dimensional space. The distribution is observed from the "point of view" of one particle, radially to all directions (Figure 14). If we now do this for all molecules in the system, and for all time frames we have, and average over the results, we can see which kinds of neighbors surround a given particle.

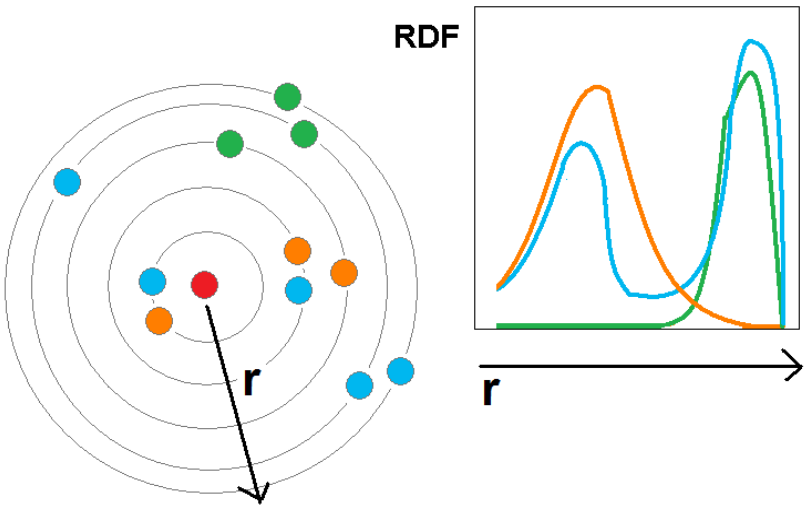

Figure 14. Radial distribution function (RDF). If the red circle looks around it and counts the numbers of its closest neighbors (left), it can draw a RDF plot of the distances of the closest neighbors from itself (right).

The RDF is expressed as a pair correlation function between atom types *X* and *Y,* for which the RDF is to be calculated for. The pair correlation function needs the average local density of atoms *Y* around atoms *X* (i.e $\langle \rho_Y \rangle$), and it compares this average density to the radial densities of atoms *Y* around atoms *X* with different radii (i.e. $\langle \rho_Y (r) \rangle$)

$$RDF_{X,Y}(r) = \frac{\langle \rho_Y (r) \rangle}{\langle \rho_Y \rangle} = \frac{1}{N_X} \sum_{i \in X}^{N_X} \sum_{j \in Y}^{N_Y} \frac{\delta (r_{ij} - r)}{4\pi r^2} \qquad \textbf{(25)}$$

The brackets < > describe averaging over all atoms Y (for each atom X), for all time points of the simulation. From this it is evident that in principle only a short stretch of the simulation trajectory is needed for calculating RDF – it is so heavily averaged over all the molecules that even a couple of simulation snapshots may be enough to calculate it. However, in practice it

is best to take many snapshots at even time intervals from a long equilibrium trajectory to account for appropriate sampling of the configuration space (ergodicity).

3.9.3 Order Parameter

In the context of lipid membranes (and also liquid crystalline systems overall), the order parameter *S* is a measure of conformational order along some axis, for example along the membrane normal direction of a lipid bilayer (Figure 15). Then, a fully ordered tail of a lipid takes the form of a straight rod-like shape (| *S* | = 1). If the tail lies in the plane of the membrane, its order parameter is zero. And, if the molecule is more or less disordered with respect to of the axis, the order parameter takes a value between these two boundaries.

The order parameter is calculated by monitoring the angle θ_z between the axis of interest (usually z-axis of the simulation box), and the axis of the molecule in question (for example the axis of the hydrocarbon chain, or its part such as a bond from carbon *n* to carbon *n*+2):

$$S_z = \frac{3}{2}\left\langle \cos^2 \theta_z \right\rangle - \frac{1}{2} \qquad \textbf{(26)}$$

where the brackets < > describe averaging over lipid molecules, and over selected simulation time points.

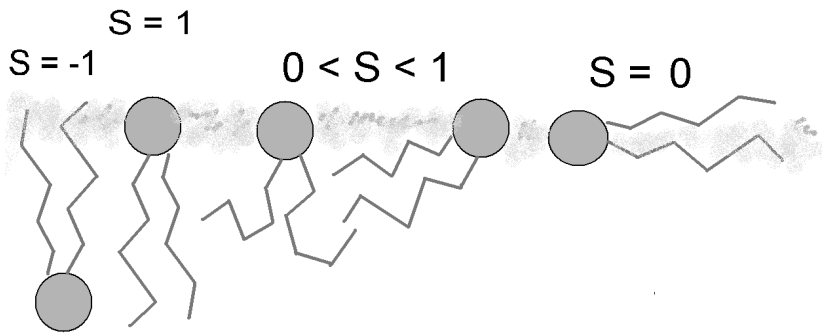

Figure 15. Order parameter along the lipid layer normal. The lipid can be ordered along the normal (order parameter -1 or 1), perpendicular to the normal (order parameter 0), or have values in between these limits.

Averaging the order parameters of all molecules for a long stretch of simulation trajectory can tell if the lipid molecules are organized to form a very ordered solid-like phase, the gel phase, or do they possess a more fluid

conformation. Sometimes one can also see different patches of ordered and disordered lipids – so called phase separation.

3.9.4 Diffusion

There is another way of monitoring the phase separation phenomena in a lipid layer – namely the diffusion of the particles in the plane of the membrane. Usually all components of the system can freely diffuse in the whole layer, but in the case of phase separation there are patches of molecules which do not interact with each other [123]. The molecules inside these patches diffuse mostly only inside their own domain, and that can be clearly monitored by calculating the mean squared displacement (MSD) of the molecules from their starting position, and plotting that against the simulation time. By doing this for all components of the system, one can monitor if some components diffuse at a different rate than others, and is the diffusion free or confined to certain areas of the system (Figure 16).

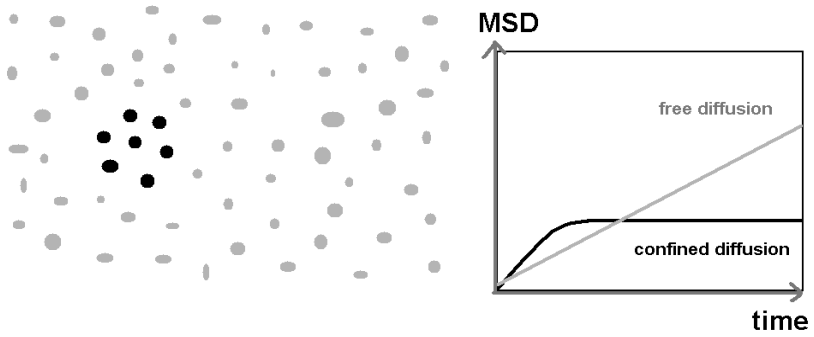

Figure 16. Mean squared displacement (MSD). The black molecules can diffuse only inside their very small cluster – so they show confined diffusion. The grey molecules can diffuse in the whole system, and show free diffusion.

The diffusion coefficient D can then (in three dimensions) be calculated from the linear portion of the mean squared displacements in time by using the so-called Einstein relation:

$$\lim_{t\to\infty} \left\langle \left\| r_i(t) - r_i(0) \right\|^2 \right\rangle = 6Dt \qquad \textbf{(27)}$$

Here the brackets < > denote averaging over all system configurations, and for each time point t along the selected period of the equilibrium trajectory.

3.9.5 Membrane Elasticity

If one wishes to investigate the elastic properties of a lipid membrane, it is crucial to know how the system responds to temperature and pressure by bending and undulating. For that purpose one can build a code measuring the mean displacement of the membrane center from the so-called neutral plane of the membrane [141, 206]. For a bilayer the neutral plane is the plane where the center of the membrane would lie if the membrane would be completely flat. When the membrane bends, it shows equal amounts of undulations on both sides of the neutral plane. By counting the amplitude, wavelength, and frequency of the undulations, one can calculate important data of the membrane properties, like the bending elasticity constants.

Usually the elasticity profile shows two trends for the wave number q – the q^{-2} part characterizing protrusions of single or a couple of molecules from the membrane plane, and the q^{-4} part describing larger undulations formed by the concerted motion of all moving lipids (Figure 17). In the case of bilayers, two types of undulations can be present – the peristaltic mode, where the leaflets of the membrane are bending to opposite directions, and the normal undulation mode, where both leaflets are bending to same direction [49, 141, 206].

Due to the periodic boundary conditions, in simulation systems one can see and monitor only the undulation modes, whose wavelength is smaller than the simulation box size [49, 118].

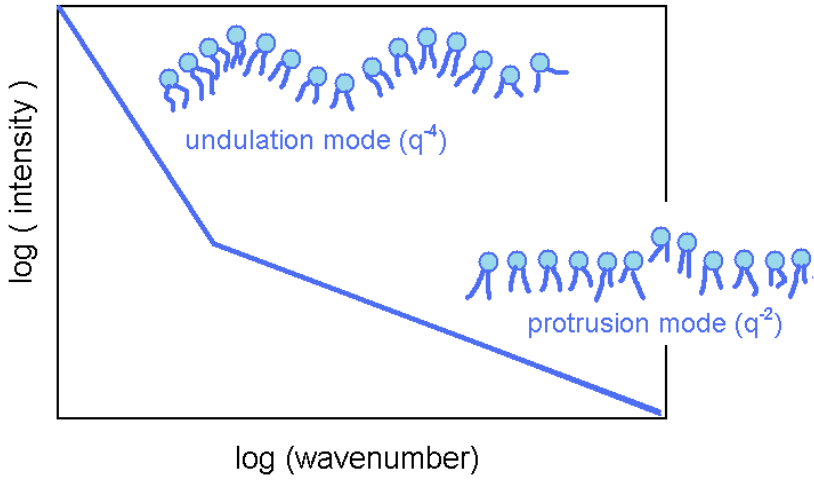

Figure 17. Lipid layer undulation modes. q denotes the wavenumber.

4. Research Objectives and the Candidate's Contribution

The main objectives of the present research program have been as follows :

i) To build appropriate simulation models for tear film lipid layers based on the mass spectrometry lipidome data of Dr. Juha Holopainen's ophthalmology group in the Helsinki Eye Lab for tear films' normal lipid composition. Using the model, the plan has been to simulate the model with various areas per lipid to investigate the effect of surface pressure, and to compare the simulation results to the results of Langmuir trough, atomic force microscopy (AFM) and grace incident X-ray spectroscopy (GIXS) experiments.

ii) To build simulation models for lipid layers whose molecular composition is based on blepharitis patients, and to compare their results to the corresponding data from various other simulation systems – several systems based on either normal or abnormal lipid compositions. Here the idea has been to compare the simulations' results to Langmuir trough measurements.

iii) To use the above models to investigate the tear film collapse mechanism and to explore the role of individual tear film lipids in maintaining the balance of the tear film lipid layer.

Work for the objective i) was conducted by the doctoral candidate during the years 2009-2010, in close interplay with M.Sc. Artturi Koivuniemi in the group of Prof. Ilpo Vattulainen. The ophthalmology research group of Dr. Juha Holopainen was consulted whenever experimental input or references were needed. The first paper of this subject (Paper I below) was published in late 2010, and the paper described both the experimental and

simulation results for the tear film monolayer consisting of lipids in normal tear film [30]. The candidate carried out the simulations, analyzed the simulation data, wrote the first draft of the manuscript for the corresponding parts (the simulation study), participated actively in the writing process, and provided all images and figures needed for the simulation part of the paper. A second publication (Paper II) about a more detailed analysis of the simulation results for objective i) was published in December 2012 [207], and here all the simulations and data analysis were conducted by the candidate. The first version of the manuscript was written by the candidate, and she also participated actively in the writing process in general.

Work for the objective ii) was conducted during the years 2010-2011, in the group of Prof. Ilpo Vattulainen, consulting M.Sc Artturi Koivuniemi when needed for simulation methods, and the group of Dr. Juha Holopainen for experimental data. The research paper for this subject (Paper III) was published in 2012, and the paper described the effect of lipid composition on the stability of tear film lipid layers [41]. It described the structure of a lipid monolayer having the composition of blepharitis patients, and compared that to various different monolayers resembling the tear film lipid layers' normal composition.

The objective iii) is to summarize the results of the project. There was a review article (Paper IV) written about the topic published in 2011 [45]. The candidate participated in the writing process, and provided all data and figures needed to sum up the simulation results for the time being. The candidate also conducted additional simulations and analyzed the previous simulations more carefully to shed further light on the topic. Further, there is a manuscript in preparation (Paper V) about the collapse mechanism of tear film lipid layer [208]. The conclusions in the manuscript are drawn by the candidate based on her own simulations, and she has conducted all data analysis and all the writing of the manuscript by herself. The manuscript will be submitted in the Spring 2014.

The project also led to additional results about the influence of triglyceride parameterization to the monolayer properties, and about the concentration-dependent effects of triglyceride and cholesteryl esters to the stability of lipid monolayers. These simulation results are unpublished at the time of writing this Thesis. The data can be requested from Prof. Ilpo Vattulainen.

Papers forming the basis of this Thesis:

1 P. Kulovesi, J. Telenius, A. Koivuniemi, G. Brezesinski, A. Rantamaki, T. Viitala, E. Puukilainen, M. Ritala, S. K. Wiedmer, I. Vattulainen, J. M. Holopainen. *Molecular organization of the tear fluid lipid layer*. **Biophysical Journal** *99*, 2559-2567 (2010). [31]

2 J. Telenius, A. Koivuniemi, P. Kulovesi, J. M. Holopainen, I. Vattulainen. *Role of neutral lipids in tear fluid lipid layer: Coarse-grained simulation study*. **Langmuir** *28*, 17092-17100 (2012). [207]

3 P. Kulovesi, J. Telenius, A. Koivuniemi, G. Brezesinski, I. Vattulainen, J. M. Holopainen. *The impact of lipid composition on the stability of the tear fluid lipid layer*. **Soft Matter** *8*, 5826-5834 (2012). [41]

4 Rantamaki, J. Telenius, A. Koivuniemi, I. Vattulainen, J. M. Holopainen. *Lessons from the biophysics of interfaces: Lung surfactant and tear fluid*. **Progress in Retinal and Eye Research** *30*, 204-215 (2011). [45]

5 J. Telenius, A. Koivuniemi, J. M. Holopainen, I. Vattulainen. *Smooth collapse of a lipid monolayer: Molecular dynamics simulation study about the art of blinking the eyes*. Manuscript under preparation (to be submitted in Spring 2014). [208]

Here, in each article, the candidate is the leading author of the persons involved in simulations. In Papers I and III, the first author of the articles (Pipsa Kulovesi) was the leading experimental scientist.

Additionally, the candidate has co-authored several additional articles, but they are not discussed in this Thesis:

6 W. Kopeć, J. Telenius, and H. Khandelia. Review: *Molecular dynamics of the interactions of medicinal plant extracts and drugs with lipid bilayer membranes*. **FEBS Journal** *280*, 2785-2805 (2013).

7 J. Telenius, I. Vattulainen, and L. Monticelli. *Visualization of complex processes in lipid systems using computer simulations and molecular graphics*. **Methods in Molecular Biology** *580*, 317-338 (2009).

8 D. E. Kainov, E. J. Mancini, J. Telenius, J. Lisai, J. M. Grimes, D. H. Bamford, D. I. Stuart, R. Tuma. *Structural basis of mechanochemical coupling in a hexameric molecular motor*. **Journal of Biological Chemistry** *283*, 3607-3617 (2008).

9 J. Telenius, A. E. Wallin, M. Straka, H. B. Zhang, E. J. Mancini, R. Tuma. *RNA packaging motor: From structure to quantum mechanical modeling and sequential-stochastic mechanism*. **Computational and Mathematical Methods in Medicine** *9*, 351-369 (2008).

5. Simulated Systems and Data Analysis

5.1 Constructing the Simulation Systems, and Running the Simulations

5.1.1 System Compositions

In the studies, multicomponent lipid systems comprised of DPPC, DPPE, POPC, CO, FFA, TO, and water were modeled (for descriptions of abbreviations, see Table 2). For free fatty acids (FFAs), two slightly different compounds, the saturated palmitic carboxylic acid (PCA) and the monounsaturated oleate carboxylic acid (OCA), were selected.

All systems were described using the coarse-grained representation in terms of the MARTINI model [188], and simulations were carried out with the Gromacs software, version 4.0 [131-132].

The first two papers [31,207] discuss the model for the native state of human tear film. The composition selected for that study was based on the 6:2:1:1 ratio for POPC:FFA:CO:TO lipid system. Two models were constructed – one having oleate as the FFA, the other having palmitate as FFA.

The third paper [41] and the unpublished manuscript [208] discuss the effects of each of the lipid components to the systems' behavior. The abundance of TO and CO lipids in the system was varied, and the response of the system to these changes was analyzed. For the phospholipid component it was investigated how the substitution of PC lipids either totally or partially by PE lipids affects the system behavior.

The simulated systems are listed in Table 2.

Table 2. Simulated systems.

Pure phospholipid monolayers [30,41,207-208]			
100% POPC			
100% DPPC			
100% DPPE			
50% DPPC	50% DPPE		
TFLL normal composition [31,207]			
60% DPPC	10% CO	10% TO	20% PCA
60% DPPC	10% CO	10% TO	20% OCA
Blepharitis lipid composition [41]			
40% DPPC	30% CO	30% TO	
Effect of cholesterol esters to the monolayer [207]			
90% DPPC	10% CO		
Effect of triglycerides and PE lipids to the monolayer [41,208]			
90% DPPC		10% TO	
80% DPPC		20% TO	
40% DPPC	40% DPPE	20% TO	

POPC = palmitoyl oleyl phosphatidyl choline
DPPC = dipalmitoyl phosphatidyl choline
DPPE = dipalmitoyl phosphatidyl ethanolamine
CO = cholesterol oleate
TO = trioleate
PCA = palmitate (free fatty acid)
OCA = oleate (free fatty acid)

5.1.2 Force Field

All systems were described using the coarse-grained (CG) representation in terms of the MARTINI model (version 2.0) [188]. The MARTINI model has been parameterized for biomolecules, especially for lipids, in water solution, at room temperature and atmospheric pressure. The model has been widely used in lipid system simulations, and it has been validated for closely related lipid layers at air-water interfaces [51-52].

The standard MARTINI parameterizations were used for POPC, TG, and PCA. In the oleate chains, the description was identical to the palmitoyl chain except for the third particle, which was assigned to the bead type C3 to describe the double bond. OCA tail was also elongated by one particle to assign the double bond to the middle of the lipid chain. For CE (cholesteryl ester), the MARTINI parameters were built by connecting the cholesterol

and oleate moieties with a bead, which describes the ester bond region [207].

The coarse-grained description of each molecule is based on the MARTINI scheme shown in Figure 18.

5.1.3 Constructing the System

The initial structure of the model was based on a POPC-CO-POPC trilayer surrounded by water, where COs were embedded between the two POPC monolayers and the whole trilayer structure was solvated by a water phase [30, 209]. The system was copied twice to a simulation box, and some COs were removed from the middle of the two POPC monolayers to produce a vacuum region between the POPC layers. The layers were manually shifted further apart from each other to increase the thickness of the vacuum region. Further, some COs were replaced by FFA molecules, and some of the POPC molecules were replaced by TOs. This box was then copied nine times to a single simulation box, to enable monitoring larger scale phenomena (phase separation, some undulation modes).

The final lipid composition corresponded to a system of POPC:FFA:TRIOL:CO = 55:16:9:8 (in terms of the number of lipids in the model system) – which represented the 6:2:1:1 composition hypothesized to be the native composition of human tear film lipid layer. The total number of lipid molecules in the system was 792.

5.1.4 Simulation Software and General Run Parameters

All the simulations were carried out by using the GROMACS software package (version 4.0.2 for the tear film normal composition model [30,207], and version 4.0.4, and version 4.0.7 for the first publication of other compositions, and for unpublished results of the other compositions, respectively [41,208]) [131-132,138]. The simulation temperature was maintained at 305 K with the Berendsen temperature coupling [145] using the time constant of 0.3 ps. For constant pressure runs in the plane of the membrane, semi-isotropic Berendsen pressure coupling was applied, with a time constant of 3 ps and a compressibility of 3×10^{-5} bar^{-1}. All simulations used a time step of 20 fs, and the data was stored every 200 ps.

The production run for each system was ran in the NVT ensemble, which according to a recent review [215] produces similar results for monolayer as the NPT ensemble, if the simulation model is equilibrated carefully.

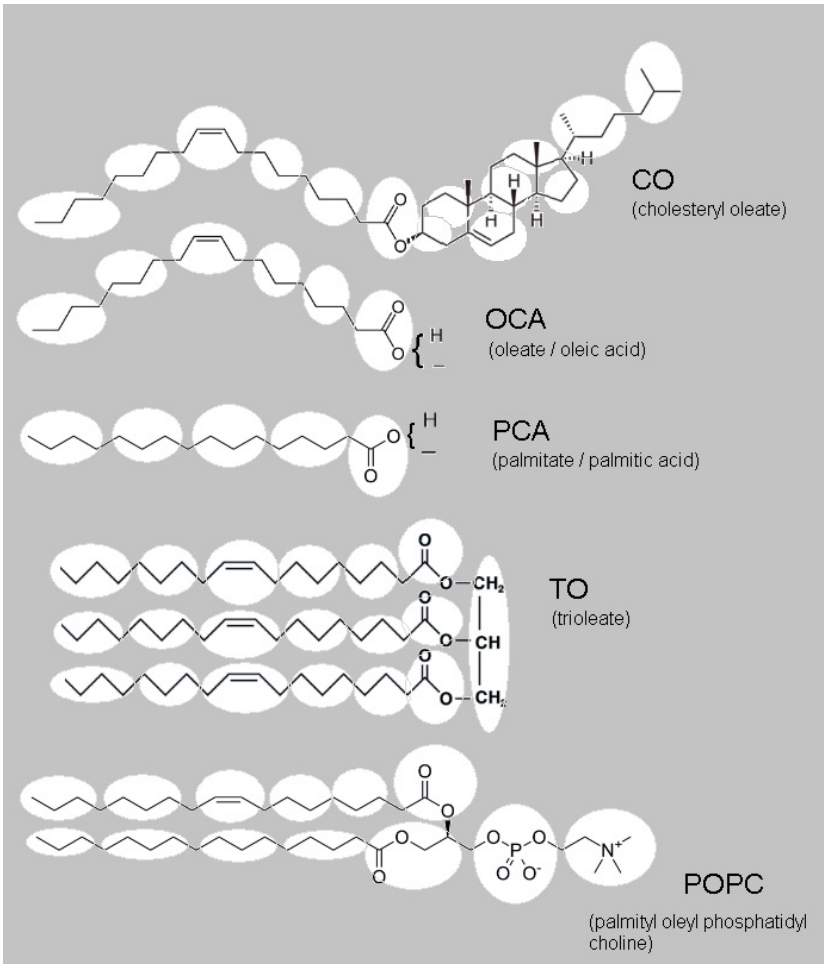

Figure 18. MARTINI mapping for the studied molecules.

5.1.5 Equilibrating the Initial System

The constructed systems (6:2:1:1 POPC:PCA:TO:CO, and 6:2:1:1 POPC:OCA:TO:CO), were subjected for an initial equilibration run in constant volume to fade the boundaries of the nine merged lipid boxes (and later on the same procedure was used to equilibrate the boundary of the added water slab and the simulation system, if needed).

Before each run the number of water molecules per lipid and the thickness of the vacuum layer were checked to be large enough, preventing the constructed lipid system from seeing its own periodic image during the simulation. If extra water molecules were needed in the simulations due to

large undulations or lipid protrusions in the system, the simulation box was merged with a pre-equilibrated water box, and the combined system was equilibrated before beginning the production runs. This protocol was applied any time the thickness of the water layer diminished below 3 nm during the simulation run. The water slabs were never added to systems, which were already compromised (i.e. in which the lipid molecules had reached closer to each others than 3 nm across the water phase), but the water slabs were added before any interaction between the lipid layers ever took place. The same protocol was used for monitoring the vacuum slab thickness, which was kept at ~10 nm at all times. If the smallest vacuum thickness in the system was seen to be less than this, the slab thickness was manually increased and the simulation was started over from the point of interruption.

5.1.6 Initial Constant Pressure Runs

First the system was subjected to constant pressure runs to test the behavior of the lipid layers under pressure change. Hereafter, a series of simulation runs was conducted, each with only a modest increase/decrease in pressure to reach a wide variety of systems with different area per lipid values.

The final structure of a system at a given pressure was used as the initial structure in the next simulation with an increased (or decreased) pressure. This was continued until a wide range of area per lipid values were covered by the simulations (from 23.8 to 73.2 $Å^2$/lipid).

In this thesis the area per lipid is defined simply by dividing the area of the simulation box (xy) by the number of lipid molecules – i.e. the "area per lipid" is the bulk area per lipid; the effect of small scale undulations to the effective area per lipid inside the lipid layer is not taken into account. This is also the principle along which the simulation results are then compared to experimental results for the corresponding area per lipid values.

5.1.7 Constant Volume Runs

The candidates for the longer production runs were selected by analyzing the constant pressure runs described in the previous chapter. Individual frames of these constant pressure runs, having an area per lipid of 42.1, 45.7, 49.4, 53.1, 56.7, 60.4, 64, 67.7, and 69.5 $Å^2$/lipid were selected for constant volume simulations under equilibrium conditions. (These

seemingly arbitrary numbers result from the fact that originally the molecular areas were calculated on the basis of lipid *chain*, and not per lipid molecule – that way these numbers were even numbers (23, 25, 27, 29, 31, 33, 35 ... Å^2 / lipid chain). Only after running the simulations was the notation changed to the more commonly used area / lipid format.)

All simulations were run for 100 ns with a time step of 20 fs, and the data was stored every 200 ps. The cases with 42.1, 49.4, 53.1, 56.7, and 64 Å^2/lipid were found to be the most promising candidates for follow-up simulations, thus they were simulated further until full equilibration was observed (no drift in system energy, pressure, etc.). The subsequent production simulations for the selected systems in equilibrium lasted for a minimum of 200 ns. The total simulated time scale varied between 500 and 800 ns. The equilibrium trajectories were analyzed, and the data was published [30].

It is worth pointing out that the time scales mentioned above do not include the speed-up factor of four arising from the fact that the dynamics in a CG system using the MARTINI description are faster than atomistic dynamics by an approximate factor of four [188]. The effective simulation time considered in the final production simulations was thus 2000 – 3200 ns, of which at least 800 ns corresponded to equilibrium conditions used in analysis.

These equilibrium runs were re-ran and re-analyzed later, to extend the length of the equilibrium simulations further, and to analyze the systems in more detail. The total simulated time scale varied between 800 and 1100 ns for these tear film systems, giving rise to the effective production simulation lengths 3200 – 4400 ns, of which at least 1200 ns corresponded to equilibrium conditions used in analysis. The results of the equilibrium trajectories were analyzed and published [207].

5.1.8 Building Further Lipid Compositions Based on the Initial Model

The initial 6:2:1:1 system simulation box (pre-equilibrated in constant volume to fade the boundaries of the nine small simulation boxes) was used as a basis of new lipid compositions.

First eight lipids were added to both monolayers of the system – to reach a convenient number of 800 lipids per monolayer (instead of the 792 lipids of previous simulations), and the system was pre-equilibrated again.

Then the lipid types were manually changed to reach various TO- and CO-concentrations for the system. The lipid types were interchanged so that

new randomly distributed lipid compositions were reached. All systems were triplicated to reach systems with 100% DPPC, 50:50 DPPC:DPPE, and 100% DPPE as the phospholipid component of the system. The FFA-molecules were all changed to other lipid types, as FFA was, based on new experimental evidence, not important in tear film lipid layer (TFLL) formation after all. The complete list of the produced lipid compositions is shown in Table 2.

After the lipids were transformed to other lipid types, the bond lengths and ring structures were slowly equilibrated with the steepest descent algorithm and subsequent equilibrium runs in constant volume, until no changes in the potential energy profiles were seen. The crude lipid properties of the generated systems were analyzed to ensure that the rings of cholesterol were formed correctly and the tails of the lipids were not entangled in abnormal configurations.

When simulating the systems, the water and vacuum slab thicknesses were monitored at all times, as described previously. All systems were considered with 33300 water beads (each bead in the MARTINI model describing four water molecules), the only exception being the PC/TG/CE 4:3:3 system with 73824 water beads. For the PC/TG/CE 4:3:3 system, 1072 lipids per air-water surface were used instead of the 800, to increase the system size after initial simulations, as the system failed to reproduce monolayer structure.

5.1.9 Simulations of the New Systems

First the structure for each system had the same area/lipid value of ~ 70 Å^2/lipid, and the systems having different areas per lipid were generated by gently applying constant pressure, and by compressing the layer during ~10 ns to a 5Å^2 smaller area/lipid value. The system was equilibrated in constant volume for 10 ns before continuing compression.

For each system the molecular areas between 40 and 70 Å^2/lipid were covered, and systems having molecular areas of 40, 45, 50, 55, 60, 65 and 70 Å^2/lipid were subjected to initial constant volume runs. Based on the initial simulations the systems of interest were selected and subjected to longer production runs in constant volume. All systems were simulated at least for 1 microsecond. Most systems reached equilibrium already in 400 ns, but especially systems having very small areas per lipid craved simulation lengths longer than 1 microsecond to reach equilibrium conditions. The effective simulation time considered in the final production

simulations was thus at least 4 microseconds, of which at least 1.6 microseconds corresponded to equilibrium conditions used in analysis.

The systems selected for full length production runs were PL:TG systems (PL:TG 9:1, and PL/TG 8:2), for which 50, 55, 60, 65 and 70 Å^2/lipid data points were created; 9:1 DPPC:CO system for which 50, 55, 60 and 65 Å^2/lipid data points were created; and finally DPPC/TO/CE 4:3:3 for which 40, 45 and 50 Å^2/lipid data points were created. Both PL/TG systems were ran in triplicates, the PL in the systems being 100% DPPC, 50:50 DPPC:DPPE, and 100% DPPE, respectively.

5.1.10 Reference Systems – Pure PL Monolayers

In the simulations the TFLL systems were compared to the behavior of a pure POPC layer [207].

The POPC layer was constructed by deleting all the CO molecules from the initial POPC-CO-POPC trilayer structure, and multiplying and equilibrating the resulting simulation box in the same manner as the TFLL system was created.

The vacuum and water slab thicknesses were monitored and the system was adjusted (and waters added) accordingly, if needed, just as in the TFLL system simulations. Each system had 33300 water beads in between two lipid layers, and extra water molecules were added when needed (to reach more than 60000 water beads) to prevent the undulating lipid layers to interact with each other.

The constant-pressure runs were applied in the same manner as for the TFLL system, and POPC systems having an area per lipid of 40, 45, 50, 55, 60, and 65 Å^2/lipid were selected for the production simulations. The total simulated time scale varied between 400 and 800 ns for these systems, of which at least 300 ns were carried out in equilibrium. This gave rise to the effective equilibrium simulation time of 1200 ns.

To investigate the effects of lipid head group on the monolayer behavior [41,208], pure DPPC and DPPE and 50:50 DPPC:DPPE reference systems were needed. Those were created from the pure POPC systems by replacing the POPC lipids manually by the corresponding lipid, re-running the equilibration, constant pressure runs, and full length constant volume runs, thus generating the data points for 40, 45, 50, 55, 60, and 65 Å^2/lipid systems for each of the reference systems. For each PC system at least 400 ns data was collected, from which the last 200 ns was used in analysis. The effective simulation time for the analyzed trajectory was thus 800ns.

5.2 Data Analysis

5.2.1 General Analysis Protocol

The analysis of the simulation results was conducted with Gromacs analysis tools (version 4.0.4 [30], and version 4.0.7 [41,207-208]) [131-132,138], and with in-house built analysis codes.

Radial distribution functions, pressure values for the pressure-area plots, order parameters, and lateral diffusion were analyzed with Gromacs 4.0 tools g_rdf, g_energy, g_density, g_order and g_msd, respectively. Structure factors were calculated by using in-house built codes that used the same methodology to calculate the structure factor as described by Murtola et al. [210]. The undulation and peristaltic spectra of the monolayer were calculated by the in-house built code that has been used previously by Niemelä et al. [203].

All analysis results were critically compared to the simulation trajectories themselves to ensure the right interpretation of the analysis results.

The visualization and figures were made with VMD [211] and GIMP [212] programs, and graphs were drawn with the Grace program [213].

We acknowledge the CSC – IT Centre for Science (Espoo, Finland) for providing the necessary computational resources for the simulations.

5.2.2 RDF and Density Profile Analysis

The RDFs for each combination of molecules and the number densities of each molecule along the membrane normal were calculated with the g_rdf and g_density tools (Gromacs 4.0) [131-132,138], respectively. The values were calculated for each simulated system in two ways: i) based on the whole equilibrium trajectory, to get the average value, and ii) by dividing the equilibrium trajectory to 4-5 equally long non-overlapping parts, and analyzing these separately, in order to estimate the error margins. The errors were calculated for the 95% confidence level, and were corrected by a correction factor as the number of repeats was smaller than ten (only four or five repeats for each system).

Bin widths used were 1 Å for center of mass RDF plots (except for PC-PC and PC-FFA using 0.5 Å), and 0.5 Å for head group RDF plots. For the density profile analysis the simulation box was divided into slices that were

0.54 Å thick [30], or 1 Å thick [207]. The error bars determined in this manner are shown in the figures.

5.2.3 Selecting the Neutral Plane for Lipid Layer Fluctuation Analysis

Assuming the layer to be aligned in the xy-plane (z being the coordinate along the layer normal), elastic out-of-plane fluctuations of membranes are typically described by the height–height correlation function h(x,y), which describes the deviation of each part of the membrane with respect to the "neutral plane" of the membrane. The neutral plane is the xy-plane, which divides the undulation amplitude in half – half the undulation amplitude is above, half below this neutral plane – the undulation takes place to both sides of this neutral plane. (The neutral plane is like the zero level in the sin(x) function – half of the amplitude of the undulating function is above, half below the neutral "zero" plane).

For bilayers one can, based on the symmetry of the membrane, usually assume that the neutral plane lies between the two monolayers of the bilayer. For monolayers, it is more difficult to select a proper neutral plane, as there is no obvious choice based on symmetry. However, one can assume that as surface tension acts at the interface of air and water, height fluctuations correspond to those where the air-water interface acts as the neutral plane. The air-water interface is not an infinitely thin plane, however. We therefore calculated height fluctuations using several different options for the neutral plane, considering the planes at the level of, for example, PC choline groups, between the glycerol groups, and between the first carbons of the carbohydrate tails. The elastic fluctuation spectra of these cases did not differ significantly. As we got smallest error margins for the spectrum calculated using the plane between phosphate PO4 and choline NC3 groups, we used it as an estimate of the neutral plane in the analysis.

5.2.4 Producing the Pressure-Area Isotherms

Surface tensions for the systems were calculated as described in literature (for instance, Lucas et al. [214] and Baoukina et al. [51]), taking into account that in the simulation box there were two monolayer interfaces. The surface pressure values were then calculated from the surface tension values by applying the experimental value of 72 mN/m for the surface tension of an air-water interface.

5.2.5 Validating the Simulation Methodology

The simulation method was validated by calculating the pressure-area isotherm of the DPPC system and comparing that to previously published simulation results for DPPC monolayers (Figure 19) [51,215].

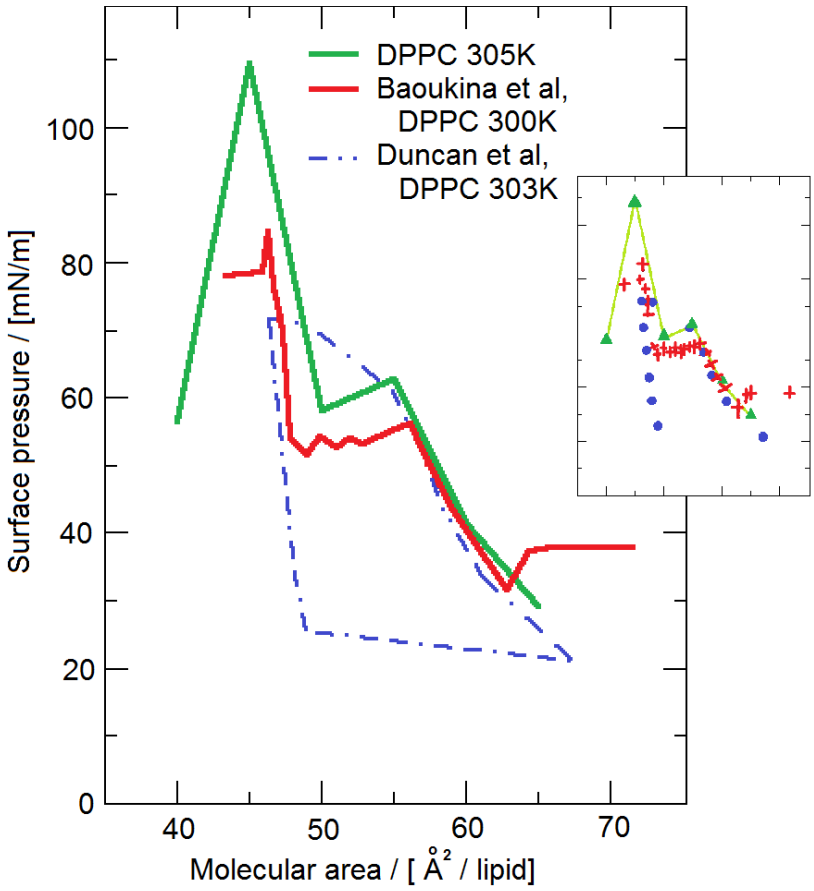

Figure 19. Comparing the simulation pressure-area isotherms for DPPC [208]. Comparison of the pressure-area isotherm of the simulated DPPC system (green) to previously published simulation results by Baoukina et al. (red) [51], and Duncan et al. (blue) [215]. The inset shows the data points in each curve. All the surface pressure values have been transformed from surface tensions by using a vacuum-water surface tension value of 72 mN/m. Error margins are approximately the same size as the width of the line. With the permission of the original authors.

As monolayer simulations are not common, finding suitable simulation sets to validate the selected simulation approach is not a trivial matter. Figure 19 depicts the results of three existing monolayer simulation studies

for DPPC monolayers. All three are based on the MARTINI force field, and they were carried out in temperatures rather close to each other. All these simulation studies, however, differ in the approach used to generate and equilibrate the systems, and thus the results do not match quantitatively.

Duncan et al. [215] used a series of constant surface tension simulations (Figure 19, dotted blue line). The surface tension was changed step by step, and at the highest possible surface pressure value (the last point before layer collapse) the direction of the surface tension change was reversed, and the system was brought step-by-step back to the initial value. Baoukina et al. [51] used the method called "constant change in pressure" – and ran the whole isotherm in a single run (Figure 19, red line). The data provided in this thesis (Figure 19, green) is based on a series of constant volume runs, connected to each other by constant pressure runs.

We can see that when surface pressure is low, all these simulation methods agree (Figure 19, on the right). In higher surface pressures the "constant pressure change" and "constant volume accompanied by constant pressure runs" seem to follow same general trend (from right to left in the picture) – first increasing the surface pressure, then slightly decreasing it, followed by an abrupt increase in surface pressure and finally a layer collapse. In contrast to this, the surface tension based simulation shows a continuous and smooth surface pressure landscape.

The surface tension approach may correspond to a situation where the system experiences a very smooth change in its surface state, thus resembling a surface pressure change taking place in long, experimentally reachable timescales (milliseconds, seconds, minutes). In experimental results for DPPC (not shown here, see for example [215]), one sees more or less this kind of behavior – no abrupt transition points along the isotherm.

For the run in "constant pressure change" [51], a strong and abrupt collapse takes place already at surface pressures well tolerated by the system when using the surface tension approach. This may result from the simple fact that simulation timescales are actually extremely short in real time – the layer may not be able to adapt to pressure changes within tens, or hundreds, of nanoseconds. The layer responds by breaking abruptly.

For the data presented in this thesis, the selected approach was based on constant volume simulations of one microsecond, accompanied by constant pressure runs to generate differential surface areas for the system. This method seems to follow the general trend of the constant-pressure-change approach, producing slightly higher surface pressure values. It is, however, hard to know how big the difference between these two approaches actually is, as the data produced for the thesis was also simulated in a higher

temperature – therefore all values scale to higher surface pressures only due to the temperature difference. Nonetheless, relevant to this work is to realize that the present data is qualitatively consistent with earlier studies when comparison is possible.

6. Results for Tear Film Lipid Layer with Its Normal Lipid Composition

The studied systems (100% PL, and 6:2:1:1 PL:FFA:TG:CO tear film lipid layers) were investigated by our team via simulation models, and also via experiments by our collaborators.

The details of the experimental methods can be found from the first publication [30]. Here, even though the candidate has not conducted the experiments herself, she will provide the reader with a brief outlook to the methods and results, since it is quite appropriate to compare the simulation data to the experimental findings [30, 207]. Only after describing the experimental methods and results, the simulation results for each system will be described and compared to their experimental counterparts.

The decision of showing the experimental data before the simulation results arises from the facts that the project was i) initiated and coordinated by a medical research group, and thus ii) the simulations were built up to shed more light on the conducted experiments, or iii) simulations were ran to consider a larger range of conditions than what was possible by experiments only. The simulations serve mainly as a facilitator in interpreting and complementing the experimental results, thus we first briefly discuss experimental data and then compare our simulation results with them.

Even though the overlap of the experimental and simulation data points in the compression isotherm is not large, and not all the experiments can be straightforwardly compared to the simulation data, the simulations did indeed produce valuable hypotheses and illustrations of what may take place in the experimental systems. Also, the simulations produced data that is not possible (or that would be very difficult) to reach with the experimental setups – such as data about layer structures close to or at the collapse surface pressure.

6.1 Experimentally Observed Compression Isotherms

The compression isotherms were measured for the PL and TFLL systems by Langmuir trough (Figure 20). The main aspects of experimental setups are discussed in Appendix E.

The PL system reached the 40 mN/m surface pressure without any phase transitions (Figure 20), describing a system where the PL lipids are in the liquid-expanded state at all times, or, if a transition to the liquid-condensed phase was reached, it was not a concerted one showing up in the compression isotherm. The expansion of the PL system, as no transition states were encountered, showed no hysteresis, and followed exactly the same path as the compression.

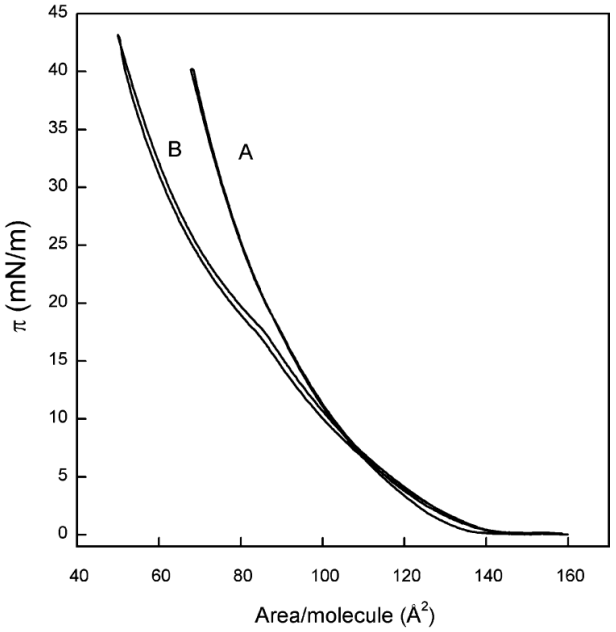

Figure 20. Langmuir trough isotherms shown (A) for the PC system – PC being egg PC, and for (B) the TFLL system [31]. π denotes surface pressure. Modified from publication [31], copyright Biophys.J., Elsevier 2010 (reprinted with publishers, and co-authors' permission).

The TFLL layer, on the other hand, reached the 40 mN/m state via one transition state, and slight hysteresis was detected (Figure 20). The hysteresis here confirms the existence of the transition state, as a transition is a nucleation phenomenon which needs i) right conditions to happen, and ii) a nucleation site from which the transition then spreads to the whole layer. This means that the transition in the compression isotherm is seen at slightly higher surface pressure values (pushing the system "over" the

transition), and the transition in the expansion isotherm is seen at somewhat lower surface pressure values (giving time for the system to nucleate the global relaxation of the ordered, condensed structure). This result means that the TFLL system is already at 40 mN/m in some kind of condensed state. What kind of transition this exactly is remains to be clarified. The most probable answer is that there is global ordering of the lipid tails to a more condensed structure, or that phase separation takes place to pack some of the lipids to separate domains in the layer to make the packing on the lipid layer's surface more efficient.

At all area/lipid values (after exiting the zero surface pressure gas phase) the TFLL layer was able to compress more easily – smaller areas were reached with less force from the trough. This is consistent with the simulation results – also in simulations it is seen how the TFLL composition is more potent in adapting to the compression of the layer.

In simulations (described in detail in subsequent chapters) several transition states of the lipid layer are seen (including lipid tail ordering transitions, the TG and CE lipid flipping to the other side of the membrane, and finally the formation of TG-CE clusters to the air side of the interface). For PL simulation system one can see the lipid tails' order transition, and finally the collapse and folding of the layer. All these phase transitions are however at very high surface pressures, already rather close to the collapse of the layer – and experimental results were not gathered from these structures.

However, there is some overlap in the simulation and experimental results – the largest area per lipid in simulations can be compared to the experiments straightforwardly. The comparable structures have area/lipid values of 65-70 $Å^2$/lipid (65 $Å^2$ for all others, 70 $Å^2$ for the experimental PL system). The PL system in both the experiments and simulations show a homogenous monolayer. In simulations this layer is in the liquid-expanded state, and in experiments it shows behavior, which would fit to either the liquid-expanded or liquid-condensed state.

The TFLL system shows in both simulations and experiments a case where the first transition has already happened – in simulations this transition is the flipping of (some of) the TG head groups to the air side of the membrane. It is thus possible that the first transition seen in the experiments is actually the flipping of the TGs, and not related to lipid tails' conformational change or a global phase transition event, after all.

6.2 Experimental Results for Near-Gas Phase Phenomena in the Lipid Layer

Several measurements of the lipid layer structure were done in the near-gas-phase region of the pressure-area diagram (around 20-30 mN/m). These included grazing incidence X-ray diffraction (GIXD), atomic force microscopy (AFM), and Brewster angle microscopy (BAM) [30].

GIXD was done in 20 mN/m, and for PL system it showed no ordering of lipids to domains in the lipid layer. For the TFLL it showed unequal distribution of lipids, predicting phase separation to two separate lipid phases, distributed evenly every ~ 55 nm distances on the layer surface. The other of these lipid phases was predicted to be probably a solid phase, and to be comprised mostly of FFA and TG.

The BAM results show the same homogenous structure for the PC layer, and also present further evidence for the early stage phase separation in this system. Thicker areas in the layer were seen already at low surface pressures, and they were proposed to be demixed condensed FFA/TG islands produced already during the spreading process.

The AFM was done in both 20 mN/m and 30 mN/m pressures. For PC layers a homogenous layer was detected, and for TFLL, multilayer structures were seen already at these low surface pressures. Both PL and TFLL systems also showed some holes in the membrane structure – illustrating that the surface of the air-water interface may not be entirely covered by a lipid layer.

When these results are compared to the simulation results at 20 – 30 mN/m, the comparison is not very straightforward. The simulation systems for those low surface pressures show mostly a pure vacuum-water interface, on top of which there were lipid fleets having a homogenous composition, and these were in the liquid-expanded phase. Even though we saw in the AFM measurements that some holes in the lipid layer can be seen in the experiments too, the behavior seen in simulations – lipids not spreading onto the layer at all, but leaving most of the interface free – is highly unlikely to be a realistic model for this part of the phase diagram.

This artifactual behavior is most probably driven by the strong repulsion term in the interaction of lipid tail particles and water particles in the MARTINI model. Even though the lipids should be able to lie horizontally on the vacuum-water surface interface when the system is in the gas phase (or close to the gas phase), the force field repulsion terms restrict that from happening, as water-lipid tail contacts are highly penalized within the force

field. This leads to generation of separate lipid domains exhibiting liquid-expanded behavior, and completely lipid-free vacuum-water interface domains. This clearly shows that the Martini parameterization which was aimed to reproduce the properties of bilayers – one of which is to repel all the water molecules from the very inside of the membrane – is not always suitable for monolayer simulations as such. One solution to overcome this problem would be to fill the vacuum side of the system with so called "dummy particles" which would be visible to all particles in the system (having a physical size, that is), but which would have attractive interaction with only lipid tail particles. Another option would be to simply adjust the water-lipid tail repulsion term – however meddling with the already parameterized interactions should be proceeded with care and caution. The dummy particle approach would be easier, and much safer, too. This modification of the system description could then compensate the repulsion of the water particles to the lipid tails at the very vacuum-water interface, and produce more realistic interfacial behavior for the system for low surface pressures.

6.3 Simulation Results

6.3.1 The PL and TFLL Monolayers Respond Differentially to Small Interfacial Areas

Snapshots from constant-volume simulations for the many-component TFLL (6:2:1:1 PL:FFA:CE:TG) and the one-component PL layer systems in equilibrium are shown in Figures 21-22. When subjected to a gradually smaller vacuum-water interfacial area in the simulation box – smaller area/lipid values than in a relaxed planar PL lipid bilayer in water – the responses of the pure PL system and the TFLL system differ significantly.

The pure PL system responds to small interfacial areas by bending the lipid layer to a highly undulating structure (Figure 22) – the whole interface folds to steep undulations, as PL lipids are essentially amphiphilic – all of them prefer to reside in the interface between the vacuum and water, and bending the interface via an emerging undulating structure is a way to ensure this when only a small lateral interfacial area is available.

In stark contrast to this, the TFLL system responds to small vacuum-water interfacial area by excluding the neutral lipids (CE, TG) from the

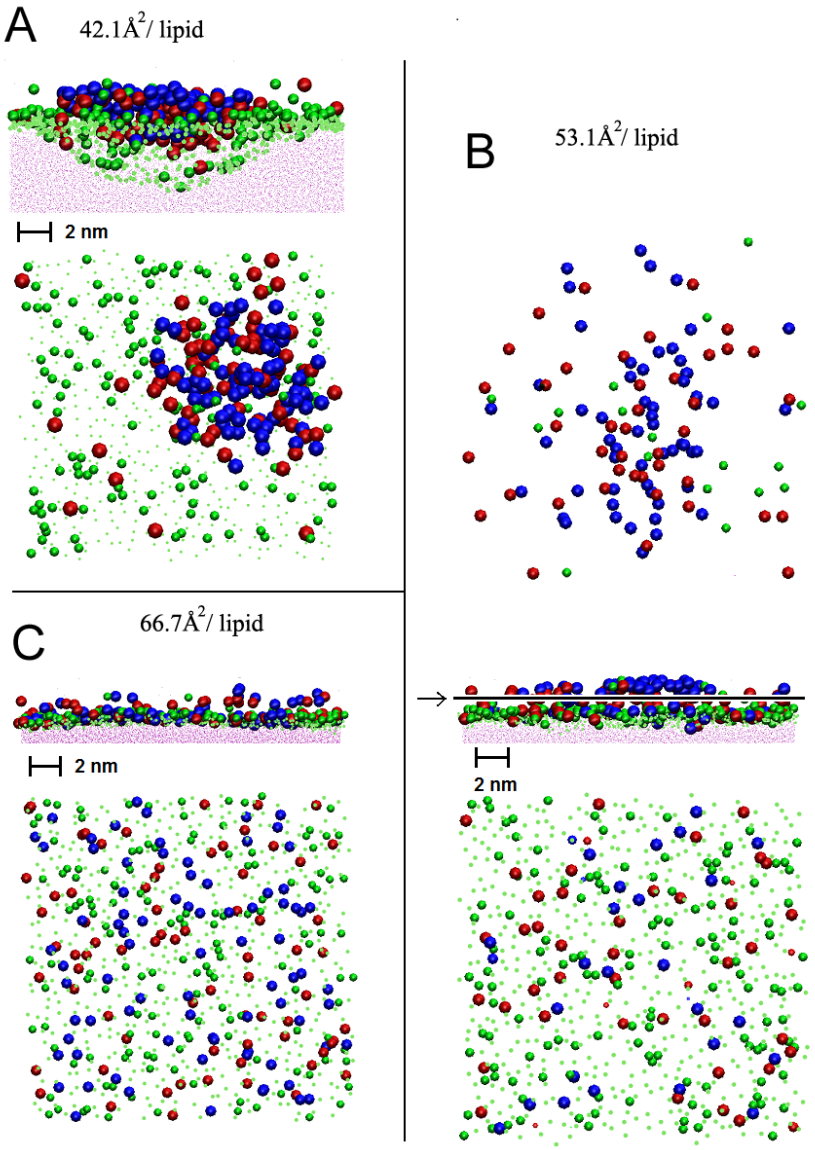

Figure 21. Snapshots from 6:2:1:1 PL/FFA/CE/TG with (A) 42.1 Å²/lipid, (B) 53.1 Å²/lipid, and (C) 66.7 Å²/lipid [207]. (A) System shown from (top) the side and (bottom) the air view of the lipid layer. (B) System depicted from (top) the air view, (middle) the side, and (bottom) the water side of the layer. (C) Layer shown (top) from the side and (bottom) the water phase. Color code is as follows: Green small dots refer to the PL (POPC) phosphate group; blue beads stand for the TG glycerol group; red beads show the CE ester group; green beads denote the FFA (PCA) carboxyl group, and water is shown as a purple mesh. Reprinted from Langmuir [207] with co-authors' and publishers permission, copyright 2012 American Chemical Society.

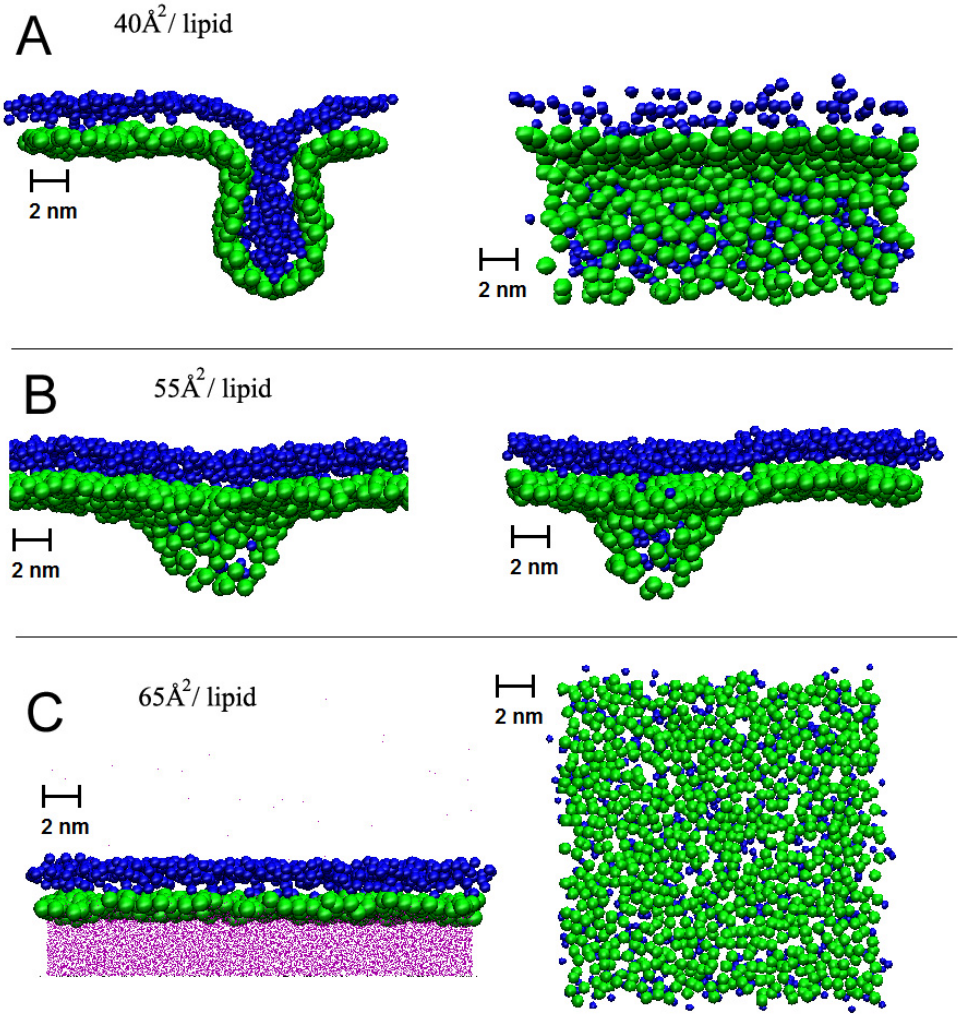

Figure 22. Snapshots from one-component PL (POPC) simulations with an area of (A) 40.0 Å²/lipid, (B) 55.0 Å²/lipid, and (C) 65.0 Å²/lipid [207]. Blue beads stand for the four last carbon atoms of the PL hydrocarbon tails.Green beads denote the phosphate group of PL. Purple mesh in panel C(left) describes water molecules. Panels (A) and (B) show systems from the side of the layer; the figure on the right has been rotated by 90°. Air is above, and water below the lipid layer. Panel (C) depicts the system from (left) the side and (right) the water phase of the layer. In the side view, air is above and water below the lipid layer. Reprinted from Langmuir [207] with co-authors' and publishers permission, copyright 2012 American Chemical Society.

immediate vicinity of the interface (Figure 21). The CEs flip and place their ester groups and cholesterol moieties deeper into the air phase. The TGs flip as well, and form TG headgroup clusters to the air side of the interface by interacting with each others via their slightly hydrophilic glycerol regions. This helps the interface to stay essentially planar even when only a small interfacial area is available for the lipids.

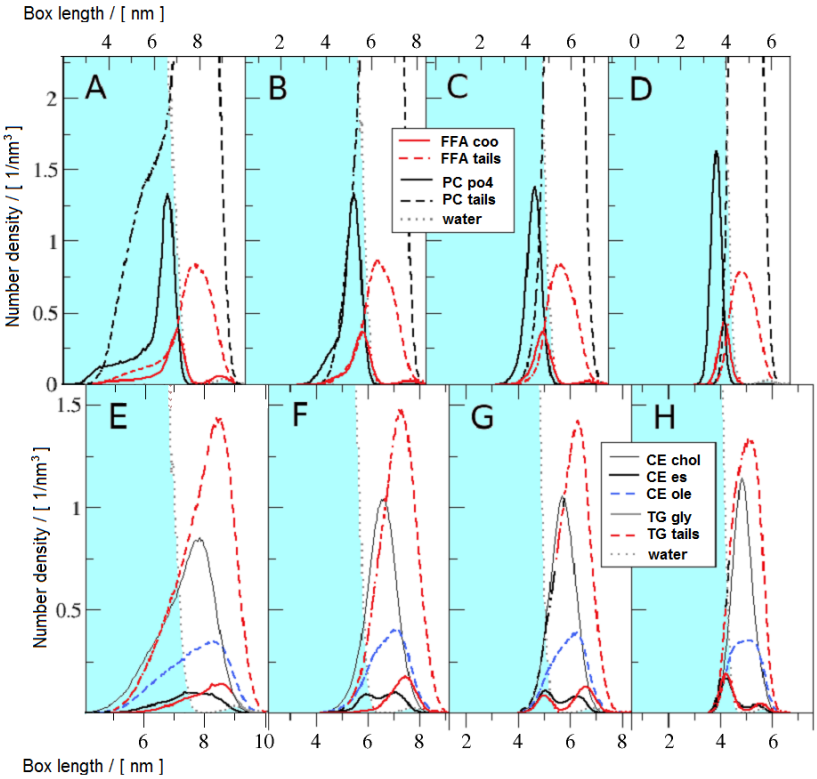

Figure 23. Number densities along the monolayer normal for 6:2:1:1 PL/FFA/CE/TG simulations, when FFA is PCA [31]. Water is on the left (light blue), and air on the right (white). The figures are aligned to each other by matching the positions of PL tail and water peaks to clarify the trends in densities. Panels (A)–(D) describe data for density profiles for PL and FFA at 42.1, 49.4, 56.7, and 66.7 Å2/lipid, respectively. Panels (E)–(H) in turn providesimilar density profiles for TG and CE. Abbreviations stand for "FFA coo" = palmitate carboxyl group; "PC po4" = POPC phosphate; "FFA tails" = palmitate hydrocarbon tails (center of mass (cm)); "CE chol" = cholesterol rings of CE (cm); "CE es" = ester group of CE; "CE ole" = oleate tail of CE(cm); "TG gly" = TG glycerol (cm); "TG tails" = hydrocarbon tails of TG (cm). Reprinted from Langmuir [207] with co-authors' and publishers permission, copyright 2012 American Chemical Society.

Snapshots and density profiles (Figures 21 and 23) for the TFLL system show how the TGs readily nanoscale phase separate, early on when the interfacial area is diminished, indicating that the surface activity of TGs in the PL layer is smaller than the surface activity of CE. This is consistent

with the finding that the area taken by TGs (with three ester bond regions) at the surface of a monolayer is larger than the area taken by CEs (with one ester bond region). The exclusion of weakly polar but spacious TG glycerol groups from the air-water interface, leads to the flipping of these groups to the other side of the lipid layer. The weakly polar TG head groups then cluster with each other at the vacuum interface, forming with the interfacial PL and FFA lipids a "hydrophobic semi-bilayer" structure (Figures 21, 23).

When the interfacial area is further diminished in the TFLL system, the CEs separate from the interfacial lipids as well, and penetrate between the "semi-bilayer sheets" formed due to TG phase separation. This CE-TG phase-separated state of the system is essentially lipoparticle-like so that on the water side the CEs are lined by surface lipids (PL lipids and FFAs), and from the vacuum side by TG glycerol groups. In the inside of the aggregate there is an unorganized melt of CEs and TG tails. In the smallest interfacial areas simulated, essentially all TGs and CEs reside in these lipoparticle-like structures.

Comparing the TFLL-mimicking systems to one-component PL layers with a corresponding area per lipid reveals the superiority of the neutral-lipid containing TFLL over the pure PL layer under high lateral pressures (during blinking of the eye): for small areas per lipid, the PL layer forms long unstable protrusions/tethers toward the water phase, while the TFLL system responds by just bending in a concerted fashion to reach a stable lipid layer. It is possible that neutral lipids, and especially triglycerides, assist the phospholipid layer to fold in an appropriate way during the various stages of the blinking process.

In the following chapters the detailed results of the RDF analysis, density profiles, lipid tail ordering, diffusion of molecules on the surface of the layer, and protrusion and undulation behavior of the surface lipids in both TFLL and PL systems are presented.

6.3.2 Density Profiles Show TG and CE Head Group Exclusion from the Interfacial Layer in the TFLL system

The density profiles were calculated along z-axis, which is essentially the axis along which the vacuum-water interface lies in the system. For the fold-forming structures (in the case of pure PL), and the lipoparticle-like protrusion-forming structures (in the case of the TFLL system), the z-axis does not coincide with the lipid layer's normal in all points of space. This means that the "crude interface" which continues to reside along the z-axis differs from the actual interface, which is formed by bent lipid structures

not residing only in the xy-plane. For these folded and curved lipid structures we can see in the density profiles also the thickness of the fold in the overall structure, in addition to the smaller scale differences telling how the molecules pack along the interface in relation to each others.

It would of course be possible to calculate the density profile along the local normal of the lipid layer, too. However, that would have required quite substantial resources to design an algorithm able to describe the contour of the lipid layer along a complex fluctuating interface. Therefore, for the present purpose, we decided not to dedicate our efforts for that purpose (below we have used the same practice in other related situations).

For the stress-less interface, having an area per lipid close to the area per lipid found in bilayers (64-67Å^2), the pure PL system and the TFLL system behave exactly the same, when it comes to organization along the vacuum-water axis (the lipid layer normal) (Figures 21-23). All lipid components lie in the planar interface, polar groups towards the water phase. As the system is very close to its energy minimum, no folding behavior is seen for the PL system, and no neutral lipid phase separation is seen for the TFLL system. In the TFLL system the head groups of PLs are in straight contact with water, followed by the FFA carboxyl groups, which also lie very close to the water-interface. A little bit deeper in the lipid layer, but still reaching water contacts, lie TG glycerol and CE ester groups. For TGs, cholesterol, and long chain alcohols, this behavior has been observed in previous simulation studies [219, 224] and predicted by experiments [30, 221, 223, 225-226]. CEs, as esters of long chain alcohols and cholesterol, can be expected to behave in a similar way, even though the ester linkage makes the molecule less surface active than cholesterol and fatty alcohols.

When the surface pressure is increased, the TG head groups flip from the water phase to the vacuum side of the interface (Figures 21-23). At the area per lipid of 56.7 Å^2, more than a half of TGs have flipped upside down exposing the ester bond regions to the air phase, whereas most of the ester bond regions of CEs are still located facing the water phase. The flipping of CEs becomes more apparent when the area per lipid is further decreased.

The reason for this phenomenon is that neutral lipids (TG and CE) do not lower the surface tension of the system considerably, and at high surface tensions (small area/lipid values) they are readily displaced from the interface by FFAs and PLs, which are more effective as surfactants. This leads to the flipping of the spacious TG and CE head groups to the air side of the interface.

Furthermore, lipids containing double bonds or cholesterol moieties (like TO and CO), disturb the molecular packing of FFAs and PLs within the

monolayer; the efficiency of packing and the effect it exerts on the entropic contribution of free energy play an increasingly important role when surface pressure is increased. This entropic effect, which drives exclusion of all “too spacious” and “not neatly packing” hydrophobic moieties from the lipid layer at high surface pressures, can then complete the phase separation process and drive the system to form separate lipoparticle-like TG-CE aggregates to the air side of the interface. This nanoscale phase separation was seen to be nearly complete at a lateral interfacial area of 42.1 Å^2/lipid, when almost all TGs and CEs have been excluded from the interfacial lipid layer. Only the FFAs and PLs remain in the interfacial layer in a system having such a small interfacial area, as they can serve as effective surfactants, and also can pack efficiently to a condensed monolayer structure to minimize the lateral pressure inside the lipid layer (Figures 21-23).

The TG and CE exclusion is more pronounced for the TFLL model containing OCA, as the proportion of unsaturated surfactants is increased and the subsequent increase in pressure in the interfacial layer excludes the oleate tails of TG from the interfacial layer faster than in the case of PCA.

6.3.3 Radial Distribution Functions Show TG and CE Clustering in the TFLL System

Radial distribution functions for the TFLL system components (TG, CE, FFA lipids, and polar lipids (FFA and PL together)) were averaged over the xy-plane in 2D at several different surface pressures. The vacuum-water interface forms essentially to the xy-plane, and for most surface pressures considered also the lipid layer resides in this plane. For the fold-forming structures (in the case of pure PL), and the lipoparticle-like protrusion-forming structures (in the case of TFLL system), the RDF shows the lipid organization in the system as a projection to the xy-plane.

The polar lipids (PL, FFA) are uniformly distributed along the membrane plane for all surface pressures considered (Figure 24). The FFA molecules, however, show slight preference in pairing with other FFA-molecules, which shows as a peak in the RDFs on all surface pressures. The peaks shift closer together as a response to higher surface pressure, describing the tighter packing of the surfactant lipids at the interface in higher lateral pressures.

The nonpolar lipids (TG, CE), on the other hand, distribute uniformly along the membrane plane only with the highest area per lipid considered (64 Å^2/lipid; see Figure 24 (bottom)). At intermediate surface pressures

(area of 56.7 Å^2/lipid; Figure 24 (middle)) one finds already quite significant clustering of neutral lipids. TGs and CEs get together, forming domains whose sizes are in the multi-nanometer regime. When the surface pressure is increased further (area 42.1 Å^2/lipid), the trend becomes more pronounced (see Figure 24, top): aggregates comprised of TGs and CEs increase in size and the concentration of these lipids outside the TG- and CE-rich domains decreases radically.

Thus, as a response to increasing surface pressure, TG molecules condense together, forming neutral lipid-containing pileups rich in TG. This is just a quantification of the effect we saw in the snapshots – the glycerol groups of the TFLL are excluded from the water side of the interface and, after being forced to the air side of the interface, they cluster together via electrostatic interactions. For CE, this effect is not so clear and becomes more evident only at the highest pressures, when the CEs get incorporated into the TG clusters and the lipoparticle-resembling aggregates form. Overall, these features are consistent with related ordering effects found in structure factors of cholesterol containing lipid bilayers [227].

6.3.4 Order Parameters Show Differential Behavior of the TFLL System

The lipid tail orientations can be calculated for all lipids of the system, along the whole trajectory. The average order parameter of the tail then tells how far from being aligned head-tail to the water-vacuum interface the hydrophobic lipids tails tend to lie. As this is a coarse grained system, we cannot reproduce the NMR (nuclear magnetic resonance) order parameters, as not all atoms are represented in the model. The order parameter is thus only a qualitative measure of the ordering, and presenting only the trend of “more ordered” or “less ordered” layers – not exact values for chain order. We can, however, see the phase transitions from fluid phases to the gel phase via this approach quite easily.

The lipid tail order parameters were calculated along the z-axis, like density profiles, and they show the tail ordering along the normal of the lipid layer. As mentioned earlier, for the fold-forming structures (in the case of pure PL), and the lipoparticle-like protrusion-forming structures (in the case of TFLL system), the z-axis does not coincide with the lipid layer’s normal in all points of space. This means that we can see two opposite trends in the order parameter. The first trend, the lipid chain ordering, is

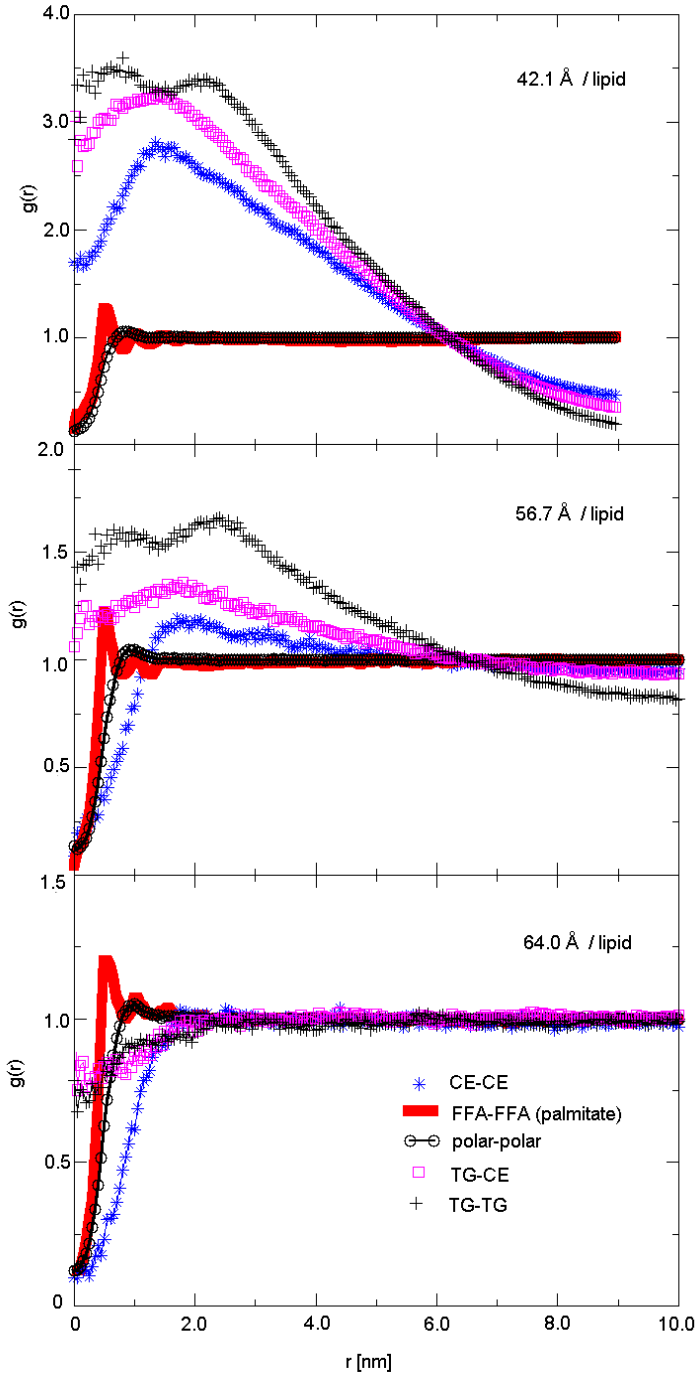

Figure 24. Radial distribution functions (RDFs), g(r), in the 6:2:1:1 PL/FFA/CE/TG system for the center of mass positions projected to the 2D membrane plane [207]. Here, "polar" stands for PL and FFA lipids together. For neutral lipids with small area, the RDFs at large distance go down below one due to aggregate formation. Reprinted from Langmuir [207] with co-authors' and publishers permission, copyright 2012 American Chemical Society.

clearly visible in the low to moderate surface pressures, where no folds and protrusions are forming into the lipid layer. The second trend, tilting of the principal axis of the lipids as the protrusions and folds form, then create order parameter data, which proposes that the ordering of the lipid tails would decrease abruptly when the folding behavior begins. This is of course not true, and can be confirmed by looking at the snapshots of the systems – the ordering of individual lipid tails along the interface normal within the system continues increasing, but the effect is masked by the fact that the true interface does not reside along the z-axis for all parts of the system.

All in all, the higher the lateral pressure, the more ordered the lipid tails in the systems. The pure PL system's lipids show higher tail ordering than TFLL phospholipids for all surface pressures considered, however. The tear film composition thus seems to hold the layer more fluid – even under high lateral pressures.

For both TFLL and pure PL systems, the increasing surface pressure has the most potent effect on the terminal region of oleate chains, where the order parameters in the systems increase by a factor of 2 (Figure 25). That is, the systems respond to an increasing surface pressure by mainly increasing the order in the unsaturated hydrocarbon chains.

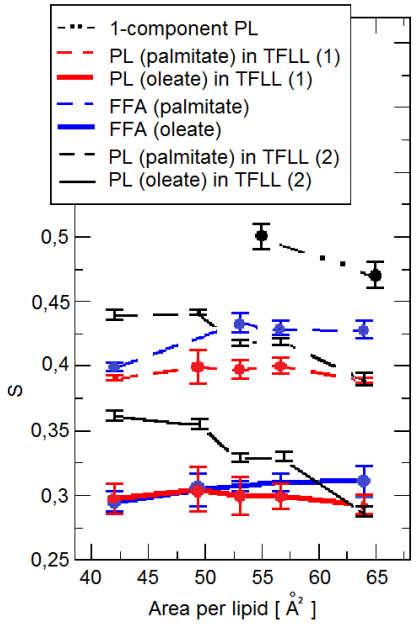

Figure 25.
Order parameter S describing the average conformational order of lipid hydrocarbon chains along the monolayer normal direction [207]. Values for S shown here are averages of all order parameters S_n along the hydrocarbon tail. TFLL (1) stands here for the system where FFA isoleate, and TFLL (2) stands for FFA being palmitate. 1-component PL stands for POPC. Reprinted from Langmuir [207] with co-authors' and publishers permission, copyright 2012 American Chemical Society.

6.3.5 Lateral Diffusion of TG and CE is Quite Different Compared to Diffusion of PL and FFA

A Few Words of MARTINI Parameterization

To investigate the effect of surface area change, and the subsequent effects of lipid chain ordering and layer's conformation changes on lipid diffusion, the diffusion constants in the xy-plane were calculated for each lipid type in the systems. Here we need to note the same limitations as for the previous analyses – the lipid layer does not reside entirely on the xy-plane for higher surface pressures, and thus lipid diffusion in that plane does not fully capture all diffusion in the plane of the lipid layer.

Also we need to note that the diffusion in the coarse grained model is not a target property of the parameterization. MARTINI model is targeted to reproduce primarily only the solubility in different solvents – and that gives justification to our primary finding, which is the separation of TGs to form a separate phase at high surface pressures. The MARTINI model for lipids is also parameterized to reproduce as closely as possible the phase transitions of the lipid tails – i.e. the formation of different liquid-crystalline and fluid phases for the lipid systems [188]. The tail ordering analysis is thus also reliable. However, as not all properties can be targeted at the same time, the diffusion of the particles is more vaguely described. It is known that the lipid molecules in the MARTINI model tend to diffuse approximately four times as fast as lipids in atomistic simulation models. However, the "factor of four" is not entirely true for all particles – the smaller the lipid, the faster it tends to diffuse in MARTINI – the correct correction factor for small lipids may in some cases be more than four [188].

We used a factor of four for all lipids in our system to scale the results to "real diffusion". That is why one needs to keep in mind when interpreting the data that it may be that the smallest of the lipids (the FFAs) show artificially high diffusion, and maybe the biggest molecules (the TGs) show artificially slow diffusion. The qualitative changes in diffusion rates of the lipid types when altering the surface area of the system can be relied on, however, as the trends of the diffusion mainly follow phase separation boundaries, and mirror the effect of lipid tail ordering. Phase separation in response to different stimuli is one of the target properties of MARTINI, and also lipid tail ordering is reasonably well parameterized. The generation of more or less ordered domains, and different kind of organizational structures and lipid phases within the layer is thus well reproduced. Thus, even when the actual value of diffusion is not expected to be quantitatively correct due to the side effects of the coarse grained

method chosen for the simulations, the qualitative changes in the diffusion rates of different components, mirroring the phase separation and lipid tail ordering processes, are reliably reproduced.

Results of Diffusion Analysis – PL vs. TFLL

When lipid diffusion in the pure PL system and the TFLL system are compared (Figure 26), the pure PL system is seen to exhibit very high lateral diffusion values for all surface areas simulated. For pure PL the diffusion rate is even increased when the surface area is diminished. In contrast, in the TFLL layer, diffusion is slowed down at low surface areas. Actually, all lipid components of the TFLL system show this trend of slowing down with smaller surface areas.

However, FFA diffusion is very fast in TFLL systems (though slower than PL diffusion in one-component PL systems at a high surface pressure) and is only slightly influenced by surface pressure. This is not only an effect of the MARTINI parameterization, but also partly due to the assembly of FFA molecules to string-like structures along which FFAs can rapidly diffuse short distances (Figure 26).

The qualitative difference in diffusion rates – increasing diffusion rate for PL, and diminished diffusion rate for TFLL – illustrates the unstable nature of the pure PL layer under high surface pressures. Under similar conditions, pure PL systems have been seen to go through the monolayer–bilayer transition, which is possibly related to vesicle formation [52]. This would be drastic for TFLL, as the vesicles detaching from the lipid layer to the aqueous phase are rapidly recycled via lacrimal ducts, which in turn would lead to dramatic depletion of the TFLL [21]. It seems clear that the neutral lipids of tear film are needed to maintain the integrity of the lipid layer by preventing the monolayer–bilayer transition and subsequent vesicle formation.

Results of Diffusion Analysis – TFLL Components

If we take a look at the diffusion of the individual lipid components of the TFLL system (Figure 26), we see that the lipid diffusion in TFLL slows down for increasing surface pressure in a distinctive way, where all lipid components slow down, but the surface lipids FFA and PL do it for different reasons than the non-surfactants TG and CE. The diffusion of the non-surfactants also slows down significantly more than the diffusion of the surfactants.

The surfactants FFAs and PLs diffuse in the vacuum-water interfacial plane for all interfacial areas. Their diffusion is slowed down by the formation of the more ordered lipid layer structure within the surface layer due to increase in surface pressure. This more ordered layer simply does not allow the lipids to diffuse as fast as in more loosely packed layers. The TGs and CEs, in contrast, diffuse along this surface layer only in systems of large interfacial area. For the smaller interfacial areas, they are pushed away from the interface, and form a separate phase to the air side of the interface. Their diffusion is thus efficiently slowed down by the formation of the aggregate structure – the whole TG-CE aggregate can of course diffuse along the lipid layer, and there can be some diffusion within the aggregate itself, but this diffusion is in nature different than the diffusion in the surface plane. The diffusion of the whole aggregate along the surface is very slow. The CE molecules within the aggregate core show more or less three-dimensional diffusion instead of two-dimensional (data not shown), as they are not located at a surface, but rather inside a sphere. The triglycerides show two-dimensional diffusion on the air side of the interface, but this diffusion is restricted to the dimensions of the aggregate, and is also slow, as the TG tails are entangled in between the CE chains inside the aggregate structure. Also the surface lipid tails intertwine the tails of TG and CE tails, which slows down the diffusion of the surface layer.

Due to this effect, for the large lateral pressures, the CE and TG molecules diffuse slowly, and only within their cluster, while PL and FFA molecules are relatively free to diffuse along the whole water–air interface. This type of "fast diffusion on the surface, and slow diffusion in the core" is consistent with diffusion that takes place in lipid droplets and lipoproteins. Recent simulations of spherical lipid droplet particles have shown [216-217] that lipid diffusion is the fastest at the surface, and slows down considerably as one goes toward the core of the particles. Here we see similar behavior, as with increasing surface pressure the diffusion of the CE and TG molecules slows down significantly more than the diffusion of PL and FFA molecules. Comparison of the diffusion constants in two and three dimensions clearly demonstrates that part of this "slowing down" of the neutral lipids is due to the fact that the diffusion in the core is 3-dimensional, instead of 2-dimensional surface diffusion (data not shown). It is however also clear that the neutral lipid aggregate is much more solid and slow than the planar lipid layer – the triglyceride hydrocarbon tails entangle around the cholesterol ester molecules (and somewhat also the phospholipid tails), making the cluster more viscous, and thus hindering the diffusion in the aggregate.

The present results are consistent with previous simulation results for Langmuir monolayers [228], where one found that the single-particle diffusion coefficient decreases for decreasing area per lipid (increasing surface pressure). Similar trends have also been observed in experiments [229-230].

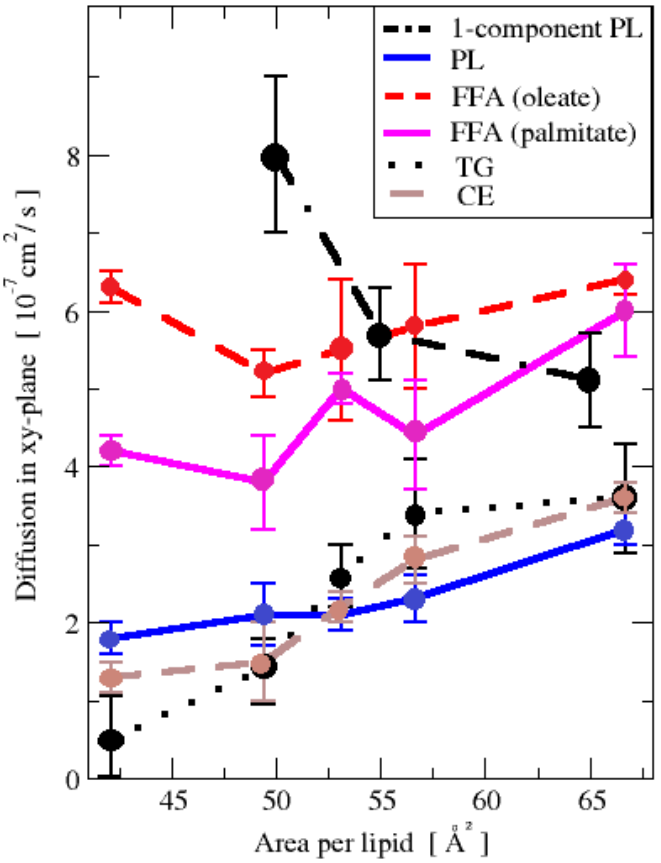

Figure 26. Lateral diffusion coefficients in the plane of the layer [207]. Results are given in units of 10^{-7} cm²/s. Diffusion coefficients reported here have been corrected by dividing the values by 4 to compensate for the faster diffusion in the coarse-grained model compared to atomistic descriptions [188]. 1-component PL stands for POPC. Reprinted from Langmuir [207] with co-authors' and publishers permission, copyright 2012 American Chemical Society.

6.3.6 Studies of Elastic Fluctuations of TFLL Show Protrusions but Not Undulations

Assuming the layer to be aligned in the xy-plane (z being the coordinate along the layer normal), elastic out-of-plane fluctuations of membranes are typically described by the height–height correlation function h(x,y), which describes the deviation of each part of the membrane with respect to the "neutral plane" of the membrane. The neutral plane is the xy-plane, which divides the undulation amplitude in half – half the undulation amplitude is above, half below this neutral plane – the undulation takes place to both sides of this neutral plane. For further discussion on the matter, see Chapter 5.

As mentioned in the previous part of the thesis, the elastic fluctuation spectrum shows two modes. The q^{-2} mode is determined by surface tension of the interface in question and is responsible for short length-scale protrusion modes of one or a few lipids moving locally up and down at the interface. Meanwhile, the q^{-4} mode depends on bending properties of the lipid layer at the interface and describes elastic undulations at length scales much larger than the size of a molecule.

Figure 27 shows that both the one-component PL and the TFLL systems behave in a similar fashion with large areas per lipid, showing only the q^{-2} behavior. The observed q^{-4} modes in both systems can be determined to not to be real undulations, but to arise from the shape change of the layer itself. The folding of the membrane in PL system, and the formation of the lipoprotein-like structure in the TFLL system produces "pseudo-q^{-4} modes" – when the part of the system, which does not lie on the xy-plane is excluded from the analysis, no q^{-4} modes are seen in the results, which concludes that there is no real undulations in the system. The visual inspection of the simulation trajectories supports this result. It is quite possible that the (lateral) system size should be substantially larger to account for large-scale fluctuations in a present-like system characterized by formation of local domains (folded structures and lipoprotein like aggregates). However, that does not necessarily need to hold – the system is not tensionless, but on contrary under a heavy lateral surface pressure – it may be that this trend of no true undulation modes across the interface is promoted by the surface tension in the vacuum-water interface.

For the TFLL system the protrusion modes increase in amplitude when the system is compressed, but show the q^{-2} behavior for all areas per lipid. In the one-component PL system the protrusion mode starts to deviate

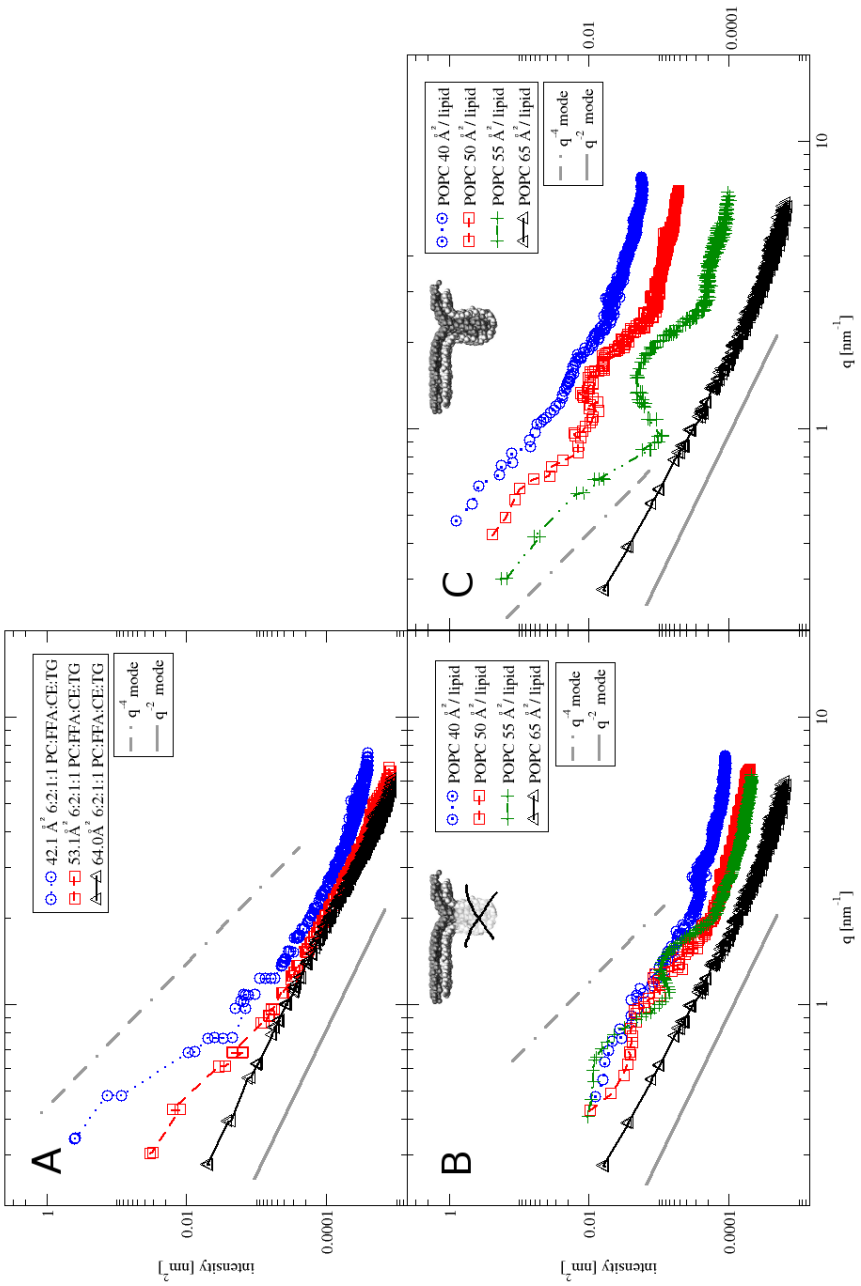

Figure 27. Correlation function for elastic fluctuations at the layer-air interface [207]. (A) Spectrum for the 6:2:1:1 PL/FFA/TG/CE system with PCA as FFA; (B) PL layer, the large layer deformation toward water phase excluded from the results; (C) PL layer, describing the whole system. In each figure, there are also drawn the slopes of the q^{-4} and q^{-2} modes to illustrate the development of the trends of the elastic modes for each system. Reprinted from Langmuir [207] with co-authors' and publishers permission, copyright 2012 American Chemical Society.

from the expected q^{-2} behavior for decreasing area per lipid. We consider this to be due to diffusion along the layer normal direction: diffusion of lipids takes place also inside the engulfment of the lipid layer, thereby affecting the fluctuation spectrum and rendering the interpretation of the spectrum quite complicated. The removal of the folded structure from the q^{-2} mode analysis is more complicated for the PL system than for the TFLL system – the PL structure folds early on in the compression series, and also the folding is much bigger in amplitude – and failure to remove even small parts of this folding leads to major artifacts in q^{-2} mode analysis.

Both elastic modes (the protrusions and undulations) have been observed in freely standing lipid membranes [49, 203], allowing one to determine the bending modulus that modulates the extent of undulations. The protrusion mode [49, 203] can be linked to the corresponding protrusion tension, but its interpretation in terms of a unique elastic property is more difficult [231]. What is clear, however, is that both the TFLL and PL systems show significantly different undulation behavior compared to freely standing bilayers [49, 203].

Further comparison of the simulation data to experiments is more challenging. While the fluctuation spectrum for the different modes allows, in principle, the determination of quantities such as bending modulus, and a term related to tension, we have not done such a comparison in the present work yet. This stems from the fact that, to the candidate's best knowledge, there is no related experimental data (for tear film lipid layers) available for comparison. It is quite possible that this matter will be explored in future studies.

7. Results for the Role of CE and TG in the Tear Film Lipid Layer

The motivation for further simulations after the initial TFLL simulation model was i) to find out the exact role of CE and TG in the TFLL, ii) to find out if lipid head group (PC vs. PE) plays a role in the layer structure, and iii) to find out what happens if PL concentration is too low in the TFLL (the case of blepharitis patients).

Various simulation models were constructed, and from those here will be reviewed the ones, which were most thoroughly analyzed. The systems described in detail are 9:1 CE:PL, 9:1 TG:PL, 8:2 TG:PL, 4:3:3 PL:TG:CE, and pure PL systems. To answer the question whether the PE/PC ratio plays a major role in the layer structure and function, triplicates were formed for each system: one with PC as the PL, another with PE, and a third one having 50:50 PE:PC composition.

Many of these systems were also investigated via Langmuir trough measurements, and one of them also with GIXS and BAM techniques [41,208]. While the candidate has not carried out the experiments, it is yet quite appropriate to present some of the experimental data first, since they will be compared with simulation results presented in the end of this Chapter.

From these systems, all others but the 4:3:3 PC:CE:TG system represent a normal or an almost normal TFLL composition. Meanwhile, the 4:3:3 PC:CE:TG case represents the TFLL composition of blepharitis patients, showing a relatively high ratio of non-surfactant lipids compared to the PL lipids. This case will be discussed separately in more detail.

7.1 Experimental Compression Isotherms

The compression isotherms were obtained via Langmuir trough experiments as described in previous Chapters, covering the surface pressure range from 0 to 40 mN/m.

The two-component PC:TG and PC:CE systems show no clear transitions in the pressure-area isotherm, and only slight hysteresis (Figure 28, on the right). Thus if there are any transitions involved, they seem not to be concerted ones. The three-component 4:4:2 PC:PE:TG system shows no clear transition states either, but the hysteresis is slightly larger for this system [41]. This is quite understandable, as in simulations the PC:PE combination leads to domain formation – the PC and PE lipids separate to different lateral domains in certain areas per lipid in the phase diagram. The larger hysteresis is most probably due to some domain formation events driven by the PC and PE head groups.

In the pressure-area diagram (Figure 28), the 9:1 PC:CE system resides leftmost, showing the smallest area/lipid values for the surface pressure values. This shows how the presence of CE is able to compress the layer to smaller areas. Right next to it, in the original publication, one sees the compression isotherm of the pure PC system, and to the right hand side (on larger areas per lipid) lies the 9:1 and 8:2 PC:TG systems [41]. Thus, the presence of CE in the system seems to shift the PC phase diagram to the left, and the presence of TG seems to shift it to the right, in a concentration dependent manner: the higher the concentration of TG, the more the curve shifts to the right. Also, replacing half of the PC lipids by PE shifts the isotherm of 8:2 PL:TG significantly to the right – showing the importance of the PE head group in the compression of the layer.

The 4:3:3 PC:CE:TG system shows a clear transition [41]. This transition is even a little larger than the one seen for the TFLL (6:2:1:1 PC:FFA:TG:CE) system. This system also shows a very large hysteresis loop, indicating many slowly reversible transitions taking place during the compression-expansion cycle. This system resides for all areas per lipid on the far left side of the other pressure-area isotherms. Especially low areas per lipid are reached after the transition state – at high surface pressures. The transition thus seems to show the formation of a multilayer phase instead of just changing the lipid packing or domain formation within the lipid layer.

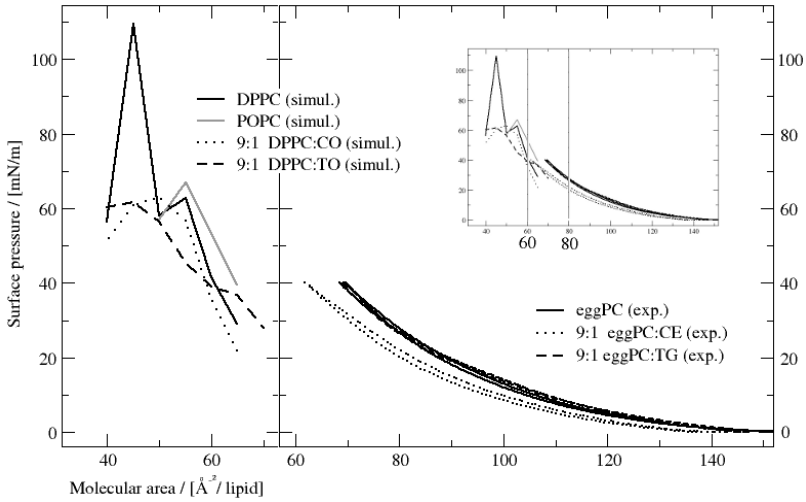

Figure 28. Pressure-area isotherms of the simulations, and Langmuir trough experiments. Comparison of the pressure-area isotherms of simulated DPPC, POPC, DPPC:CO 9:1 and DPPC:TO 9:1 systems [208], and the experimental isotherms of Kulovesi et al. [41]. In the inset, both data has been drawn to the same graph. Error margins are approximately of the same size as the width of the line. With the permission of the original authors.

When the compression isotherms are compared to the simulation results, the agreement is quite good (Figure 28). As the simulated systems are in the limit of reversible compression of the monolayers (see the comparisons of simulations and experiments of this kind by Duncan and Larson [215]), we can only compare the behavior of our largest areas per lipid, to the smallest areas per lipid reached experimentally. This is partially due to the above-mentioned limitations in the MARTINI force field description, which does not allow us to simulate any low surface pressures. All the simulation systems show gas phase formation for areas per lipid larger than 70 Å^2/lipid, as has been reported for other simulation systems, too [51, 215], and for the simulations presented here, the highest area per lipid in liquid phase was 65 Å^2/lipid for DPPC and DPPC:CO 9:1 systems, and 70 Å^2/lipid for the DPPC:TO system. For the 4:3:3 PC:CE:TG system all areas above 50 Å^2/lipid showed gas phase formation.

There are only minute differences between the pressure-area curves between the experimental systems, but even so our simulations reproduce the pressure difference, for the positions in the isotherm we are able to compare our data with (Figure 28). The simulation curves are shifted a little bit left compared to the experimental curves, and that mainly results from the fact that in simulations we used DPPC, while the experiments were made with egg PC, which contains somewhat more unsaturated fatty acids. When comparing our DPPC simulation data with our POPC simulation system, we indeed see the pressure-area curve shifting to the right.

7.2 GIXD and BAM Measurements

From the simulated systems only the blepharitis layer mimicking the composition 4:3:3 PC:CE:TG was investigated via GIXD and BAM [41].

In GIXD, at 20 mN/m, the system was seen to be condensed due to the CE, which gave rise to liquid-ordered domains having a hexagonal packing of 29 Å^2/lipid. These ordered domains were considered rather fluid-like, however, as the molecular area was so high. With this liquid-ordered phase there was noticed co-existence with a gel phase, which consisted mainly of TG molecules. This formation of two phases, an ordered one with TG in it, and another more fluid phase, was also seen in BAM measurements at 20 mN/m. In BAM, there were also some multilayer structures visible, which were interpreted as de-mixed condensed domains produced already during the spreading process.

Comparing these results to the simulation data is not possible, as for this particular system we could not reach anywhere near the 20 mN/m region. In simulations we can capture only multilayer structures for the system. These multilayer structures are presumably present in the experimental systems as well, after the transition seen in the pressure-area isotherm has been completed.

7.3 Simulation Results

7.3.1 Pure PL Systems

In line with the results described in previous Chapters for POPC, the DPPC system used as the pure PC layer in the subsequent simulations formed a monolayer, which folded towards the water phase when the area per lipid became small enough (here 45 Å) (see Figure 29 for snapshots). Some monolayer instability was registered already at areas per lipid of 55–60 Å^2 per lipid, and the folding and collapse of the PC layer were clearly found to emerge at 45 Å^2 per lipid.

Similar trends were reproduced for all PL systems simulated – the POPC [30, 207], DPPC [41,208], DPPE, and 50:50 DPPC:DPPE (data not shown). Changing the lipid head group did not change the behavior of the system significantly – it just shifted the whole isotherm a little bit to the right, leading to layer collapse in a slightly smaller area per lipid value. This was

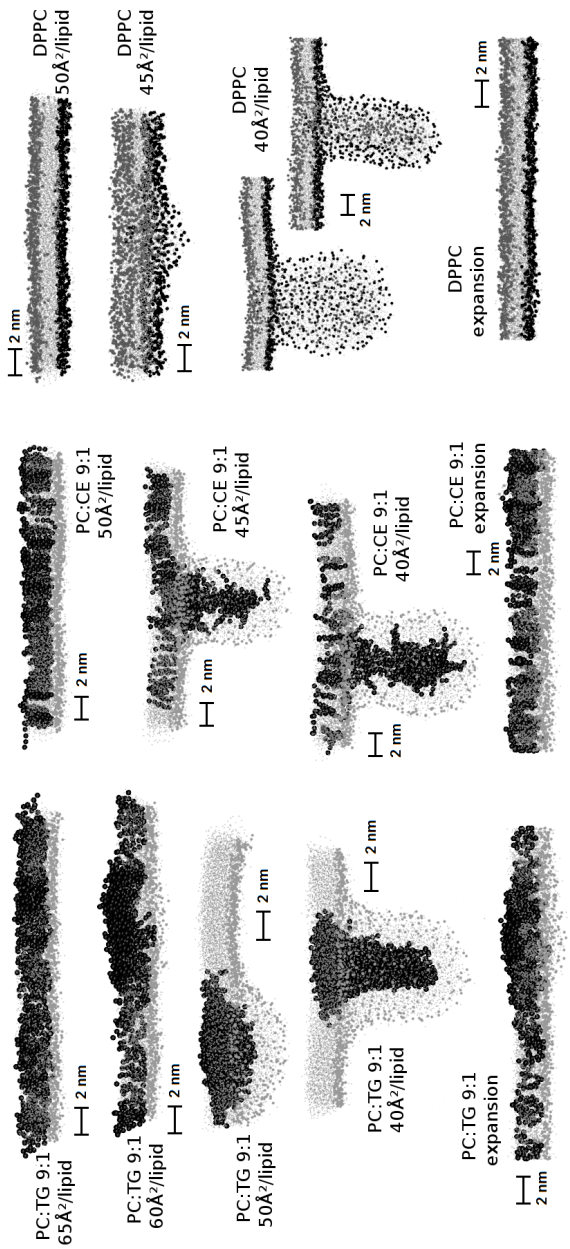

Figure 29. Snapshots of the simulated systems [208]. Water below, and air above the lipid layer. DPPC molecules are grey (big beads represent the PO4 group), and neutral lipids (CO or TO) black. For pure DPPC system (right column) black beads represent the PO4 group, dark grey beads represent the tip of the lipid tail, and light grey all other atoms.

expected, as the PE head group is smaller than the PC head group. The shift was 5 Å^2 at high areas per lipid (when solely PC and solely PE containing systems were compared), gradually getting smaller, and finally vanishing at 45 Å^2, where all PL systems were seen to show closely related, ordered near-collapse structures (for DPPC, see Figure 19). For the surface pressure the difference was approximately 10 mN/m for all data points (between PC and PE systems), showing a maximum of 20 mN/m at 50 Å^2, and completely vanishing at the fully ordered structure at 45 Å^2. The fully saturated DPPC system formed a distinctive lipid condensed phase before collapsing, whereas the POPC containing the double bond in the oleate chain did not show clear hexagonal packing before the collapse and folding into the water phase.

The DPPC simulation results were compared to the previous DPPC monolayer simulations (Figure 19), and the simulations were seen to agree with the previous data [51,215]. As the simulation box volume was fixed in our production simulations, the isotherm reached higher lateral pressures for the near planar-collapse transition structure at 45 Å^2/lipid, than the previous simulations, as the system could not go through the transition and relax to the collapsed state due to the fixed box dimensions. However, the general features of the DPPC pressure-area curve for layer compression were nicely reproduced. In larger areas per lipid, where the system was still in fluid phase, the lipid tails gradually reorganized to a more ordered structure as a response to the increasing stress in the plane of the lipid layer. This gradual ordering of the lipid tails caused that the pressure was not rising steeply at that part of the pressure-area isotherm. These data points reproduced the same trend of gradual surface pressure increase as the two earlier simulations for the same system (Figure 19). After all the lipid tails had transformed to the ordered phase, the surface pressure within the lipid layer increased to a maximum at 45 Å^2/lipid – approximately at the same point as in earlier simulations by Baoukina et al [51], after which the lipid layer collapse was seen, just like in the simulations of Baoukina et al.

7.3.2 Role of Triglycerides in the Phospholipid Monolayers

PC:TG systems showed qualitatively similar behavior as the TFLL system (6:2:1:1 PC:FFA:TG:CE) described earlier [30,41,207-208]. At the large water-vacuum interfacial areas only very few triglycerides had their head groups turned to the air phase of the interface, but with decreasing air-water surface area, all of them gradually flipped to the air side, forming a

cluster, and finally (nano-scale) phase separating from the monolayer, bending the surface layer and forming a “lipoprotein like” particle below the surface PC layer (Figure 29). Both the initiation of the head group flipping to the air side (at ~65 Å^2/lipid and less), and the initiation (at ~60 Å^2/lipid and less) and the completion of the phase separation phenomenon (at ~ 50 Å^2/lipid and less) are dependent on the concentration of TG. For the 8:2 PC:TG system, both of these took place at larger interfacial areas than in the 9:1 PC:TG system. This is expected, as the more there is TG in the system, the more space they take in the interface, and as the interfacial area is diminished, the exclusion of the TG molecules from the interface will begin the earlier the more there are TGs present in the system.

It seems clear that the TG component is needed to initiate the phase separation event in the tear film monolayer. This phase separation results with a surfactant layer on the interface, accompanied with a bulk TG phase on the air side of the surface monolayer. This behavior has been predicted based on experiments [221].

One striking feature of the TG:PC systems is the “smooth collapse” they exert via the ability to expel TG from the monolayer when the surface pressure gets too high. In no step of the phase transition and bulk phase formation the PC lipids get near the liquid-condensed phase – the surface layer of the system stays essentially fluid until all TG has been expelled from the surface layer to the bulk phase (Figure 30). TG thus essentially functions as a buffer against changes in the lateral pressure within the surface lipid layer, maintaining stable conditions for the PL lipids within the layer during increasing or decreasing surface pressure in the air-water interface. Like this the presence of TG lipids in the system affects not only the effective area per lipid for each PL molecule, but also the lipid tail ordering, keeping the layer essentially fluid for a wide range of surface pressures. This also ensures normal diffusion rates in the plane of the lipid layer (data not shown).

7.3.3 Role of Cholesteryl Esters in the Phospholipid Monolayer

The PC/CE (9:1) simulations show qualitatively similar behavior as the pure PC layers [41,208]. However, the presence of CEs compresses the lipid layer. This matches the previously published results for DPPC, and cholesterol containing DPPC layers [51, 224].

At 65 Å^2/lipid, the ester bond regions of CE molecules are exposed to the water phase (see snapshots in Figure 29). When the area per molecule is decreased from 65 to 50 Å^2 per molecule, some CEs are excluded from the

water–lipid interface. Density profiles showed that some of the ester bond beads of CEs flipped from the PC–water interface to the PC–air interface (region near the terminal beads of PC acyl chains).

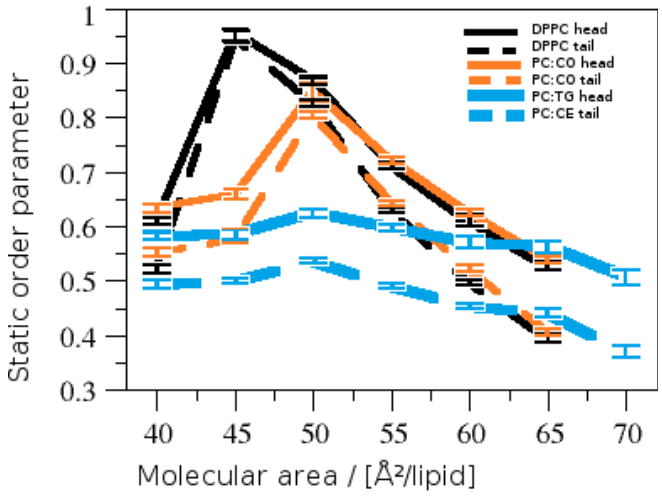

Figure 30. Static order parameters for the PC palmitate chain, in 10:90 TG:PC, 10:90 CE:PC, and 100% PC systems [208]. Order parameters are given along the normal of the lipid layer, for the *sn*-2 palmitate chain of PC. "Tail" denotes the 3 tail-most MARTINI beads (~12 carbon atoms), and "head" denotes the 3 head-most MARTINI beads (out of 16 palmitate tail carbons). Order parameter values range from 1 to 0, where 1 represents a tail resting fully parallel to the lipid layer normal, and 0 represents random orientation with respect to the lipid layer normal. For all systems, only the lipids in the planar lipid layer are taken into account, i.e. lipids participating in folding structures were excluded from the analysis.

In contrast to the TG containing systems, neither CE:PC, nor pure PL systems show a phase separation behavior, where a bulk phase would form to the air side of the monolayer. This result is consistent with the previously published results for DPPC, and cholesterol containing DPPC layers [51, 224], which show no phase separation for cholesterol. This essentially leads the CE:PC system to collapse the same way as pure DPPC layers collapse – the layer organizes to a hexagonally packed, highly ordered, condensed phase structure, which then abruptly collapses to a folded "semi-bilayer" structure, forming long protrusions into the water phase. These kinds of undulations are known to be able to fold back to the planar lipid layer, possibly leading to vesicle detachment from the membrane [52]. Another result could be micelle detachment, if stalk formation or related phenomenon could take place on the connection point of the undulation and the planar lipid layer (Figure 7). However, after the CE:PC layer has folded to the collapsed structure, the CE molecules phase separate between the fold leaflets – and the resulting structure resembles a PC-CE-PC

trilayer. The formation of the trilayer structure may hinder the vesicle formation from the folded structure, but could on the other hand promote CE-filled PC-lipoparticle formation and detachment from the monolayer (Figure 7).

7.3.4 Effect of Changing the PL Head Group

Additional simulations were carried out for other multi-component systems including also PE (such as PE:PC:TG 40:40:20, PE:PC:TG 45:45:10, PC:TG 80:20, and PE:TG 80:20) ([41, 208], data not shown). Their results were consistent with the above and did not provide new insight. All transitions were shifted towards smaller molecular areas, as the PE head group is smaller than the PC head group.

The difference between 100% PC and 100% PE containing TG systems was bigger than the one observed for similar phospholipid systems (Section 7.3.1 above), being 5-10 $Å^2$ for the whole isotherm, and vanishing only at 40 $Å^2$. PE content thus had a stronger effect on compressibility in TG containing systems than in pure PC systems.

7.3.5 Reversible Collapse

We tested if the stage we reach in the collapse – the folding of the PC and PC:CE systems into the water phase, and the formation of the phase separation structure in the PC:TG system – is a reversible or an irreversible process [208]. All the collapse structures we found were reversible in simulations. Even the TG phase separation was essentially reversible, and readily reversed itself spontaneously when the system was exposed to a mildly expanding constant pressure during the simulation. The surface pressures of these collapsed structures are rather high, however – already at the limit where experimental monolayers are not reversible any more [20, 41]. We propose that the collapsed structures we see are actually reversible, but if these deformations are to lead to detachment of vesicles, micelles, or lipoparticles from the continuous lipid surface, the layer could go through an irreversible collapse seen in experiments. Also, as the unfolding of folded structures and insertion of phase separated non-polar lipids back to the monolayer during the layer expansion is a slow process, that could explain some of the hysteresis seen in the experimental pressure-area isotherms for these systems [20, 41, 221].

7.3.6 Composition to Mimic Blepharitis Patients

The 4:3:3 PL:CE:TG system, having only 40% of lipids surfactants, never shows a monolayer structure in the simulations [41] (Figure 31). A stable multilayer structure is seen for low areas per lipid (smaller than 50 Å²/lipid). For systems having area/lipid values larger than 50 Å²/lipid, the lipids form a lipoprotein-like, or tubular particle, where the PLs form the surface, and the TGs and CEs form the core of the particle. The PL lipids do not cover the whole water-vacuum interface in this structure, but only cover the TG and CE lipids, and leave the rest of the interface without any lipid coverage.

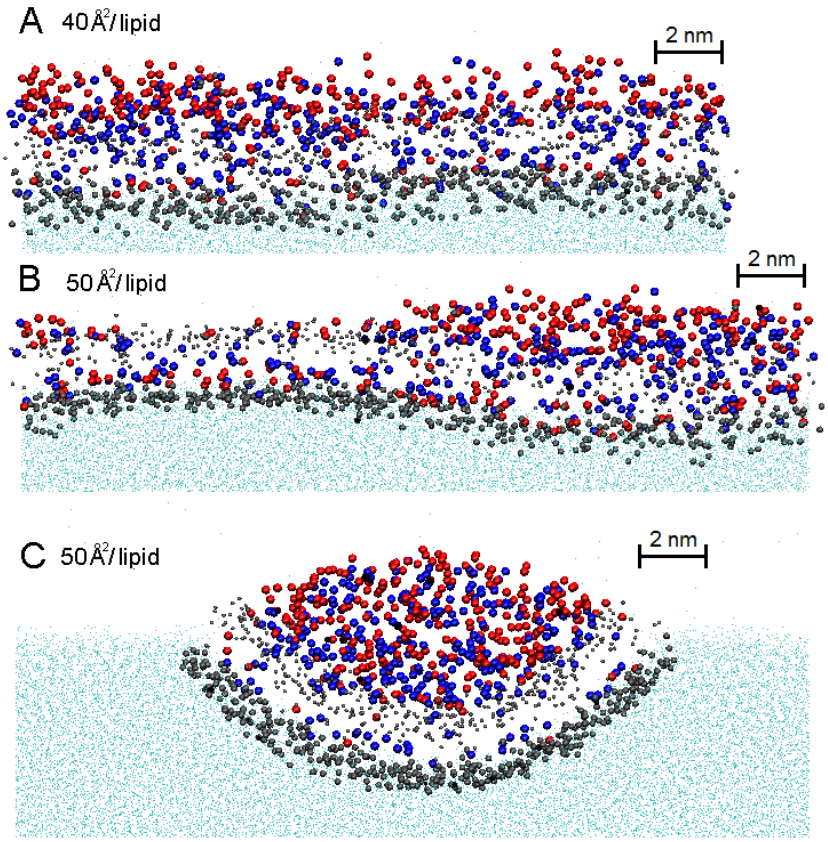

Figure 31. Snapshots for the blepharitis layer [41] with different area per lipid values. Air is above and water below the lipid layer. Colour code for the beads shown in the plots is as follows: PC phosphate (big grey), tips of the PC hydrocarbon tails (small grey), CE ester (blue), TG glycerol (red), and water (light blue mesh). Here, note that in the simulated system there are simultaneously two lipid layers at two air–water interfaces, and panels B and C are snapshots of these two interfaces at the same moment. Reprinted from [41], with the permission of the publisher (copyright holder Soft Matter, RSC Journals 2012), and permission of the co-authors.

The effect of the PL type to the system was investigated by simulating the system with both POPC and DPPC as the PL. The systems behaved essentially the same, however. The only difference was that in the presence of the unsaturated POPC oleate tails, the system shifted the onset of the formation of the tubular / lipoprotein-like structures by ~7 Å^2/lipid towards higher area per lipid values.

The simulation results for the 4:3:3 PL:CE:TG layer clearly demonstrated, why this kind of lipid composition could lead to clinical symptoms – the ability of such compositions to form a continuous surfactant layer to the air-water interface may be severely impaired, and thus lead to aberrations in the vision, and also possibly increased evaporation rate of the aqueous tears from the eye surface.

7.3.7 Comparing the Simulation Systems – the Roles of CE and TG in TFLL

Based on the insight of our simulations, and partly the related experiments, the roles of TG and CE in tear film lipid layers can be summarized as follows.

i) The collapse of the TG containing systems happened via phase separation of the TG lipids, which formed a bulk phase to the vacuum side of the interface. The CO containing and pure PC systems collapsed to a folded structure, exerting steep, bilayer- or trilayer-like structures into the water side of the interface.

ii) The CO containing system's collapsed structure could give rise to lipoparticle detachment from the lipid layer, and the PC collapse structure could lead to either micelle or vesicle detachment from the lipid layer. The TG containing system does not seem to have such a potential for lipid loss into the water phase.

iii) The lateral diffusion in triglyceride containing layers stayed the same for all areas per lipid, whereas for CO containing and pure DPPC systems the diffusion was strongly diminished when the area per lipid was diminished [208].

iv) The CO containing and pure DPPC systems went through a highly ordered, condensed phase structure before collapsing to the folded structure. In the TG containing structure no such lipid phase transition was seen.

These highly ordered structures in CO containing and pure DPPC systems coincided with a high peak in the surface pressure of the system. For the TG containing system, the surface pressure never peaked, but instead stayed rather constant through all simulated areas per lipid.

All these points underline the unique ability of TG to compensate for the effects of surface area change to the lipid system. This could be critical in the tear film lipid layer system – as the system is indeed exposed to a wide range of surface pressures during the blinking of the eye, as the whole layer is pushed towards the eyelids, and then let to expand spontaneously back to the eye surface after the blink.

I would like to conclude that both TG and CE seem to be essential as TFLL components. TG provides the system with an ability to tolerate the various surface pressures the system will be exposed to, and CE on the other hand provides the layer with rigidity and an ordering effect when the system is not under compression or expansion – i.e. between the blinks. These two molecules in the TFLL thus both have their functions in the lipid layer, but the functions they serve are very different from each other.

8. Conclusions and Outlook

The motivation of this study was to understand i) how the physical properties of tear film lipid layers depend on their lipid composition, and ii) whether one could better understand the cause or implications of certain eye diseases based on the lipid compositions in given individuals tear fluid lipid layers. To this end, we have here discussed how coarse-grained molecular dynamics simulations can be used to shed light on some of these issues.

Overall, the present studies show that the collapse behavior of tear film lipid layers varies depending on which lipid molecules (in addition to phospholipids) are present in the layer.

Based on simulations, pure PL systems experienced a steep increase in lateral pressure in definite areas per lipid, and after that the layer formed steep undulations to the water phase [41, 207-208]. These undulations have previously seen to leak lipids to the water phase leading to the collapse of the lipid layer [52].

When adding cholesteryl esters, the DPPC collapse behavior is generally the same as for pure DPPC, although the lipid layer is slightly more ordered. For both pure DPPC and CO-containing DPPC monolayers, large protrusions are formed in response to high lateral pressures [41, 207-208].

In TG:PL systems, no such sudden increase in lateral pressure was seen, and the system underwent a process to a more smooth collapse [30, 41, 207-208].

Finally, the effect of triglycerides thus have two different stabilizing effects: i) to prevent the steep increase in lateral pressure during compression, and ii) to prevent the formation of steep, unstable undulations into the water phase by promoting the formation of triglyceride clusters which bend the lipid layer to form more smooth, lipoparticle-like, undulations instead.

Based on the simulation studies conducted in the Thesis, one can conclude that both TG and CE seem to be essential as TFLL components. TG provides the system with an ability to tolerate the various surface

pressures the system will be exposed to, and CE on the other hand provides the layer with rigidity and an ordering effect.

Altogether, one can conclude that the lipid composition makes a difference, but there is yet a long way to go to understand how the changes in tear film layers' lipid compositions could be used as, e.g., biomarkers for the emergence of eye diseases such as the dry eye syndrome.

Having concluded the main results, let me close this discussion with a brief self-criticism of the work that has been presented in this Thesis. In essence the main question I want to address is how much we can trust the simulation results we have found. Also the value of the results of the Thesis in serving as a foundation for further simulations and experiments is discussed.

8.1 MARTINI Parameters Are Not Well Suited for Air Phase Simulations

MARTINI parameters are not well suited for air phase simulations. The MARTINI parameters used to describe our systems have been determined to match thermodynamic partitioning behavior and phase separation events in fluid-phase biological or soft matter systems – especially in water solutions [188]. In these cases the MARTINI model works very well. However, it is less clear that the MARTINI parameterization would be appropriate for models studied at air-water interfaces. Given this view, we can consider our data in a critical manner. The phase separation of TGs and CEs in response to low surface areas is most probably a real effect. Meanwhile, the results for phases, which form at high surface areas are more questionable. Near the gas phase the lipid tails should interact *preferably* with water molecules, but the MARTINI parameters were not designed to do that, so the lipid tail-water interaction is strongly repulsive in all circumstances [188]. An interesting test would be to mask the water repulsion by adding to the air phase dummy particles, which would show equal repulsion to all particles in the system (mimicking the effect of air) – this should allow the lipid tails settle closer to the water interface in the near-gas-phase structures. This would most probably allow the simulations to overlap more with the experimental Langmuir trough measurements, and would also confirm if that really is the case that the blepharitis patient samples really cannot form a continuous lipid layer on top of the water phase.

8.2 MARTINI Water Molecules Are Not "Water" in the Traditional Sense

MARTINI water molecules are not "water" in the traditional sense. Also, as there has been differing hypotheses, and also contradicting evidence, whether the TFLL prevents water evaporation from tear film or not [30, 31], it would be worthwhile to investigate the system also with atomistic models. MARTINI water has not been designed to "evaporate", but rather to provide a liquid water phase with a constant density [188]. Also, penetration of MARTINI water beads through the lipid layer is highly penalized as each of the beads corresponds to "four water molecules" and insertion of that kind of water amount to a lipid layer is much harder than penetration of a single water molecule to the membrane in atomistic simulations. Also, in atomistic simulations one could use polarizable atoms, which can shift the partial charges inside the molecule, making the waters look "less polar" while penetrating the layer – which is exactly what happens when small molecules penetrate lipid layers. Altogether these points imply that consideration of the penetration of water to TFLL layers is a quite delicate matter, and it is not obvious that such results found by MARTINI would be completely in order.

8.3 It Is Hard to Know, Based on These Simulations Alone, if TFLL is a Monolayer

It is hard to know, based on these simulations alone, if TFLL is a monolayer. Last but not least, there is no consensus that what kind of layer the TFLL actually is – is it a monolayer, multilayer, or if the lipids are in some other phase than the lamellar one [8, 18-26]. There simply is not enough data about the layer yet, and it is hard to know what kind of lipid layer there actually is. So, the starting configuration of the simulations, which was a monolayer-like structure for all systems, may have tweaked the results to show that there indeed "is" a monolayer-like structure, and not some other kind of structure in the interface. The time scales, and more importantly the length scales, were not big enough to allow large-scale phase transition to take place in the systems. Also, there may be proteins incorporated in the lipid layer [15-17].

However, if the TFLL really, or even only partially, does resemble a simple monolayer-like structure, the results of the simulations are in my opinion a

reliable measure of its behavior, when the surface area and the lipid composition of the system are varied. This view is backed up by the fact that the simulation results have been largely consistent with experiments, as the two have been determined in a concerted manner during this thesis project.

8.4 Propositions for Future Work

Finally, let us briefly discuss how the present work could be extended to consider a number of new ideas.

i) *Fine-graining some or all of the systems simulated here through coarse-grained models*. The fine-graining to an atomistic representation would allow one to explore if there are differences in water penetration through the layers. The advantage of this would be that the coarse-grained strucures are already equilibrated and simulated for 1 μs. If significant differences between the lipid compositions would be seen, this would suggest a role of the tear film lipid layer in preventing water evaporation – if not, it would suggest that the role of the tear film lipid layer is more of a mechanical barrier and a lubricant between the eyelid and eye surface during blinking.

ii) *Simulating some systems, especially the ones containing a lot of nonpolar lipids, with "dummy particles" in MARTINI*. If this method would prove to be efficient in preventing artifacts in low surface pressure simulations of monolayer systems, it would enable large scale use of the molecular dynamics software packages also for monolayer simulations. It would also make comparing experimental and simulation results of monolayer studies much more straightforward than it is nowadays.

iii) *Constructing experimental systems* to investigate if the lipid clustering and neutral lipid phase separation in high surface pressures really takes place also in reality for systems having the same lipid composition as the simulated ones. The GIXS measurements done for the systems so far could be complemented with additional sets of measurements in higher surface pressures, if possible. Also, the lipid tail ordering and orientation of the ordered domains could be investigated in Langmuir trough

experiments complemented with Laurdan fluorescence probes, with which one can resolve the order parameter within the layer, as well as the packing orientation of the lipid tails. This depends on, of course, if it indeed would be possible to investigate systems very close to, or even corresponding to, the very collapse surface pressure of the layers.

iv) *Building a tool to analyze simulation data in cases, where the lipid layer is not entirely a planar configuration but is comprised of locally curved regions*. Implementing all commonly used molecular dynamics simulation tools to use this platform – and enabling layer density, RDF distribution, lipid tail ordering, and lipid diffusion analysis within this true (locally curved) lipid layer plane.

v) *Simulating the tear film systems with tear fluid proteins*. The effect of the proteins to the surface properties of the lipid layers is most probably one of the keys into understanding the function and dynamics of the tear film lipid layer. Once the force fields associated with coarse-grained models of proteins have been developed to allow reliable conformation changes (to avoid freezing the protein to a solid object), they would be suitable in simulations of this kind, which most probably need the proteins to show flexibility, as they participate in the formation of a continuous lipid layer structure. Another option would be to simulate this with atomistic models – but that would be very resource demanding, and thus would need to be done in a "grand challenge" project, and still it would probably provide only a partial picture of the interactions between the lipid and protein components of the system. It may thus be better to continue with this part of the project only in a couple of years – the development of the hardware and software is so rapid that within a year or two, these kinds of simulations may very well be feasible.

References

1. Forrester, J.V., A.D. Dick, P.G. McMenamin, and F. Roberts. 2008. The Eye: Basic Sciences in Practice, 3e. Saunders Ltd.

2. Bergmanson, J. 2011. Clinical ocular anatomy and physiology. 18th ed. Texas Eye Research and Technology Center.

3. Remington, L.A. 2011. Clinical Anatomy and Physiology of the Visual System 3e. Butterworth-Heinemann.

4. Pizlo, Z. 2001. Perception viewed as an inverse problem. Vision Research. 41: 3145-3161.

5. Dutton, G.N. 2003. Cognitive vision, its disorders and differential diagnosis in adults and children: knowing where and what things are. Eye (London, England). 17: 289-304.

6. Montés-Micó, R. 2007. Role of the tear film in the optical quality of the human eye. Journal of cataract and refractive surgery. 33: 1631-5.

7. Knop, E., and N. Knop. 2005. The role of eye-associated lymphoid tissue in corneal immune protection. Journal of anatomy. 206: 271-85.

8. Tiffany, J.M. 2008. The normal tear film. Developments in ophthalmology. 41: 1-20.

9. McClellan, K. 1997. Mucosal defense of the outer eye. Survey of ophthalmology. 42.

10. Johnson, M.E., and P.J. Murphy. 2004. Changes in the tear film and ocular surface from dry eye syndrome. Progress in retinal and eye research. 23: 449-74.

11. Ohashi, Y., M. Dogru, and K. Tsubota. 2006. Laboratory findings in tear fluid analysis. Clinica chimica acta; international journal of clinical chemistry. 369: 17-28.

12. Braun, R.J. 2012. Dynamics of the Tear Film. Annual Review of Fluid Mechanics. 44: 267-297.

13. Grus, F., P. Sabuncuo, S. Herberm, and A. Augustin. 2002. Tear-spreading rates: Post-blink. In: Sullivan DA, ME Stern, K Tsubota, DA Dartt, RM Sullivan, et al., editors. Lacrimal gland, tear film and dry eye syndromes 3, Basic Science and Clinical Relevance Part B, Advances in Experimental Medicine and Biology, Vol. 506. Springer. pp. 1201-1205.

14. Abelson, M.B., G.W. Ousler, L.A. Nally, D. Welch, and K. Krenzer. 2002. Alternative reference values for thear film break up time in normal and dry eye populations. In: Sullivan DA, ME Stern, K Tsubota, DA Dartt, RM Sullivan, et al.,

editors. Lacrimal gland, tear film and dry eye syndromes 3, Basic Science and Clinical Relevance Part B, Advances in Experimental Medicine and Biology, Vol. 506. Springer. pp. 1121-1125.

15. McNamara, N., and C. Basbaum. 2002. Mucins : Origin, properties, regulation and function. In: Sullivan DA, ME Stern, K Tsubota, DA Dartt, RM Sullivan, et al., editors. Lacrimal gland, tear film and dry eye syndromes 3, Basic Science and Clinical Relevance Part B, Advances in Experimental Medicine and Biology, Vol. 506. Springer. pp. 269-363.

16. Zhou, L., S.Z. Zhao, S.K. Koh, L. Chen, C. Vaz, et al. 2012. In-depth analysis of the human tear proteome. Journal of proteomics. 75: 3877-85.

17. Tragoulias, S.T., P.J. Anderton, G.R. Dennis, F. Miano, and T.J. Millar. 2005. Surface pressure measurements of human tears and individual tear film components indicate that proteins are major contributors to the surface pressure. Cornea. 24: 189-200.

18. Bron, a. J., J.M. Tiffany, S.M. Gouveia, N. Yokoi, and L.W. Voon. 2004. Functional aspects of the tear film lipid layer. Experimental Eye Research. 78: 347-360.

19. Chetty, E., and W.D.H. Gillan. 2008. Reviewing the tear film ' s lipid layer. 67: 155-159.

20. Mudgil, P., and T.J. Millar. 2011. Surfactant properties of human meibomian lipids. Investigative ophthalmology & visual science. 52: 1661-70.

21. Khanal, S., and T.J. Millar. 2010. Nanoscale phase dynamics of the normal tear film. Nanomedicine : nanotechnology, biology, and medicine. 6: 707-13.

22. King-Smith, P.E., B. a Fink, R.M. Hill, K.W. Koelling, and J.M. Tiffany. 2004. The thickness of the tear film. Current eye research. 29: 357-68.

23. Foulks, G.N. 2007. The correlation between the tear film lipid layer and dry eye disease. Survey of ophthalmology. 52: 369-74.

24. Butovich, I. a. 2009. The Meibomian puzzle: combining pieces together. Progress in retinal and eye research. 28: 483-98.

25. Butovich, I. a. 2011. Lipidomics of human Meibomian gland secretions: Chemistry, biophysics, and physiological role of Meibomian lipids. Progress in lipid research. 50: 278-301.

26. Rantamäki, A.H., T. Seppänen-Laakso, M. Oresic, M. Jauhiainen, and J.M. Holopainen. 2011. Human tear fluid lipidome: from composition to function. PloS one. 6: e19553.

28. McCulley, J.P., and W.E. Shine. 2001. The lipid layer: the outer surface of the ocular surface tear film. Bioscience reports. 21: 407-18.

29. Smith, E.C., J.M. Crane, T.G. Laderas, and S.B. Hall. 2003. Metastability of a supercompressed fluid monolayer. Biophysical journal. 85:3048-57.

30. Kulovesi, P., J. Telenius, A. Koivuniemi, G. Brezesinski, A. Rantamäki, et al. 2010. Molecular organization of the tear fluid lipid layer. Biophysical journal. 99: 2559-67.

31. Rantamäki, A.H., M. Javanainen, I. Vattulainen, and J.M. Holopainen. 2012. Do lipids retard the evaporation of the tear fluid? Investigative ophthalmology & visual science. 53: 6442-7.

32. Borchman, D., G.N. Foulks, M.C. Yappert, J. Mathews, K. Leake, et al. 2009. Factors affecting evaporation rates of tear film components measured in vitro. Eye & contact lens. 35: 32-7.

33. King-Smith, P.E., B. a Fink, J.J. Nichols, K.K. Nichols, R.J. Braun, et al. 2009. The contribution of lipid layer movement to tear film thinning and breakup. Investigative ophthalmology & visual science. 50: 2747-56.

34. Rolando, M., and M. Zierhut. 2001. The ocular surface and tear film and their dysfunction in dry eye disease. Survey of ophthalmology. 45 Suppl 2: S203-10.

36. Nagyová, B., and J.M. Tiffany. 1999. Components responsible for the surface tension of human tears. Current eye research. 19: 4-11.

37. Miano, F., M.G. Mazzone, A. Giannetto, V. Enea, P. McCauley, et al. 2002. Interface properties of simplified tear-like fluids in relation to lipid and aqueous layer composition. In: Sullivan DA, ME Stern, K Tsubota, DA Dartt, RM Sullivan, et al., editors. Lacrimal gland, tear film and dry eye syndromes 3, Basic Science and Clinical Relevance Part B, Advances in Experimental Medicine and Biology, Vol. 506. Springer. pp. 405-417.

40. Goto, E., K. Endo, A. Suzuki, Y. Fujikura, Y. Matsumoto, et al. 2003. Tear evaporation dynamics in normal subjects and subjects with obstructive meibomian gland dysfunction. Investigative ophthalmology & visual science. 44: 533-9.

41. Kulovesi, P., J. Telenius, A. Koivuniemi, G. Brezesinski, I. Vattulainen, et al. 2012. The impact of lipid composition on the stability of the tear fluid lipid layer. Soft Matter. 8: 5826.

42. Aydemir, E., C.J.W. Breward, and T.P. Witelski. 2011. The effect of polar lipids on tear film dynamics. Bulletin of mathematical biology. 73: 1171-201.

43. Petrov, P.G., J.M. Thompson, I.B.A. Rahman, R.E. Ellis, E.M. Green, et al. 2007. Two-dimensional order in mammalian pre-ocular tear film. Experimental eye research. 84: 1140-6.

44. Georgiev, G.A., E. Kutsarova, a Jordanova, R. Krastev, and Z. Lalchev. 2010. Interactions of Meibomian gland secretion with polar lipids in Langmuir monolayers. Colloids and surfaces. B, Biointerfaces. 78: 317-27.

45. Rantamäki, A.H., J. Telenius, A. Koivuniemi, I. Vattulainen, and J.M. Holopainen. 2011. Lessons from the biophysics of interfaces: lung surfactant and tear fluid. Progress in retinal and eye research. 30: 204-15.

46. McCulley, J., and W. Shine. 1997. A compositional based model for the tear film lipid layer. Transactions of the American Opthalmology Society. 95: 79–93

47. Bernardes, T.F., and A.A. Bonfioli. 2010. Blepharitis. Seminars in ophthalmology. 25: 79-83.

48. Dartt, D.A. 2011. Tear Lipocalin: structure and Function. The Ocular Surface. 9: 126-138.

49. Lindahl, E., and O. Edholm. 2000. Mesoscopic undulations and thickness fluctuations in lipid bilayers from molecular dynamics simulations. Biophysical journal. 79: 426-33.

50. Pocivavsek, L., R. Dellsy, A. Kern, S. Johnson, B. Lin, et al. 2008. Stress and fold localization in thin elastic membranes. Science (New York, N.Y.). 320: 912-6.

51. Baoukina, S., L. Monticelli, S.J. Marrink, and D.P. Tieleman. 2007. Pressure-area isotherm of a lipid monolayer from molecular dynamics simulations. Langmuir : the ACS journal of surfaces and colloids. 23: 12617-23.

52. Baoukina, S., L. Monticelli, H.J. Risselada, S.J. Marrink, and D.P. Tieleman. 2008. The molecular mechanism of lipid monolayer collapse. Proceedings of the National Academy of Sciences of the United States of America. 105: 10803-8.

53. Lemp, M. a. 2008. Advances in understanding and managing dry eye disease. American journal of ophthalmology. 146: 350-356.

54. Brewitt, H., and F. Sistani. 2001. Dry eye disease: the scale of the problem. Survey of ophthalmology. 45 Suppl 2: S199-202.

55. McGinnigle, S., S. a Naroo, and F. Eperjesi. 2012. Evaluation of dry eye. Survey of ophthalmology. 57: 293-316.

56. Perry, H.D. 2008. Dry eye disease: pathophysiology, classification, and diagnosis. The American journal of managed care. 14: S79-87.

57. Tsubota, K. 1998. Tear dynamics and dry eye. Progress in retinal and eye research. 17.

60. Rosenthal, P., and D. Borsook. 2012. The corneal pain system. Part I: the missing piece of the dry eye puzzle. The ocular surface. 10: 2-14.

61. Himebaugh, N., L. Thibos, C. Begley, A. Bradley, and G. Wilson. 2002. Predicting optical effects of tear film break up on retinal image quality using the Shack-Hartmann aberrometer and computational optical modeling. In: Sullivan DA, ME Stern, K Tsubota, DA Dartt, RM Sullivan, et al., editors. Lacrimal gland, tear film and dry eye syndromes 3, Basic Science and Clinical Relevance Part B, Advances in Experimental Medicine and Biology, Vol. 506. Springer. pp. 1141-1147.

62. Wilson, S., R. Mohan, J.-W. Hong, J.-S. Lee, R. Choi, et al. 2002. Apoptosis in the cornea in response to epithelial injury : Significance to wound healing and dry eye. In: Sullivan DA, ME Stern, K Tsubota, DA Dartt, RM Sullivan, et al., editors. Lacrimal gland, tear film and dry eye syndromes 3, Basic Science and Clinical Relevance Part B, Advances in Experimental Medicine and Biology, Vol. 506. Springer. pp. 821-826.

63. Ousler, G., M. Abelson, L. Nally, D. Welch, and J. Casavant. 2002. Evaluation of the time to “natural compensation” in normal and dry eye subject populations during exposure to a controlled adverse environment. In: Sullivan DA, ME Stern, K Tsubota, DA Dartt, RM Sullivan, et al., editors. Lacrimal gland, tear film and dry eye syndromes 3, Basic Science and Clinical Relevance Part B, Advances in Experimental Medicine and Biology, Vol. 506. Springer. pp. 1057-1063.

64. Calonge, M., A. Enríquez-de-Salamanca, Y. Diebold, M.J. González-García, R. Reinoso, et al. 2010. Dry eye disease as an inflammatory disorder. Ocular immunology and inflammation. 18: 244-53.

65. Beuerman, R.W., and M.E. Stern. 2005. Neurogenic inflammation: a first line of defense for the ocular surface. The ocular surface. 3: S203-6.

66. Bron, A.J., N. Yokoi, E. Gaffney, and J.M. Tiffany. 2009. Predicted Phenotypes of Dry Eye: Proposed Consequences of Its Natural History. The Ocular Surface. 7: 78-92.

67. Sullivan, R., J. Cermak, A. Papas, M. Dana, and D. Sullivan. 2002. Economic and quality of life impact of dry eye symptoms in women with Sjögren's syndrome. In: Sullivan R, J Cermak, A Papas, M Dana, D Sullivan, editors. Lacrimal gland, tear film and dry eye syndromes 3, Basic Science and Clinical Relevance Part B, Advances in Experimental Medicine and Biology, Vol. 506. Springer. pp. 1183-1188.

68. Shimazaki, J., E. Goto, M. Ono, S. Shimmura, and K. Tsubota. 1998. Meibomian Gland Dysfunction in Patients with Sjogren Syndrome. : 1485-1488.

69. Nguyen, C.Q., and A.B. Peck. 2009. Unraveling the Pathophysiology of Sjogren Syndrome-Associated Dry Eye Disease. The Ocular Surface. 7: 11-27.

70. Akpek, E.K., K.B. Lindsley, R.S. Adyanthaya, R. Swamy, A.N. Baer, et al. 2011. Treatment of Sjögren's syndrome-associated dry eye an evidence-based review. Ophthalmology. 118: 1242-52.

71. Akpek, E.K., A. Klimava, J.E. Thorne, D. Martin, K. Lekhanont, et al. 2009. Evaluation of patients with dry eye for presence of underlying Sjögren syndrome. Cornea. 28: 493-7.

72. Sullivan, B.D. 2000. Impact of Antiandrogen Treatment on the Fatty Acid Profile of Neutral Lipids in Human Meibomian Gland Secretions. Journal of Clinical Endocrinology & Metabolism. 85: 4866-4873.

73. Krenzer, K.L. 2000. Effect of Androgen Deficiency on the Human Meibomian Gland and Ocular Surface. Journal of Clinical Endocrinology & Metabolism. 85: 4874-4882.

74. Gupta, P.D., K. Johar, K. Nagpal, and a R. Vasavada. 2005. Sex hormone receptors in the human eye. Survey of ophthalmology. 50: 274-84.

75. Ma, L., and X.-M. Lin. 2010. Effects of lutein and zeaxanthin on aspects of eye health. Journal of the science of food and agriculture. 90: 2-12.

76. He, J., and H.E.P. Bazan. Omega-3 fatty acids in dry eye and corneal nerve regeneration after refractive surgery. Prostaglandins, leukotrienes, and essential fatty acids. 82: 319-25.

77. Roncone, M., H. Bartlett, and F. Eperjesi. 2010. Essential fatty acids for dry eye: A review. Contact lens & anterior eye : the journal of the British Contact Lens Association. 33: 49-54; quiz 100.

78. Kalt, W., A. Hanneken, P. Milbury, and F. Tremblay. 2010. Recent research on polyphenolics in vision and eye health. Journal of agricultural and food chemistry. 58: 4001-7.

79. Rand, A.L., and N. York. 2012. Nutritional supplements for dry eye syndrome. 22: 279-282.

80. Pflugfelder, S.C. 2008. Prevalence, burden, and pharmacoeconomics of dry eye disease. The American journal of managed care. 14: S102-6.

81. Klein, B., and R. Klein. 2007. Lifestyle exposures and eye diseases in adults. American journal of ophthalmology. 144: 961-969.

82. Rosenfield, M. 2011. Computer vision syndrome: a review of ocular causes and potential treatments. Ophthalmic & physiological optics : the journal of the British College of Ophthalmic Opticians (Optometrists). 31: 502-15.

83. Yao, W., R.S. Davidson, V.D. Durairaj, and C.D. Gelston. 2011. Dry eye syndrome: an update in office management. The American journal of medicine. 124: 1016-8.

84. Foulks, G.N. 2003. What is Dry Eye and What Does It Mean to the Contact Lens Wearer ? 29: 96-100.

85. Mcculley, J.P., and W.E. Shine. 2003. Eyelid Disorders : The Meibomian Gland , Blepharitis , and Contact Lenses. 29: 2002-2004.

86. Lemp, M. a, and L. Bielory. 2008. Contact lenses and associated anterior segment disorders: dry eye disease, blepharitis, and allergy. Immunology and allergy clinics of North America. 28: 105-17, vi-vii.

87. Panaser, A., and B.J. Tighe. 2012. Function of lipids – their fate in contact lens wear: an interpretive review. Contact lens & anterior eye : the journal of the British Contact Lens Association. 35: 100-11.

88. Ramamoorthy, P., and J.J. Nichols. 2008. Mucins in contact lens wear and dry eye conditions. Optometry and vision science : official publication of the American Academy of Optometry. 85: 631-42.

89. Fonn, D. 2009. Dryness with contact lenses and dry eye: are they the same or different? Eye & contact lens. 35: 219.

90. Sindt, C.W., and R.A. Longmuir. 2007. Contact lens strategies for the patient with dry eye. The ocular surface. 5: 294-307.

91. Dartt, D.A. 2009. Neural regulation of lacrimal gland secretory processes: relevance in dry eye diseases. Progress in retinal and eye research. 28: 155-77.

92. Stern, M.E., R.W. Beuerman, R.I. Fox, J. Gao, A.K. Mircheff, et al. 1998. The pathology of dry eye: the interaction between the ocular surface and lacrimal glands. Cornea. 17: 584-9.

93. Joffre, C., M. Souchier, S. Grégoire, S. Viau, L. Bretillon, et al. 2008. Differences in meibomian fatty acid composition in patients with meibomian gland dysfunction and aqueous-deficient dry eye. The British journal of ophthalmology. 92: 116-9.

94. Calonge, M. 2001. The Treatment of Dry Eye Tear Substitution : Artificial Tear. 45.

95. Dogru, M., and K. Tsubota. 2011. Pharmacotherapy of dry eye. Expert opinion on pharmacotherapy. 12: 325-34.

96. Doughty, M.J., and S. Glavin. 2009. Efficacy of different dry eye treatments with artificial tears or ocular lubricants: a systematic review. Ophthalmic & physiological optics : the journal of the British College of Ophthalmic Opticians (Optometrists). 29: 573-83.

97. Rauz, S., and V.P. Saw. 2010. Serum eye drops, amniotic membrane and limbal epithelial stem cells--tools in the treatment of ocular surface disease. Cell and tissue banking. 11: 13-27.

98. Ding, J., and D. a Sullivan. 2012. Aging and dry eye disease. Experimental gerontology. 47: 483-90.

99. Berke, A. 2002. Blinking frequency and the thickness of the lipid layer. In: Sullivan DA, ME Stern, K Tsubota, DA Dartt, RM Sullivan, et al., editors. Lacrimal gland, tear film and dry eye syndromes 3, Basic Science and Clinical Relevance Part

B, Advances in Experimental Medicine and Biology, Vol. 506. Springer. pp. 513-516.

100. Tan, M., G. Demirci, D. Pearce, I. Jalbert, P. Sankaridurg, et al. 2002. Contact lens-induced papillary conjunctivitis is associated with increased deposits of extended wear hydrogel lenses. In: Sullivan DA, ME Stern, K Tsubota, DA Dartt, RM Sullivan, et al., editors. Lacrimal gland, tear film and dry eye syndromes 3, Basic Science and Clinical Relevance Part B, Advances in Experimental Medicine and Biology, Vol. 506. Springer. pp. 951-955.

101. Langtangen, H.P. 2009. Python Scripting for Computational Science (Texts in Computational Science and Engineering). Springer.

102. Berendsen , H.J.C. 2007. Simulating the Physical World: Hierarchical Modeling from Quantum Mechanics to Fluid Dynamics. Cambridge University Press .

103. Donner, L.J., and W.G. Large. 2008. Climate Modeling. Annual Review of Environment and Resources. 33: 1-17.

104. Krishnamurti, T.N. 1995. Numerical Weather Prediction. Annual Review of Fluid Mechanics. 27: 195-225.

105. Coveney, P.V., and P.W. Fowler. 2005. Modelling biological complexity: a physical scientist's perspective. Journal of the Royal Society, Interface / the Royal Society. 2: 267-80.

106. Hölttä-Vuori, M., R.-L. Uronen, J. Repakova, E. Salonen, I. Vattulainen, et al. 2008. BODIPY-cholesterol: a new tool to visualize sterol trafficking in living cells and organisms. Traffic (Copenhagen, Denmark). 9: 1839-49.

107. Hoefling, M., N. Lima, D. Haenni, C. a M. Seidel, B. Schuler, et al. 2011. Structural heterogeneity and quantitative FRET efficiency distributions of polyprolines through a hybrid atomistic simulation and Monte Carlo approach. PloS one. 6: e19791.

108. Loura, L.M.S., and J.P.P. Ramalho. 2011. Recent developments in molecular dynamics simulations of fluorescent membrane probes. Molecules (Basel, Switzerland). 16: 5437-52.

109. López Cascales, J.J., M.L. Huertas, and J. García de la Torre. 1997. Molecular dynamics simulation of a dye molecule in the interior of a bilayer: 1,6-diphenyl-1,3,5-hexatriene in dipalmitoylphosphatidylcholine. Biophysical chemistry. 69: 1-8.

110. Vaiana, A.C., H. Neuweiler, A. Schulz, J. Wolfrum, M. Sauer, et al. 2003. Fluorescence quenching of dyes by tryptophan: interactions at atomic detail from combination of experiment and computer simulation. Journal of the American Chemical Society. 125: 14564-72.

111. Wong-Ekkabut, J., Z. Xu, W. Triampo, I.-M. Tang, D.P. Tieleman, et al. 2007. Effect of lipid peroxidation on the properties of lipid bilayers: a molecular dynamics study. Biophysical journal. 93: 4225-36.

112. Khandelia, H., and O.G. Mouritsen. 2009. Lipid gymnastics: evidence of complete acyl chain reversal in oxidized phospholipids from molecular simulations. Biophysical journal. 96: 2734-43.

113. Jurkiewicz, P., L. Cwiklik, P. Jungwirth, and M. Hof. 2012. Lipid hydration and mobility: an interplay between fluorescence solvent relaxation experiments and molecular dynamics simulations. Biochimie. 94: 26-32.

114. Alonso, H., A.A. Bliznyuk, and J.E. Gready. 2006. Combining docking and molecular dynamic simulations in drug design. Medicinal research reviews. 26: 531-68.

115. Li, Y., and T. Hou. 2010. Computational Simulation of Drug Delivery at Molecular Level. Current Medicinal Chemistry. 17: 10.

116. Ferrer, S., J. Ruiz-Pernía, S. Martí, V. Moliner, I. Tuñón, et al. 2011. Hybrid schemes based on quantum mechanics/molecular mechanics simulations goals to success, problems, and perspectives. Advances in protein chemistry and structural biology. 85: 81-142.

117. Broglia, R. a, G. Tiana, and D. Provasi. 2004. Simple models of protein folding and of non-conventional drug design. Journal of Physics: Condensed Matter. 16: R111-R144.

118. Feller, S.E., and R.W. Pastor. 1996. On simulating lipid bilayers with an applied surface tension: periodic boundary conditions and undulations. Biophysical journal. 71: 1350-5.

119. Salditt, T. 2005. Thermal fluctuations and stability of solid-supported lipid membranes. Journal of Physics: Condensed Matter. 17: R287-R314.

120. Siegel, A.P., N.F. Hussain, M. Johnson, and C.A. Naumann. 2012. Metric between buckling structures and elastic properties in physisorbed polymer-tethered lipid monolayers. Soft Matter. 8: 5873.

121. Lingwood, D., and K. Simons. 2010. Lipid rafts as a membrane-organizing principle. Science (New York, N.Y.). 327: 46-50.

122. Fan, J., M. Sammalkorpi, and M. Haataja. 2010. Influence of nonequilibrium lipid transport, membrane compartmentalization, and membrane proteins on the lateral organization of the plasma membrane. Physical Review E. 81: 011908.

123. Elson, E.L., E. Fried, J.E. Dolbow, and G.M. Genin. 2010. Phase separation in biological membranes: integration of theory and experiment. Annual review of biophysics. 39: 207-26.

124. Leslie, M. 2011. Mysteries of the cell. Do lipid rafts exist? Science (New York, N.Y.). 334: 1046-7.

125. Niemelä, P.S., M.T. Hyvönen, and I. Vattulainen. 2009. Atom-scale molecular interactions in lipid raft mixtures. Biochimica et biophysica acta. 1788: 122-35.

126. Leach, A. 2001. Molecular Modelling: Principles and Applications (2nd Edition). Prentice Hall.

127. Jensen, F. 2007. Introduction to computational chemistry. Wiley.

128. Becker, O.M., A.D. MacKerell, B. Roux, and M. Watanabe, editors. 2001. Computational Biochemistry and Biophysics. CRC Press.

129. Schlick, T. 2002. Molecular Modeling and Simulation: An Interdisciplinary Guide (Interdisciplinary Applied Mathematics). Springer.

130. Schwartz, R. 2008. Biological Modeling and Simulation: A Survey of Practical Models, Algorithms, and Numerical Methods (Computational Molecular Biology). The MIT Press.

131. Van Der Spoel, D., E. Lindahl, B. Hess, G. Groenhof, A.E. Mark, et al. 2005. GROMACS: fast, flexible, and free. Journal of computational chemistry. 26: 1701-18.

132. Hess, B., S.- Uppsala, and E. Lindahl. 2008. GROMACS 4 : Algorithms for Highly Efficient , Load-Balanced , and Scalable Molecular Simulation. : 435-447.

133. Phillips, J.C., R. Braun, W. Wang, J. Gumbart, E. Tajkhorshid, et al. 2005. Scalable molecular dynamics with NAMD. Journal of computational chemistry. 26: 1781-802.

134. Case, D.A., T.E. Cheatham, T. Darden, H. Gohlke, R. Luo, et al. 2005. The Amber biomolecular simulation programs. Journal of computational chemistry. 26: 1668-88.

135. Brooks, B.R., C.L. Brooks, A.D. Mackerell, L. Nilsson, R.J. Petrella, et al. 2009. CHARMM: the biomolecular simulation program. Journal of computational chemistry. 30: 1545-614.

136. Fetter, A.L., J.D. Walecka, and Physics. 2003. Theoretical Mechanics of Particles and Continua (Dover Books on Physics). Dover Publications.

137. Landau, L.D., and E.M. Lifshitz. 1976. Mechanics, Third Edition: Volume 1 (Course of Theoretical Physics). Butterworth-Heinemann.

138. Hess, B., C. Kutzner, D. van der Spoel, and E. Lindahl. GROMACS 4, manual. ftp://ftp.gromacs.org/pub/manual . Link tested 21. 10. 2013.

139. Callen, H.B. 1985. Thermodynamics and an Introduction to Thermostatistics. Wiley.

140. Reichl, L.E. 2009. A Modern Course in Statistical Physics. Wiley-VCH.

141. Safran, S. 2003. Statistical Thermodynamics Of Surfaces, Interfaces, And Membranes (Frontiers in Physics). Westview Press.

142. Atkins, P., and J. de Paula. 2009. Physical Chemistry. W. H. Freeman.

143. Verlet, L. 1967. Computer “Experiments” on Classical Fluids. I. Thermodynamical Properties of Lennard-Jones Molecules. Physical Review. 159: 98-103.

144. Hockney, R. 1970. The potential calculation and some applications. Methods in Computational Physics. 9. 135-211.

145. Berendsen, H.J.C., J.P.M. Postma, W.F. van Gunsteren, A. DiNola, and J.R. Haak. 1984. Molecular dynamics with coupling to an external bath. The Journal of Chemical Physics. 81: 3684.

146. Nosé, S. 1984. A unified formulation of the constant temperature molecular dynamics methods. The Journal of Chemical Physics1. 81: 511-519.

147. Nosé, S. 1984. A molecular dynamics method for simulations in the canonical ensemble. Molecular Physics. 52: 255-268.

148. Hoover, W. 1985. Canonical dynamics: Equilibrium phase-space distributions. Physical review. A. 31: 1695-1697.

149. Bussi, G., D. Donadio, and M. Parrinello. 2007. Canonical sampling through velocity rescaling. The Journal of chemical physics. 126: 014101.

150. Parrinello, M. 1981. Polymorphic transitions in single crystals: A new molecular dynamics method. Journal of Applied Physics. 52: 7182.

151. Nosé, S., and M.L. Klein. 1983. Constant pressure molecular dynamics for molecular systems. Molecular Physics. 50: 1055-1076.

152. Ryckaert, J.-P., G. Ciccotti, and H.J.C. Berendsen. 1977. Numerical integration of the cartesian equations of motion of a system with constraints: molecular dynamics of n-alkanes. Journal of Computational Physics. 23: 327-341.

153. Miyamoto, S., and P.A. Kollman. 1992. Settle: An analytical version of the SHAKE and RATTLE algorithm for rigid water models. Journal of Computational Chemistry. 13: 952-962.

154. Hess, B., H. Bekker, H.J.C. Berendsen, and J.G.E.M. Fraaije. 1997. LINCS: A linear constraint solver for molecular simulations. Journal of Computational Chemistry. 18: 1463-1472.

155. Hess, B. 2008. P-LINCS: A Parallel Linear Constraint Solver for Molecular Simulation. Journal of Chemical Theory and Computation. 4: 116-122.

158. de Vries, A.H., I. Chandrasekhar, W.F. van Gunsteren, and P.H. Hünenberger. 2005. Molecular dynamics simulations of phospholipid bilayers: Influence of artificial periodicity, system size, and simulation time. The journal of physical chemistry. B. 109: 11643-52.

159. Baştuğ, T., S.M. Patra, and S. Kuyucak. 2006. Finite system and periodicity effects in free energy simulations of membrane proteins. Chemical Physics Letters. 425: 320-323.

160. Knecht, V., and S.-J. Marrink. 2007. Molecular dynamics simulations of lipid vesicle fusion in atomic detail. Biophysical journal. 92: 4254-61.

161. Sagui, C., and T.A. Darden. 1999. Molecular dynamics simulations of biomolecules: long-range electrostatic effects. Annual review of biophysics and biomolecular structure. 28: 155-79.

162. Karttunen, M., J. Rottler, I. Vattulainen, and C. Sagui. 2008. Electrostatics in biomolecular simulations: Where are we now and where are we heading? In: Feller S, editor. Computational Modeling of Membrane Bilayers. Academic Press. pp. 49-89.

163. Kastenholz, M.A., and P.H. Hünenberger. 2004. Influence of Artificial Periodicity and Ionic Strength in Molecular Dynamics Simulations of Charged Biomolecules Employing Lattice-Sum Methods. The Journal of Physical Chemistry B. 108: 774-788.

164. Bergdorf, M., C. Peter, and P.H. Hünenberger. 2003. Influence of cut-off truncation and artificial periodicity of electrostatic interactions in molecular simulations of solvated ions: A continuum electrostatics study. The Journal of Chemical Physics. 119: 9129.

165. Darden, T., D. York, and L. Pedersen. 1993. Particle mesh Ewald: An N·log(N) method for Ewald sums in large systems. The Journal of Chemical Physics. 98: 10089.

166. Essmann, U., L. Perera, M.L. Berkowitz, T. Darden, H. Lee, et al. 1995. A smooth particle mesh Ewald method. The Journal of Chemical Physics. 103: 8577.

167. Hou, C., and W. Ge. 2012. A novel mode and its verification of parallel molecular dynamics simulation sith the coupling of GPU and CPU. International Journal of Modern Physics C. 23: 1250015.

168. Ruymgaart, A.P., A.E. Cardenas, and R. Elber. 2011. MOIL-opt: Energy-Conserving Molecular Dynamics on a GPU/CPU system. Journal of chemical theory and computation. 7: 3072-3082.

169. Sanbonmatsu, K.Y., and C.-S. Tung. 2007. High performance computing in biology: multimillion atom simulations of nanoscale systems. Journal of structural biology. 157: 470-80.

170. Harvey, M.J., and G. De Fabritiis. 2012. A survey of computational molecular science using graphics processing units. Wiley Interdisciplinary Reviews: Computational Molecular Science. 2: 734-742.

171. Hansson, T., C. Oostenbrink, and W. van Gunsteren. 2002. Molecular dynamics simulations. Current opinion in structural biology. 12: 190-6.

172. Larsson, P., B. Hess, and E. Lindahl. 2011. Algorithm improvements for molecular dynamics simulations. Wiley Interdisciplinary Reviews: Computational Molecular Science. 1: 93-108.

173. Berendsen, H.J.C., D. van der Spoel, and R. van Drunen. 1995. GROMACS: A message-passing parallel molecular dynamics implementation. Computer Physics Communications. 91: 43-56.

174. Mackerell, A.D. 2004. Empirical force fields for biological macromolecules: overview and issues. Journal of computational chemistry. 25: 1584-604.

175. van Gunsteren, W.F., D. Bakowies, R. Baron, I. Chandrasekhar, M. Christen, et al. 2006. Biomolecular modeling: Goals, problems, perspectives. Angewandte Chemie (International ed. in English). 45: 4064-92.

176. Klauda, J.B., R.M. Venable, and R.W. Pastor. Considerations for Lipid Force Field Development. In: Feller SE, editor. Computational Modeling of Membrane Bilayers, Current Topics in Membranes, Vol 60. Elsevier.

177. Jorgensen, W.L., and J. Tirado-Rives. 2005. Potential energy functions for atomic-level simulations of water and organic and biomolecular systems. Proceedings of the National Academy of Sciences of the United States of America. 102: 6665-70.

178. Brooks, B.R., R.E. Bruccoleri, B.D. Olafson, D.J. States, S. Swaminathan, et al. 1983. CHARMM: A program for macromolecular energy, minimization, and dynamics calculations. Journal of Computational Chemistry. 4: 187-217.

179. MacKerell,, A.D., D. Bashford, R.L. Dunbrack,, J.D. Evanseck, M.J. Field, et al. 1998. All-Atom Empirical Potential for Molecular Modeling and Dynamics Studies of Proteins. The Journal of Physical Chemistry B. 102: 3586-3616.

180. The Nobel Prize in Chemistry 2013. Nobelprize.org. Nobel Media AB 2013. http://www.nobelprize.org/nobel_prizes/chemistry/laureates/2013/. Link tested 21 Oct 2013.

181. Weiner, P.K., and P.A. Kollman. 1981. AMBER: Assisted model building with energy refinement. A general program for modeling molecules and their interactions. Journal of Computational Chemistry. 2: 287-303.

182. Cornell, W.D., P. Cieplak, C.I. Bayly, I.R. Gould, K.M. Merz, et al. 1995. A Second Generation Force Field for the Simulation of Proteins, Nucleic Acids, and Organic Molecules. Journal of the American Chemical Society. 117: 5179-5197.

183. Jorgensen, W.L., and J. Tirado-Rives. 1988. The OPLS [optimized potentials for liquid simulations] potential functions for proteins, energy minimizations for crystals of cyclic peptides and crambin. Journal of the American Chemical Society. 110: 1657-1666.

184. Jorgensen, W.L., D.S. Maxwell, and J. Tirado-Rives. 1996. Development and Testing of the OPLS All-Atom Force Field on Conformational Energetics and Properties of Organic Liquids. Journal of the American Chemical Society. 118: 11225-11236.

185. Hermans, J., H.J.C. Berendsen, W.F. Van Gunsteren, and J.P.M. Postma. 1984. A consistent empirical potential for water-protein interactions. Biopolymers. 23: 1513-1518.

187. Poger, D., W.F. Van Gunsteren, and A.E. Mark. 2010. A new force field for simulating phosphatidylcholine bilayers. Journal of computational chemistry. 31: 1117-25.

188. Marrink, S.J., H.J. Risselada, S. Yefimov, D.P. Tieleman, and A.H. de Vries. 2007. The MARTINI force field: coarse grained model for biomolecular simulations. The journal of physical chemistry. B. 111: 7812-24.

189. Berger, O., O. Edholm, and F. Jähnig. 1997. Molecular dynamics simulations of a fluid bilayer of dipalmitoylphosphatidylcholine at full hydration, constant pressure, and constant temperature. Biophysical journal. 72: 2002-13.

190. Khandelia, H., and E. Salonen. Unpublished results.

191. Pasenkiewicz-Gierula, M., T. Róg, K. Kitamura, and A. Kusumi. 2000. Cholesterol effects on the phosphatidylcholine bilayer polar region: a molecular simulation study. Biophysical journal. 78: 1376-89.

192. Shillcock, J.C., and R. Lipowsky. 2002. Equilibrium structure and lateral stress distribution of amphiphilic bilayers from dissipative particle dynamics simulations. The Journal of Chemical Physics. 117: 5048.

193. Kamerlin, S.C.L., S. Vicatos, A. Dryga, and A. Warshel. 2011. Coarse-grained (multiscale) simulations in studies of biophysical and chemical systems. Annual review of physical chemistry. 62: 41-64.

194. de Pablo, J.J. 2011. Coarse-grained simulations of macromolecules: from DNA to nanocomposites. Annual review of physical chemistry. 62: 555-74.

195. Bennun, S.V., M.I. Hoopes, C. Xing, and R. Faller. 2009. Coarse-grained modeling of lipids. Chemistry and physics of lipids. 159: 59-66.

196. Riniker, S., J.R. Allison, and W.F. van Gunsteren. 2012. On developing coarse-grained models for biomolecular simulation: a review. Physical chemistry chemical physics : PCCP. 14: 12423-30.

197. Hyeon, C., and D. Thirumalai. 2011. Capturing the essence of folding and functions of biomolecules using coarse-grained models. Nature communications. 2: 487.

198. Clementi, C. 2008. Coarse-grained models of protein folding: toy models or predictive tools? Current opinion in structural biology. 18: 10-5.

199. Bereau, T., and M. Deserno. 2009. Generic coarse-grained model for protein folding and aggregation. The Journal of chemical physics. 130: 235106.

200. Hall, A. 2011. Computational modelling of triglycerides in lipoproteins and glycolipids in lipid rafts. Tampere University of Technology.

201. Wang, Z.-J., and M. Deserno. 2010. Systematic implicit solvent coarse-graining of bilayer membranes: lipid and phase transferability of the force field. New journal of physics. 12.

202. Bond, H.S. 1996. What ' s So Great about Nothing ? The GNU General Public License and the Zero-Price-Fixing Problem II . A Price of Nothing on Subsequent Distributions. 08: 547-572.

203. Niemelä, P.S., S. Ollila, M.T. Hyvönen, M. Karttunen, and I. Vattulainen. 2007. Assessing the nature of lipid raft membranes. PLoS computational biology. 3: e34.

204. Als-Nielsen, J., and D. McMorrow. 2011. Elements of Modern X-ray Physics. Wiley.

206. Imparato, a, J.C. Shillcock, and R. Lipowsky. 2005. Shape fluctuations and elastic properties of two-component bilayer membranes. Europhysics Letters (EPL). 69: 650-656.

207. Telenius, J., A. Koivuniemi, P. Kulovesi, J.M. Holopainen, and I. Vattulainen. 2012. Role of neutral lipids in tear fluid lipid layer: coarse-grained simulation study. Langmuir : the ACS journal of surfaces and colloids. 28: 17092-100.

208. Telenius, J., A. Koivuniemi, J. Holopainen, and I. Vattulainen. Smooth collapse of a lipid monolayer – MD simulation study about the art of blinking the eyes. unpublished manuscript.

209. Koivuniemi, A., M. Heikelä, P.T. Kovanen, I. Vattulainen, and M.T. Hyvönen. 2009. Atomistic simulations of phosphatidylcholines and cholesteryl esters in high-density lipoprotein-sized lipid droplet and trilayer: clues to cholesteryl ester transport and storage. Biophysical journal. 96: 4099-108.

210. Murtola, T., T. Róg, E. Falck, M. Karttunen, and I. Vattulainen. 2006. Transient Ordered Domains in Single-Component Phospholipid Bilayers. Physical Review Letters. 97: 238102.

211. Humphrey, W., A. Dalke, and K. Schulten. 1996. VMD: visual molecular dynamics. Journal of molecular graphics. 14: 33-8, 27-8.

212. GIMP, Freeware GNU image manipulation program. http://docs.gimp.org/en/ . Link tested 21. 10. 2013.

213. Grace, a WYSIWYG 2D plotting tool for the X Window System. http://plasma-gate.weizmann.ac.il/Grace/doc/UsersGuide.html . Link tested 21. 10. 2013.

214. Lucas, T.R., B.A. Bauer, J.E. Davis, and S. Patel. 2012. Molecular dynamics simulation of hydrated DPPC monolayers using charge equilibration force fields. Journal of computational chemistry. 33: 141-52.

215. Duncan, S.L., and R.G. Larson. 2008. Comparing experimental and simulated pressure-area isotherms for DPPC. Biophysical journal. 94: 2965-86.

216. Murtola, T., T.A. Vuorela, M.T. Hyvönen, S.-J. Marrink, M. Karttunen, et al. 2011. Low density lipoprotein: structure, dynamics, and interactions of apoB-100 with lipids. Soft Matter. 7: 8135.

217. Vuorela, T., A. Catte, P.S. Niemelä, A. Hall, M.T. Hyvönen, et al. 2010. Role of lipids in spheroidal high density lipoproteins. PLoS computational biology. 6: e1000964.

218. Catte, A., J.C. Patterson, D. Bashtovyy, M.K. Jones, F. Gu, et al. 2008. Structure of spheroidal HDL particles revealed by combined atomistic and coarse-grained simulations. Biophysical journal. 94: 2306-19.

219. Khandelia, H., L. Duelund, K.I. Pakkanen, and J.H. Ipsen. 2010. Triglyceride blisters in lipid bilayers: implications for lipid droplet biogenesis and the mobile lipid signal in cancer cell membranes. PloS one. 5: e12811.

220. Henneré, G., P. Prognon, F. Brion, and I. Nicolis. 2009. Molecular dynamics study of a phospholipid monolayer at a water/triglyceride interface: towards lipid emulsion modelling. Chemistry and physics of lipids. 157: 86-93.

221. Mitsche, M.A., L. Wang, and D.M. Small. 2010. Adsorption of egg phosphatidylcholine to an air/water and triolein/water bubble interface: use of the 2-dimensional phase rule to estimate the surface composition of a phospholipid/triolein/water surface as a function of surface pressure. The journal of physical chemistry. B. 114: 3276-84.

222. Kwong, C.N., R.E. Heikkila, and D.G. Cornwell. 1971. Properties of cholesteryl esters in pure and mixed monolayers. Journal of lipid research. 12: 31-5.

223. Bonn, M., S. Roke, O. Berg, A. Stamouli, and M. Müller. 2004. A Molecular View of Cholesterol-Induced Condensation in a Lipid Monolayer. The Journal of Physical Chemistry B. 108: 19083-19085.

224. Laing, C., S. Baoukina, and D.P. Tieleman. 2009. Molecular dynamics study of the effect of cholesterol on the properties of lipid monolayers at low surface tensions. Physical chemistry chemical physics : PCCP. 11: 1916-22.

225. Tuckermann, R., S. Bauerecker, and H.K. Cammenga. 2007. The generation of octadecanol monolayers on acoustically levitated water drops. Colloids and Surfaces A: Physicochemical and Engineering Aspects. 309: 198-201.

226. Zdravkova, A.N., and J.P.J.M. van der Eerden. 2007. Structure and Stability of Triglyceride Monolayers on Water and Mica Surfaces. Crystal Growth & Design. 7: 2778-2787.

227. Murtola, T., E. Falck, M. Patra, M. Karttunen, and I. Vattulainen. 2004. Coarse-grained model for phospholipid/cholesterol bilayer. The Journal of chemical physics. 121: 9156-65.

228. Javanainen, M., L. Monticelli, J. Bernardino de la Serna, and I. Vattulainen. 2010. Free volume theory applied to lateral diffusion in Langmuir monolayers: atomistic simulations for a protein-free model of lung surfactant. Langmuir : the ACS journal of surfaces and colloids. 26: 15436-44.

229. Caruso, F., F. Grieser, P.J. Thistlethwaite, and M. Almgren. 1993. Two-dimensional diffusion of amphiphiles in phospholipid monolayers at the air-water interface. Biophysical journal. 65: 2493-503.

230. Denicourt, N., P. Tancrède, M. Brullemans, and J. Teissié. 1989. The liquid condensed diffusional transition of dipalmitoylphosphoglycerocholine in monolayers. Biophysical chemistry. 33: 63-70.

231. Brandt, E.G., A.R. Braun, J.N. Sachs, J.F. Nagle, and O. Edholm. 2011. Interpretation of fluctuation spectra in lipid bilayer simulations. Biophysical journal. 100: 2104-11.

Appendix A

Deriving Law of Coulomb from Maxwell's Equations and Force of Lorenz

To be able to represent the interaction between charged particles, we need to derive the law of Coulomb from the Maxwell's equations and the force of Lorenz, which are the basic fundamental principles of electrostatics – they are like the "Newtonian equations of electrostatics". These laws explain how charges and electricity-related phenomena work in our world. As the laws of Newton, also these laws are amazingly simple.

When constructing the concept of "atomic charge", we can approximate the atom as a sphere, having a point charge at the center of the sphere. Now the charge of the atom can be described by a uniform charge distribution on the surface of the sphere.

According to Maxwell's equations for linearly behaving materials, the point charge induces a charge density ρ to it surroundings, and this charge density creates an electric field **E** around the particle. The flux density of the electric field describes the strength of the electric force:

$$\textit{electric flux density} = \nabla \bullet \mathbf{E} = \frac{\rho}{\varepsilon} \qquad \textbf{(1A)}$$

The flux density is dependent on the electric permittivity ε of the media surrounding the point charge. For electrically inert materials like air ε is close to the permittivity of vacuum ε_o. Here below we assume this to hold true.

This can be stated in an integral form, describing the electric flux through a surface *S* around the point charge:

$$electric\ flux = \oint_S \mathbf{E} \bullet d\mathbf{A} = \frac{Q}{\varepsilon_0} \qquad \textbf{(2A)}$$

Here the infitesimal area unit ***dA*** feels the effect of the electric field **E**, and this "electric flux over infitesimal area" is integrated over the whole surface area *S*. Here *Q* is the charge of the point charge, and *S* is the surface area of a selected sphere around the point charge. We now define that the surface is spherical, and that the point charge is located in the center of this sphere – we essentially create a spherically symmetric charge distribution over which we are integrating. And, as we were integrating over such a spherical surface, having the point charge in the center, we can write the surface integral as a volume integral in spherical coordinates and realize that this integral is actually constant over any sphere having the point charge *Q* in the origin. Now the total flux through each of these spherical surfaces *S* stays the same, even though the charge density diminishes when moving away from the point charge.

We can see that the integrand can be written also as a constant volume integral :

$$\oint_S \mathbf{E} \bullet d\mathbf{A} = \int_0^r \int_0^{2\pi} \int_0^{\pi} ERsin(R)dRd\theta d\phi = 4\pi r^2 E = \frac{Q}{\varepsilon_0} \qquad \textbf{(3A)}$$

where *R* is the radial distance from the point charge, and *r,θ,Φ* are the spherical coordinate axes (point charge in the origo of the coordinate system).

From this integral one can solve **E**:

$$\mathbf{E} = \frac{Q}{\varepsilon_0 4\pi r^2} \frac{\mathbf{r}}{|\mathbf{r}|} \qquad \textbf{(4A)}$$

Here we have made *E* to be a vector again by giving it direction **r** along the spherical coordinate from the point charge (radius **r** of any *Q*-centered sphere). Now we can use the law of Lorenz force to find that

$$\mathbf{F} = \mathbf{E}q + \mathbf{v} \times \mathbf{B} \qquad \textbf{(5A)}$$

Where *q* is the charge, and **v** the velocity of the particle. We note that the magnetic field ***B*** is absent in our system as the charge of the systems stays

constant and the point charge moves slowly enough not to induce any magnetic fields. This results to the absence of magnetic field **B,** and equation 5A takes the form $\mathbf{F} = \mathbf{E}q$, and we reach

$$\mathbf{F} = \frac{q_1 q_2}{\varepsilon_0 4\pi r^2} \frac{\mathbf{r}}{|\mathbf{r}|} \qquad \textbf{(6A)}$$

which tells us the magnitude of a force between charged particles, having charges of q_1 and q_2, when separated by distance $r = |\mathbf{r}|$. Here we assumed low charge density (permittivity close to ε_o), no fast movement of charged particles, and also that all charges are constant.

Appendix B

Derivation of the Most Probable Distribution

In molecular dynamics one is to set the initial kinetic energy distribution of atoms and molecules in the MD system to resemble as probable state of the system as possible. To find out the most probable microstate, which can be used as a starting configuration for the kinetic energies, let us consider a system having a constant total energy, and constant number of molecules. This is the so-called microcanonical ensemble, or the *NVE* ensemble. Now, the energies of single molecules need to sum up to the total energy of the system at all times. Now focusing on distinguishable particles, the molecules spread to the possible energy states *i* like this:

$$\sum_i N_i E_i = E \qquad \textbf{(1B)}$$

where N_i is the number of molecules having the energy state *i*, E is the total energy of the system, and E_i is the discrete energy of the i^{th} energy state.

Our aim here is to find an expression for N_i at equilibrium.

There are many ways the molecules can be distributed among the energy states E_i, and still reproduce the same total energy E. We wish to investigate only that energy distribution which is the most probable one – the microstate, which can be "formed from the substrates the most ways".

We can start searching for this most probable microstate by defining a formula for the weight (W) of the configuration:

$$W = \frac{N!}{N_1!\, N_2! \ldots N_i!} \qquad \textbf{(2B)}$$

Here N is the number of ways to assign the particles over the energy levels. For simplicity, we assume degeneracy of one for all energy levels (meaning that all particles reside on different, i.e. *distinguishable* energy levels).

The higher the W, i.e. the more ways there are to form a given configuration, the more probable the state is. The most probable configuration can thus be found by searching for the maximum of W. We can now write

$$\ln(W) = \ln\left(\frac{N!}{N_1!\, N_2! \ldots N_i!}\right) = \ln N! - \sum_i \ln N_i! \qquad \textbf{(3B)}$$

Next, before moving on, we can realize that in our *NVE* ensemble there are conditions

$$\sum_i \mathrm{d}N_i = 0 \qquad \textbf{(4B)}$$

for fixed N, and

$$\sum_i E_i \mathrm{d}N_i = 0 \qquad \textbf{(5B)}$$

for fixed E. Now based on these we can introduce the constraints

$$\alpha \sum_i \mathrm{d}N_i = 0 \qquad \textbf{(6B)}$$

and

$$\beta \sum_i E_i \mathrm{d}N_i = 0 \qquad \textbf{(7B)}$$

with some parameters α and β.

Now, as our total energy and the number of molecules are constant, and each molecule is always on one of the allowed energy levels, we reach (using the Stirling's approximation for the factorial):

$$\begin{aligned} \mathrm{d}\ln W &\approx -\sum_i \ln(N_i)\ \mathrm{d}N_i \\ &= -\sum_i \left(\ln(N_i) + \beta E_i + \alpha\right)\ \mathrm{d}N_i = 0 \end{aligned} \qquad \textbf{(8B)}$$

This implies that now we get

$$\ln(N_i) + \beta E_i + \alpha = 0 \quad \Leftrightarrow \quad \ln(N_i) = -\beta E_i - \alpha \tag{9B}$$

and then

$$N_i = e^{-\beta E_i - \alpha} \tag{10B}$$

Consequently

$$N = \sum_i N_i = \sum_i e^{-\beta E_i} e^{-\alpha} = e^{-\alpha} \sum_i e^{-\beta E_i} \tag{11B}$$

Now, we define the partition function *Q*:

$$\sum_i e^{-\beta E_i} = Q = \textit{ partition function} \tag{12B}$$

which allows us to eliminate α from the equation by noting that $e^{-\alpha} = \frac{N}{Q}$,

which allows us to express the occupation level for each energy level:

$$N_i = \frac{N}{Q}\ e^{-\beta E_i} \tag{13B}$$

That is, the distribution of particle number in state *i* follows the Boltzmann distribution. The identification of β as the Boltzmann factor is shown in Appendix D.

If we normalize this (to get weights w_i for states n_i, and assign them such that the sum of all states will be 1), we get

$$w_i = \frac{N_i}{N} \tag{14B}$$

We reach:

$$w_i = \frac{1}{Q} e^{-\beta E_i} \tag{15B}$$

Now the expectation value of the energy, the thermodynamic internal energy (*U*) is constant:

$$U = \sum_i w_i E_i \qquad \textbf{(16B)}$$

where the weights w_i sum up to one (normalized weights), and each molecule of the system is always in one of the states i.

The weights w_i can be readily used to determine the distribution of kinetic energies of atoms and molecules of our MD system. In Appendix D it is shown, how this distribuition is used to create the preferred simulation temperature for the system.

Appendix C

Definition of Entropy

Entropy is a thermodynamic entity, which provides a measure for the accessible different microstates of the system.

Let us first define entropy, S, for the microcanonical ensemble:

$$S = k_B \log \Omega(U) \tag{1C}$$

where $\Omega(U)$ is the number of different microstates on a tiny range of energies $\mathrm{d}U$, and k_B is Boltzmann's constant. $\Omega(U)$ thus tells us how many different microstates we can create in the tiny energy range. That is, in how many different ways we can construct the system with that total energy E from the individual molecular energies E_i. That depends on how many different values (or small energy ranges) j are available (the total molecular energy range available in that state) and also how many molecules there are in each energy state. The number of different combinations available in the current state of the system is then $\Omega(U)$.

If we wish to formulate an equation for the change of entropy (when the system moves from state a to state b), we get:

$$\mathrm{d}S = \mathrm{d}\left(k_B \log \Omega(U)\right) \tag{2C}$$

$$\int \mathrm{d}S = \int_a^b \mathrm{d}\left(k_B \log \Omega(U)\right) \tag{3C}$$

$$\Delta S = k_B \left(\log(\Omega_b) - \log(\Omega_a)\right) = k_B \log \frac{\Omega_b}{\Omega_a} \tag{4C}$$

We see that the change in entropy is a logarithm of the relative change in the number of different microstates. So, as entropy is higher, more states

are available for molecules. An increase in entropy means an increase in energy state configurations, i.e. microstates, available for the system. The ratio of the new and old available microstates gives rise to the change in entropy.

We can compare this result to the fundamental equation of thermodynamics, which relates the change in system's internal energy U when only heat q is added to the system, at constant temperature:

$$\mathrm{d}U = \mathrm{d}q = T\mathrm{d}S \qquad \textbf{(5C)}$$

We see that the change in entropy is linear with respect to the amount of heat added. If we think about the microstates, then we can see that the number of available microstates increases exponentially. Even a slight increase in heat increases the number of available microstates quite tremendously.

So, to get entropy change linearly in respect to the added heat, we need to take a logarithm from the relative change of the number of different microstates, and define entropy with that.

Appendix D

Boltzmann's Constant and Distribution

In Appendix B we described the most probable distribution, and in Appendix C we defined the thermodynamic quantity *entropy*. Here we combine those two to reach the Boltzmann's constant and distribution, which link the molecular configuration space to the simulation temperature, providing means to estimate and set up starting configurations for simulation systems.

D-1 Boltzmann's Constant

In Appendix B we reached the relative occupancy, the normalized weights w_i , for each energy level E_i in the system :

$$w_i = \frac{1}{Q} e^{-\beta E_i} \qquad \textbf{(15B)}$$

where Q is the partition function. (We assumed degeneragy level of 1 for all states, i.e. *distinguishable* particles).

We saw that the expectation value of the energy, the thermodynamic internal energy (U) is constant:

$$U = \sum_i w_i E_i \qquad \textbf{(16B)}$$

where the weights w_i sum up to one (normalized weights), and each molecule of the system is always in one of the states i.

To be able to determine the factor β, we need to formulate the fundamental equation of thermodynamics also in the context of the energy configuration space.

Based on formula 16B, we already know that we can formulate the change in internal energy, when only heat is added to the *NVE* system:

$$\mathrm{d}U = \mathrm{d}q = \mathrm{d}\sum_i w_i E_i = \sum_i E_i \mathrm{d}w_i \qquad \textbf{(1D)}$$

In practice we have now shifted to the *NVT* ensemble, the so-called canonical ensemble, where instead of total energy we hold temperature constant by adding and subtracting heat q from the system to maintain constant temperature.

Now we can rewrite this with the use of formula 15B, to yield (for a detailed derivation see Berendsen et al. [102]):

$$\mathrm{d}U = \mathrm{d}q = \sum_i E_i \mathrm{d}w_i = \sum_i \left(-\beta^{-1} \ln w_i - \beta^{-1} \ln Q\right) \mathrm{d}w_i = -\beta^{-1} \sum_i \ln w_i \mathrm{d}w_i \qquad \textbf{(2D)}$$

If we now compare the resulting formula:

$$\mathrm{d}q = \left(\frac{1}{\beta}\right) \mathrm{d}\left(-\sum_i w_i \ln w_i\right) \qquad \textbf{(3D)}$$

to the fundamental equation in thermodynamics:

$$\mathrm{d}U = \mathrm{d}q = T\mathrm{d}S \qquad \textbf{(4D)}$$

which links the change in internal energy to temperature T and entropy S, we can see that

$$\frac{1}{\beta} \propto T \qquad \textbf{(5D)}$$

and

$$-\mathrm{d}\left(\sum_i w_i \ln w_i\right) \propto S \qquad \textbf{(6D)}$$

And, scaling this to fit other SI system units, we reach a conclusion that the factor β, needed to couple the energy distribution to the temperature T of the system, is $(k_B T)^{-1}$, where the constant k_B (Boltzmann's constant) is needed to express the constant β as a molar, not molecular, quantity.

D-2 Boltzmann's Distribution – Providing the Kinetic Energy Values for MD Simulation

Now we have reached a formula suitable to set kinetic energy values (the velocities) for the molecules of our MD system's starting configuration:

$$U = \frac{1}{Q}\sum_i E_i e^{-\beta E_i} \qquad \textbf{(7D)}$$

where $\beta = 1/k_B T$.

We can modify this formula so that we can calculate the most probable distribution for the molecular kinetic energies.

This distribution is known as the Boltzmann distribution:

$$w_i = \frac{N_i}{N} = g_i \frac{1}{Q}\sum_i E_i e^{-\beta E_i} \qquad \textbf{(8D)}$$

and it gives the fractions of molecules N in energy states E_i. Here we have also taken into account the degeneracy g of each state i , generalizing the formula for all configurational states – also the energetically indistinguishable ones.

By setting the velocities of the molecules of the system so that the kinetic energy distribution follows the Bolzmann's distribution, one can reach a reasonably good approximation for the starting configuration of the MD system. In practice one just starts the *NVT* simulation with this setup, monitors the kinetic energy values, and if needed, corrects or scales the velocities of the molecules to reach a constant temperature and an equilibrated system during the simulation run. After equilibration the system can then be ran longer, and the gathered data can be used to investigate the biological properties of the system.

Appendix E

Details of Experimental Studies

Compression Isotherm Experiments

Concerning Section 6.1 about experiments for compression isotherms, let us briefly discuss the experimental setups. The compression isotherms were measured for the PL and TFLL systems by Langmuir trough (see Figure 20). The experiment is constructed so that the lipid mixture is pipetted on the surface of water, so that in the beginning a homogenous lipid monolayer is formed at the very air-water interface. This layer is first in zero surface pressure, describing "gas phase" lipid molecules dispersed randomly on the surface of the interface, diffusing fast on the surface. The formed monolayer is then compressed slowly by the trough, and after a short while a continuous lipid layer will form, after which possibly one or several lipid layer's phase transitions can be seen if there should be any concerted conformational changes in the organization or tail orientations of the lipids as the lipid layer adapts to the slowly compressing surface area. Finally the layer will turn to a solid phase, and right after that break, as the lateral pressure becomes too high for the lipid layer to adapt.

During the whole process the surface pressure and the area of the lipid layer are measured, and the results are represented as an area/pressure curve, where the surface pressure of the system is represented as a function of the surface area available (on average) for each lipid of the system (area/lipid).

Here the layers were not compressed to very high surface pressures to avoid the layer collapse. The layers were compressed to 40 mN/m surface pressure, and right after that expanded to the original area of the layer (in the gas phase).

Additional details are given in refs. [30, 207].

The outer layer of human tear film – the tear film lipid layer – covers the surface of the eye, in the very interface between the tear film and the air surrounding the eye. Abnormal composition of the tear film lipid layer may have quite severe consequences for health in terms of the so-called "dry eyes syndrome".
In this thesis, the tear film lipid layer was investigated by the means of molecular dynamics simulations. It was found that the lipids form a layer to the very interface of air and water. In the normal tear film composition, phospholipids formed the main body of the interfacial layer, while cholesteryl esters were observed to penetrate into it, promoting tighter packing of the interfacial layer. When the system was exposed to decreasing interfacial area to investigate what happens when eyes are being blinked, triglycerides helped the layer to stay intact even at very small interfacial areas. Meanwhile, with lipid layers characteristic to blepharitis patients, the ability to form a continuous lipid layer to the surface was impaired.

ISBN 978-952-60-5489-6
ISBN 978-952-60-5490-2 (pdf)
ISSN-L 1799-4934
ISSN 1799-4934
ISSN 1799-4942 (pdf)

Aalto University
Aalto University School of Science
Department of Applied Physics
www.aalto.fi

BUSINESS + ECONOMY

ART + DESIGN + ARCHITECTURE

SCIENCE + TECHNOLOGY

CROSSOVER

DOCTORAL DISSERTATIONS

Aalto-DD 210/2013